University of California
Santa Barbara

# Gold Nanoparticle Characterization: Improved Methods for Measuring Nanoparticle Surface Properties and Colloidal Stability

A dissertation submitted in partial satisfaction
of the requirements for the degree

Doctor of Philosophy
in
Mechanical Engineering

by

Tyler R. Ray

Committee in charge:

Professor Sumita Pennathur, Chair
Professor Matthew Begley
Professor Andrew Cleland
Professor Carl Meinhart

December 2015

The Dissertation of Tyler R. Ray is approved.

---

Professor Matthew Begley

---

Professor Andrew Cleland

---

Professor Carl Meinhart

---

Professor Sumita Pennathur, Committee Chair

October 2015

Gold Nanoparticle Characterization: Improved Methods for Measuring Nanoparticle Surface Properties and Colloidal Stability



by

Tyler R. Ray

To Sumita

# Acknowledgements

I first and foremost thank my PhD Advisor Sumita Pennathur. Over the course of my PhD, you provided the resources, expertise, and mentorship that enabled my growth as a researcher and experimentalist. Your passion for research combined with your collaborative approach to solving transformative, interdisciplinary problems provided a wonderful model for pursuing research at the interface of scientific disciplines. I offer my sincerest thanks for the countless opportunities you provided to explore challenging scientific questions while refining my research interests. Your dedication to both research and teaching serves as an inspiring model for my future academic pursuits.

I also thank the members of my PhD Committee Matt Begley, Andrew Cleland, and Carl Meinhart for all of their time, support, and direction throughout my PhD. In particular, I thank Matt for your mentorship and guidance. It was invaluable in both my engineering education and development as a researcher. The example you set through your approach to overcoming roadblocks in pursuit of scientific questions transformed the way I approach scientific discovery. Andrew, I thank you for your countless contributions to refining my experimental approaches, especially early on in my research. The opportunity to work with your group offered wonderful insight into research as an experimentalist. Carl, I thank you for the invaluable discussions on both COMSOL modeling and particle behavior in microfluidic systems. Your knowledge provided significant insight into the phenomena observed in my experimental work.

Throughout my PhD, I have had the distinct privilege to work with many wonderful people without whose contributions this work would not have been possible. I specifically thank my co-authors Bethany Lettiere, Joe De Rutte, and Dr. Kjeld Janssen. I also thank my fellow lab members Travis del Bonis O'Donnell and Tom Wynne for the countless discussions and experimental troubleshooting throughout our time together at UCSB.

Although not directly involved with my research, I thank fellow graduate students and post-doctoral scholars Dr. Scott Ferguson, Dr. Chris Bergner, Dr. Chrysafis Andreou, Dr. Rachel Collino, Dr. Demis John, and Dr. Pete Crisalli for all of the support provided throughout my PhD and whose interactions brought great fun to even the most tedious of experiments. I am also indebted to the members of the Pennathur Lab with whom I have worked, both past and present, for blazing the trail upon which this work is based: Sharice Handa, Jared Frey, Jess Sustarich, Alex Russell, Neeraja Venkateshwaran, Dr. Logan Garner, Alex Dixon, Ben Eovino, John Herr, Deep Shah, Andrew Crumrine, Chris McCallum, Mike Garcia, Josh Loessburg-Zahl, Sam Sherman, Marco Palombo, and Seth Boden.

I also thank my friends and my family for their encouragement over the course of my PhD for which I am most grateful. Finally, I extend a heartfelt thanks to Monica for her support throughout this process without which this work, truly, would not have been possible.

## Abstract

Gold Nanoparticle Characterization: Improved Methods for Measuring Nanoparticle Surface Properties and Colloidal Stability

by

Tyler R. Ray

Plasmonic nanoparticles are used in a wide variety of applications over a broad array of fields including medicine, energy, and environmental chemistry. The continued successful development of this class of materials requires the accurate characterization of nanoparticle stability for a variety of solution-based conditions. Although a wide array of methods exist, there is an absence of a unified, quantitative means for complete nanoparticle characterization. This work focuses on the challenges inherent with current methods through a comparative analysis of the current gold standard characterization methods. I propose using capillary electrophoresis and micro-capillary electrophoresis as powerful tools for better quantifying the inherent polydispersity and differences in surface functionalization within a nanoparticle sample. I present the Particle Instability Parameter (PIP) as a robust, quantitative, and generalizable characterization technique based upon UV-Vis absorbance spectroscopy to characterize colloidal instability. I validate PIP performance with both traditional and alternative characterization methods by measuring gold nanorod instability in response to different salt (NaCl) concentrations and as a function of solution pH, salt, and buffer type. I contextualize these methods within the literature on gold nanoparticle characterization to establish a standardized methodology for nanoparticle analysis. Finally, I present a concept for an integrated biodiagnostics platform using gold nanorods based upon an integrated microfluidic microspectrophotometry system for the detection of pathogens.

# Contents

# Chapter 1

# Preface

## 1.1 Motivation

When Gerd Binnig and Heinrich Rohrer invented the Scanning Tunneling Microscope in 1981, they opened the doors to the world of nanotechnology, a term coined by Norio Taniguchi almost a decade earlier in 1974. The seemingly limitless possibilities offered by nanotechnology to shape the natural world by precisely controlling the placement and structure of atoms, only further popularized by Erik Drexler in his seminal book "Engines of Creation," has inspired a whole generation of researchers [1]. There are an estimated number of over 150,000 researchers in the US, 400,000 worldwide working in the field as of 2010 [2].

Despite the great interest and focus of scientists along with trillions of dollars in research grants, the commercial "real world" impact has been limited with only 1300 nanotechnology-based products on the market as of 2012 [3], [4]. The limited realization of nanotechnology's promise lies in the significant challenges researchers face in harnessing and translating the novel and unique material properties of the nanoscale into macroscale applications [2]. While researchers have made great fundamental advances

in manipulating and controlling matter on the nanoscale, scaling up these techniques to industrial, mass-production applications has proven a substantial hurdle.

The material properties seen on the nanoscale are exclusively size dependent. The term nanoscale refers to a specific class of materials that has at least one characteristic dimension between 1-100 nm in length. While engineered nanoparticles are commonly associated with the nanoscale, micro and macroscale objects with one dimension in the nanoscale (*e.g.*, nanofluidic capillary electrophoresis chips) are also considered to be "nano." As objects scale up to the microscale, they lose their nanoscale properties and exhibit the properties found in the bulk material / device. Of particular interest to both this PhD and to the research community as a whole is harnessing the nanoscale properties of engineered nanoparticles for macroscale applications without the loss of these unique material properties.

Engineered nanoparticles refers broadly to a class of particles that are nanoscale in nature and exhibit tailored material properties [5]. Examples include quantum dots, polymer beads, inorganic nanoparticles of defined shapes (*e.g.*, rods, spheres, dogbones, dumbells, triangles, stars), organic particles such as functionalized DNA strands, and inorganic / organic hybrids including silver DNA clusters and DNA decorated gold nanospheres. These particles, engineered for specific material properties, can exhibit a range of radically different mechanical, optical, thermal, electrical, and catalytic properties compared to their bulk counterparts. Of particular interest are gold nanoparticles, specifically gold nanorods and nanospheres, for the localized surface plasmon resonance and elastic light scattering they exhibit when excited by light from the visible spectrum. These properties enable a variety of applications including their use as biosensors, imaging devices, and cancer therapies.

The central challenge to continued application development of both gold nanoparticles and engineered nanoparticles as a whole is the absence of facile methods of rapidly

characterizing nanoparticle morphology and functionalization. Although many methods exist, development of new characterization tools and standardization of characterization approaches is a crucial area of continued research [6].

## 1.2 Scientific Hypothesis

The challenge of accurately characterizing engineered nanoparticles forms the foundational core of this dissertation with a particular focus on gold nanoparticle characterization. Specifically, I ask the question: *what is the best way to characterize the morphology, surface properties, and environmental interactions of gold nanoparticles so as to engineer specific material properties and behavior suitable for biodiagnostic applications?*

In this dissertation I propose that microfluidics offers a compelling platform for nanoparticle characterization that when coupled with optical spectroscopy, enables the facile characterization of the size, polydispersity, surface charge, and colloidal stability of a nanoparticle population. To do this, I experimentally compare the measurement performance of standard nanoparticle characterization tools to that of capillary and micro-capillary electrophoresis for morphology and surface property analysis. I investigate the use of UV-Vis spectroscopy as a method to characterize colloidal stability for nanoparticle populations in comparison with Dynamic Light Scattering measurements. Finally, I explore the combination of optical absorption spectroscopy with micro-capillary electrophoresis as a characterization and biosensing platform for gold nanoparticles.

## 1.3 Chapter Synopses

This dissertation is built upon the three core areas described above. Chapter 2 provides a broad overview of nanoparticle characterization methodology with specific details

regarding gold nanoparticles. Chapter 3 studies the efficacy of different methods for characterizing commercially synthesized, fluorescently functionalized gold nanoparticles and investigates for the first time the characterization of gold nanorods via micro-capillary electrophoresis. Chapter 4 presents a new method for characterizing the colloidal stability of a gold nanoparticle suspension using UV-Vis spectroscopy. Chapter 5 details the work focused on integrating optical microspectrophotometry and micro-capillary electrophoresis for gold nanoparticle characterization. Chapter 6 provides a summary of this work and an outlook on future directions.

## 1.4 Permissions and Attributions

The content of Chapter 4 and Appendix A is the result of a collaboration with Bethany Lettiere, Joseph de Rutte, and Sumita Pennathur and has previously appeared in Langmuir[7]. It is reproduced here with the permission of American Chemical Society: `http://pubs.acs.org/`.

# Chapter 2

# Theory and Background

## 2.1 Gold Nanoparticles

Metallic nanoparticles have captivated the imaginations of glassworkers, alchemists, scientists, and researchers since the early Middle Ages. Medieval artisans blended tissue-paper thin gold sheets into molten glass to create stained glass panels with vivid, rich ruby red hues to grace the windows of the gothic European cathedrals. These artisans unknowingly created a composite of colloidal gold nanospheres suspended in a glass matrix.

While history speaks of the ancient recipes alchemists and artisans used to create colloidal gold solutions of different colors, a systematic study of gold colloid optical properties wasn't conducted until Faraday's work in 1857. Faraday's interest in gold colloids, much like that of today's researchers, stemmed from the unique optical properties metallic nanoparticles possess on the nanoscale as compared to their macroscale or "bulk" material counterparts. In a paper to the Royal Academy of Science, Faraday detailed his work with "finely-divided gold," where he studied the vivid colors produced by solutions of suspended gold colloids [8]. His work was the vanguard for the modern field of colloid

chemistry and heralded the start of intense interest in colloid suspensions [9].

Faraday's work with gold colloid suspensions also marked the beginning of researchers' intense exploration of a very specific subset of metallic colloids – noble metal nanoparticles. Noble metal nanoparticles, specifically gold nanoparticles, exhibit a variety of unique material properties beyond their optical properties including photothermal, catalytic, and electrical properties along with bio-inert surfaces that can be easily functionalized [10]. Additionally, gold nanoparticles exhibit material properties fundamentally different from other nanoparticles with examples including their preferential accumulation in tumor cells and their ability to enter biological cells much faster than small molecules [11]. These material properties, along with easier synthesis methods, has continued to drive research interest promoting the development of compelling nanoparticle applications such as their use as biosensors, cancer therapies, composite material components, and drug-delivery mechanisms. This is further evidenced by the fact that since 1990 the number of papers published on gold nanoparticles each year has grown exponentially[12].

Although the field is vast, especially considering the wide array of synthesized shapes and sizes of gold nanoparticles, this PhD is focused on a very specific subset of nanoparticles: the study of metallic gold nanorods and, to a lesser degree, gold nanospheres. Gold nanorods, as with other metallic nanoparticles, possess novel and captivating optical properties as a result of their nanoscale size and shape. This is a result of two phenomena known as localized surface plasmon resonance and resonant (Rayleigh) elastic light scattering they exhibit when excited by light from the visible spectrum. The specific interest in gold nanorods stems from the fact that these two phenomena are shape dependent with gold nanorods exhibiting remarkably different behavior compared to nanospheres of the same diameter.

**Localized Surface Plasmon Resonance** When gold nanorods are excited by light of the appropriate resonant frequency, they exhibit a behavior known as localized surface plasmon resonance. At these frequencies, the nanorods intensely absorb the light and because the diameter of the nanoparticles is smaller than the penetration depth of the evanescent wave generated by the exciting light, the wave penetrates the particle. The absorbed energy from the photons of light couples to the conduction band electrons in the gold nanoparticles and create a negative charge on one side of the particles. As a result, a "restoring" force arises to neutralize the attractive force between the two oppositely polarized sides causing the electrons to collectively oscillate [13, 14]. These oscillations are referred to as plasma oscillations, plasmons, surface plasmons, particle plasmons, or surface plasmon polaritrons [15, 16]. The frequencies for the plasmon resonance are known as plasmon bands or plasmon absorption bands. Most metallic nanoparticles exhibit surface plasmon resonance, but the particular frequencies can vary widely across the electromagnetic spectrum. For gold nanoparticles, the resonant frequencies are primarily in the visible or near-infrared ranges with the plasmon resonance wavelength for nanospheres centered around 520 nm [17].

As the aspect ratio of the nanoparticles increase from spheres to rodlike shapes, the gold nanorods exhibit not only the plasmon band associated with gold nanospheres at 520 nm, but also a second plasmon band either in the red or near-infrared range of the spectrum. The absorbance spectrum of the second plasmon band shifts further into the near-infrared with increasing nanorod length as the absorbance of the red wavelength of light increases [18]. These two plasmon bands correspond to the two axes of the nanorod: the short or transverse axis and the long or longitudinal axis [19]. *It is important to note that since the second plasmon band is length dependent, one can tune the plasmon absorption of the nanorods simply by controlling the nanoparticle length. The tunable nature of the absorption peak has enabled the possibility of a wide range of gold nanorod–*

*based sensors.*

**Rayleigh Light Scattering** Light is not only absorbed by the plasmons but is also elastically scattered, a behavior known as Rayleigh light scattering. As the nanoparticle increases in size, the amount of light elastically scattered increases compared to the light absorbed [20]. The plasmons absorb and scatter light at the same wavelength [13]. As a result of the gold nanorods resonant frequencies being predominantly in the visible region of the spectrum, this scattering can be used to visualize the gold nanorods and track their spacial position. When gold nanoparticles are viewed under an optical microscope at 100x magnification, as a result of the scattering of visible light, individual colored spots 250-500 nm in diameter appear and directly correspond to either individual nanoparticles or small clusters of nanoparticles in close proximity [19]. Aggregation of nanoparticles can cause a color shift as the plasmon resonance of one rod can couple to another rod if they are separated by <100 nm.

**Orientation Effects** Beyond the tunability of the plasmon resonant frequency in gold nanorods that results from changing the aspect ratio of the nanorods, the light scattered by the nanorods is highly dependent on orientation as a result of this anisotropy. Alivisatos and others, when imaged using darkfield microscopy under polarized light conditions, observed that the light scattered by the nanorods is strongly polarized in the direction of the long-axis of the nanorods [21]. Tracking the color shift associated with the nanorod excitation can be used to detect nanorod orientation in either solution [21] or locked in a transparent polymer [22]. While the surrounding media can shift the resonant frequency of the nanorods, in both instances the nanorods could be accurately characterized. This characterization is applicable for rods of varying aspect ratios with plasmon bands in both the visible and near-infrared ranges of the spectrum.

### 2.1.1 Applications

Gold nanorods, as a result of their light scattering and aspect–ratio dependent properties, are found primarily in applications serving as sensors or markers, especially in cell biology [20]. Specifically, gold nanorod applications can be categorized into drug delivery mechanisms, biological sensors, environmental sensors, cancer therapies, and other applications such as composite material filters or image markers.

There have been many reviews on the applications of gold nanorods and gold nanoparticles in general. [12] provides one of the earlier reviews on the broad field with an excellent introduction to the field of noble metal nanoparticles and their current applications. The specific focus of this review is the origin of the surface plasmon resonance properties of gold nanoparticles, their synthesis procedures, and potential applications. [23] follows up this review with another exploring the specific optical and photothermal properties gold nanoparticles possess and the applications in imaging and sensing these properties open up. [24] provides another excellent topical overview on the uses of gold nanoparticles with a look to future applications. More recently, gold nanorods have been introduced into a variety of biological applications with very specific developments in surface functionalizations (review by [25]), medical treatments (review by [26]), energy applications (review by [27]), and general biomedicine (review by [11]).

Specifically, there has been much work by researchers exploring the use of gold nanorods as biosensors. [28] studied the use of gold nanoparticles as bioconjugates for aiding the study of Gelatin and Human IgG adsorption through the use of light scattering spectra and dynamic light scattering. [29] published an excellent paper exploring the use of gold and silver nanoparticles as sensors and the influence on the sensitivity of plasmon response to size, shape, and metal composition. More recently, [30] developed an ultrasensitive method for the detection of gene fragments using gold nanoparticles

and dynamic light scattering. [31] used color changes and dynamic light scattering to detect DNA sequences using gold nanospheres and gold nanorods. Several researchers, [32], [33], and [34] use gold nanoparticles to detect viruses through different nanoparticle surface coatings.

Gold nanoparticles also lend themselves to being used as environmental sensors, specifically the detection of Mercury in the environment. [35], [36], [37], [38] have each demonstrated the ability to sense Mercury in various forms and environments with extremely high sensitivity using gold nanoparticles. Gold nanoparticles have also been used to detect arsenic in groundwater by [39].

Some of the most novel work with gold nanorods involves their use as a cancer therapy. As a result of the gold nanorods exhibiting surface plasmon resonance, they generate a great deal of heat when excited at the surface plasmon resonance peak. If the nanoparticles are functionalized such that they preferentially bind to tumor cells, this property can be used to selectively ablate tumor cells. [40] and [41] provide excellent overviews to this process and the work that has been done in developing this new type of therapy.

These are not the only uses of gold nanoparticles and specifically gold nanorods. Mechanical engineers and physicists are also highly interested in the unique material properties these materials possess and have extended their use into traditional engineering disciplines. Examples include [42] using gold nanorods as an optical pattern for digital image correlation to track the local deformation in collagen between cells in real time and the development of optical metamaterials with a negative index of refraction [43].

### 2.1.2 Gold Nanorod Synthesis

The gold nanorods used in this work were created using the well-established seed-mediated growth approach developed in the Murphy Lab at the University of South

Carolina [44, 45]. This process can produce a relatively monodisperse solution containing 90% gold nanorods of uniform length. Both "long" and "short" nanorods can be produced through this process.

**Seed Solution Preparation:**

Combine 9.75mL of 0.1M CTAB with 0.25mL of 0.01M $HAuCl_4$ (gold salt) in a sterile conical flask. Rapidly add 0.6mL of ice cold 0.1$NaBH_4$ (sodium borohydride) to the solution while stirring. Stir solution at a medium speed for 2 minutes. With the addition of the $NaBH_4$, the solution will turn from gold to dark brown, indicating the formation of spherical nanoparticles. This solution should be used within 2 to 5 hours from preparation.

**Short Nanorod Preparation:**

The following detailed process yields nanorods of aspect ratio up to 6. Figure 2.1 provides a graphical overview of this process. Specifically, the process consists of adding 9.5mL of 0.1M CTAB into a clean test tube, followed by the addition of the desired quantity of $AgNO_3$ (silver nitrate). After mixing these two quantities together, 0.5mL of $HAuCl_4$ is added to the test tube, which is then inverted. The addition of the gold salt turns the clear solution into a solution with a rich, dark gold color. It is important to note that if multiple batches of rods are produced, each test tube must be treated separately from this point onwards. Next, add 0.055mL of freshly prepared 0.1M ascorbic acid to the solution and invert the test tube. The solution should immediately turn from a dark gold color to clear. If any color remains, rods will not form. 0.012mL of the gold seed solution is then added to the solution and the test tube is very slowly tipped to one side in a one-half inversion. The solution is then left overnight and will slowly change from clear to a colored solution whose specific color depends upon the aspect ratio of the gold

nanorods. This preparation will produce rods as small as 10nm and as large as 120nm. The precise aspect ratio of the gold nanorods depends upon the amount of silver nitrate added to the solution. For rods 10 nm in length, 0.01mL of 0.01 M $AgNO_3$ should be used. A 0.01mL increase in amount added corresponds to a 10 nm increase in rod length until the maximum length of 120 nm is reached.

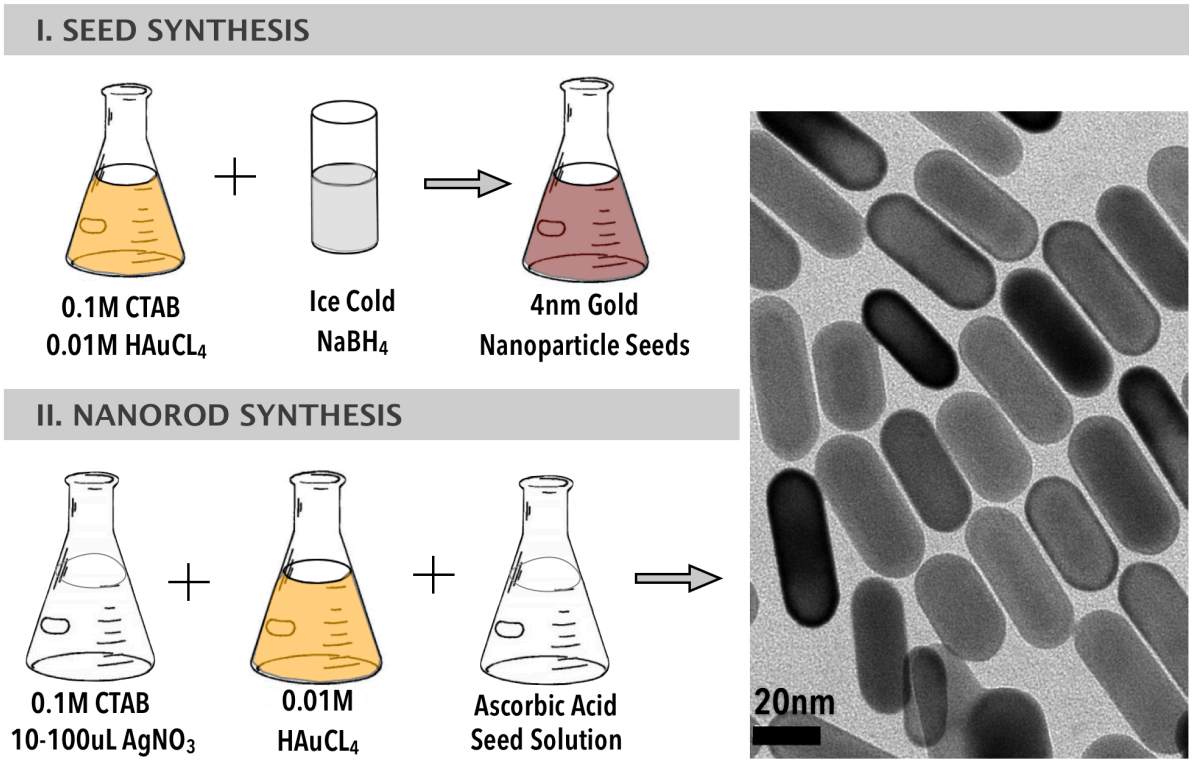


Figure 2.1: The process for synthesizing short gold nanorods (aspect ratio less than 6) is presented graphically. Briefly, a seed solution is created consisting of 3nm gold spheres by reducing chloroauric acid with a strong reducing agent in the presence of surfactant. A solution of surfactant, silver nitrate, and chloroauric acid is then mixed with a weak reducing agent (ascorbic acid) to create a growth solution, which upon the addition of a small amount of the seed solution, will yield gold nanorods if left undisturbed overnight. The length (aspect ratio) of the synthesized nanorods depends upon the amount of silver nitrate added to the growth solution before the addition of the ascorbic acid.

A photograph of nanorods synthesized by this method are shown in Figure 2.2 as synthesized by me in our lab.

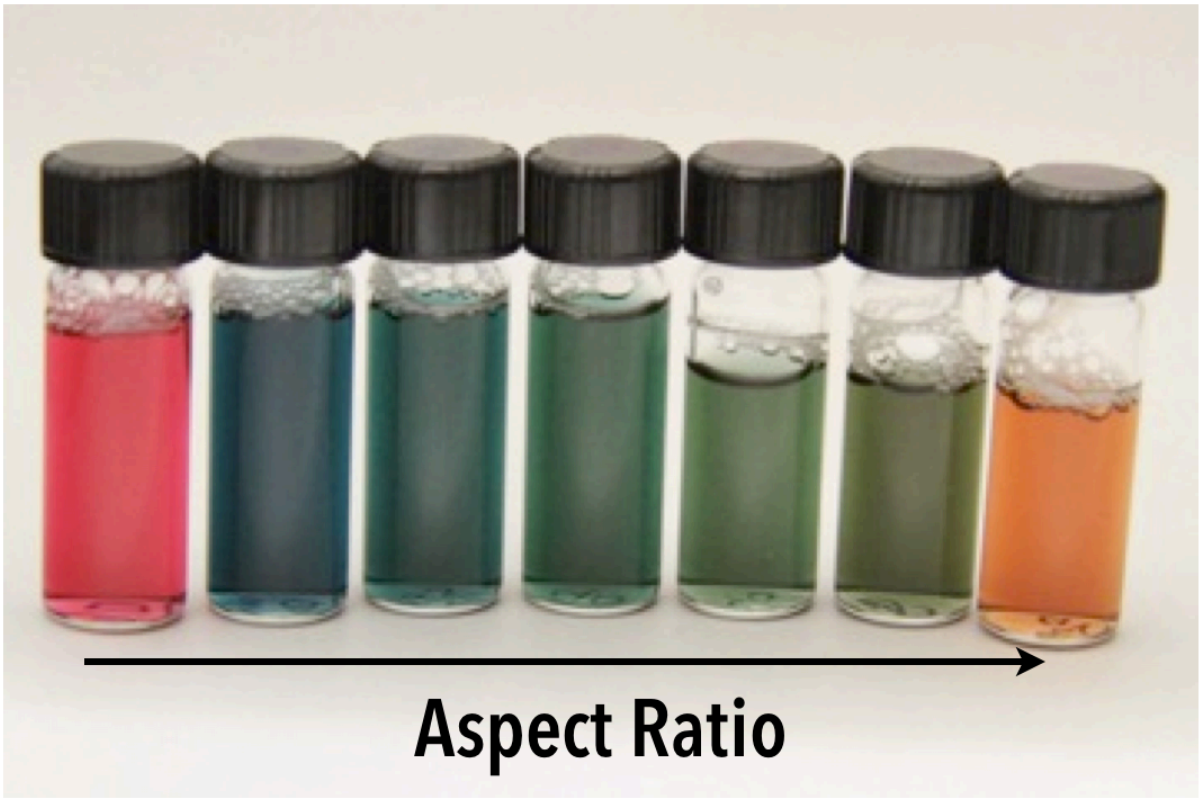


Figure 2.2: Color image of synthesized nanospheres and nanorods. The left–most vial contains synthesized nanospheres (25nm in diameter) for comparison to the nanorod samples. The color shifts from blue to green to tan to brown as the nanorods increase in aspect ratio. As this synthesis method maintains the same diameter of the nanorods, a change in aspect ratio is directly related to a change in nanorod length.

**Long Nanorod Preparation:**

Long nanorods are prepared through a three-step process, which produces nanorods with an aspect ratio of 13 +/- 2. 9mL of 0.1 M CTAB is added to each of three test-tubes labeled A, B, and C. 0.25mL of 0.01M HAuCl4 is added to each test tube followed by 0.05mL of freshly prepared 0.01 M ascorbic acid. 1mL of the 4nm gold seed solution is then added to test-tube A and stirred vigorously for 30s. The color of test-tube A turned red within 2-3 min. of the addition of the seed. After 4-5h, 1mL of the solution was pipetted into test-tube B and stirred vigorously. The color of test-tube B turned red within 4-5 min. of the addition of the solution from A. After 4-5h, 1mL of the solution is

pipetted into test-tube C followed by vigorous stirring. The color of test-tube C turned red with within 10 minutes of the addition of the solution from B. This solution was left overnight. Excess CTAB was removed from the solution in test-tube C by centrifuging test- tube C at 2000rpm for 30 minutes at room temperature. The supernate, which contains the excess CTAB and non-nanorod nanoparticles, is then removed and the remaining pellet is re-dispersed in 1mL of water and sonicated. The solution contains gold nanorods with an aspect ratio of 13.

### Material Considerations

The chemistry involved in synthesizing gold nanorods is quite complex and requires materials to be of a certain quality. The Deionized water (DI) used for this synthesis was 18.1 MΩ from a Millipore system. All chemicals were ordered from Sigma-Aldrich and were used as received. It should be noted that this process is very sensitive to the purity of the CTAB and for this synthesis the ultra-pure CTAB, H9151, was used. Temperature is also a factor in synthesis and as such the CTAB, seed, and growth solutions were kept at a constant 26 °C during the growth process in a home–built incubator.

## 2.2 Nanoparticle Characterization Methods

Accurate methods of nanoparticle characterization are vitally important for further breakthroughs in the field as well as the industrial development of nanoparticle applications. Current methods are limited by a variety of factors with no one technique offering the necessary sensitivity, accuracy, affordability, or speed to fully characterize nanoparticle samples. The ability to perform in-situ rapid characterization of the size, shape, surface charge, and nanoparticle stability in a variety of environments would be beneficial in further extending nanoparticle development and application.

## 2.3 State of Characterization

Nanoparticles are characterized using a variety of techniques ranging from individual nanoparticle measurements to bulk, ensemble studies of colloidal solutions. These techniques can be generally classified based on the analytical method and are broadly listed in Table 2.1. While not an exhaustive list, the breadth demonstrates the large number of techniques developed for nanoparticle characterization.

Although there exists a wide range of techniques available as seen in Table 2.1, *literature reflects three common techniques used across all disciplines that form the workhorse characterization methodology for gold nanorod analysis.*

- `TEM` to image the physical structure of the nanoparticles
- `DLS` to characterize ensemble colloidal properties and determine nanoparticle zeta potential or "surface charge"
- `UV-Vis` to characterize the light response and concentration of nanoparticles

Similar to other nanoparticles, gold nanorods are characterized primarily using the three techniques listed above. Specifically, gold nanorods are commonly characterized by their size using TEM [59, 60, 10, 61], their zeta potential using DLS [57, 62, 63, 64, 65, 66, 67, 68, 69, 70], and their absorbance spectra using the UV-Vis [57, 36, 71, 72].

By using these three techniques, researchers try to overcome the limitations inherent in each technique to better understanding the precise nature of the nanoparticle being characterized.

Specific limitations with TEM analysis include not only the high-cost of ownership, operation, and maintenance (+$250K), but also the substantial operational and analytical time and skill required to characterize nanoparticle samples. As this is a single particle measurement, great care must be taken to analyze a statistically significant number of

| Classification | Technique | Type |
|---|---|---|
| Chromatography | Size Exclusion (SEC)[46], Capillary Electrochromatography[46], Gas (GC)[46], Liquid (LC)[46], High-Performance Liquid (HPLC)[46], Micellar Electrokinetic Chromatography[46] | Ensemble |
| Microscopy, *Optical* | Brightfield, Darkfield[47], Confocal, Total Internal Reflection | Ensemble |
| Microscopy, *Electron* | Transmission Electron (TEM), Scanning Tunneling, Scanning Electron | Single |
| Microscopy, *Other* | Atomic Force (AFM), Kelvin Probe | Single |
| Scattering | Dynamic Light (DLS)[48], Interferometry[49], Nanoparticle Tracking Analysis (NTA)[50], Rayleigh (Resonant) Light (RLS)[41] | Ensemble |
| Separations, *Electrophoresis* | Gel[51], Capillary[52], Microfluidic Capillary[53], Nanofluidic Capillary[54], Polyacrylamide Gel (PAGE)[55] | Ensemble |
| Spectroscopy, *Physical* | Mass (MS)[56], Matrix–Assisted Laser Desorption Ionization (MALDI)[56] | Ensemble |
| Spectroscopy, *Light* | UV-Visible Absorbance (UV–Vis)[57], Raman[10], Surface Enhanced Raman (SERS)[10], Circular Dichroism[58], Fluorescence[54] | Ensemble |
| Other | Field Flow Fractionation (FFF)[46], Centrifugation, Ultracentrifugation | Ensemble |

particles in order to draw accurate conclusions about the sample. Due to the TEM measurement using an electron beam to "image" a nanoparticle, samples that are organic, non-solid, or deformable do not image either clearly or at all. For gold nanorod analysis, this limits the ability to detect coatings, such as the CTAB bilayer coating the outer surface of the gold nanorod core.

DLS equipment, while moderately expensive ($30-$50K), offers a simple turnkey solution to ensemble particle measurements. The ease of use offered by DLS has prompted its rapid adoption in many research laboratories, but at the expense of utilizing the technique to characterize particles without assessing its suitability to the sample. Some of the DLS limitations include inability to accurately characterize polydisperse samples, non-spherical particles, nanoparticles smaller than 100 nm in diameter, and non-optically clear (turbid) samples[69, 73, 46]. Although some of these limitations can be addressed by appropriate sample preparation, the DLS technique is often limited to qualitative rather than quantitative measurements when analyzing nanometer sized particles [74]. Specific to gold nanorods, their highly charged surface (surface coatings typically >25mV [59]) causes significant issues with the accurate reporting of the nanorod zeta potential [46]. Furthermore, the anisotropy of the nanorod shape prohibits accurate size measurements, instead yielding an average size from the diameter and nanorod length.

The UV-Vis instrument is a relatively inexpensive measurement technique ($10–$60K), but limited to measuring the absorptivity and concentration of a colloidal solution of nanoparticles. This technique is readily suited to nanoparticles that strongly absorb or scatter light, such as metallic nanoparticles. While also a turnkey solution, less knowledge is required to measure accurate spectral data of a nanoparticle sample. The technique's limitations stem from the fact that it is difficult to resolve accurate spectral information from polydisperse samples, highly concentrated samples, and samples that have weak signal response compared with the background solvent. As this is an

ensemble measurement, specifics about individual nanoparticles or smaller population subsets of a sample are lost in the aggregated measurement. This is especially true for gold nanorod absorbance spectra measurements. The gold nanorod absorbance spectra is broadened as a result of the inherent polydispersity present in synthesized nanorod solutions [11, 75, 76, 25, 41, 77] , along with trace elements of non-nanorod shaped gold nanoparticles (e.g. spheres, triangles, etc.) [72] as compared to the theoretical absorbance spectra calculated by Mie Scattering Theory[78].

Nanoparticle characterization and analysis is a challenging and complex topic. Current state one that has been covered in great detail in several excellent treatments by [79, 56, 61, 80]. As seen from these reviews and from experimental literature, better characterization methods are required for the advancement of nanoparticle–based applications [81]. Specifically, new methods to perform the in-situ rapid characterization of the size, shape, surface charge, and nanoparticle stability in a variety of environments are critical to the progress of several different applications.

Specific examples include:

- `Biosensors`: The development of nanoparticle based biosensor applications utilizing the Localized Surface Plasmon Resonance of gold nanorods. LSPR biosensors require monodisperse populations for the greatest sensitivity [82] as even small differences in length can cause significant signal shifts [10].

- `Composite Materials`: Using gold nanorods in composite materials or as self-assembly building blocks also requires precise size control over the nanorod population [83]. The inability to accurately and rapidly characterize nanoparticle size will hamper further development of nanoparticle–based applications such as these.

- `Molecular Identification`: SERS detection of molecular targets of interest strongly depends on the shape and size of the gold nanorod [29]. Without careful control

over both properties, SERS "hotspots" will be limited weakening the maximize Raman signal strength.

- `Nanomedicine`: In nanoparticle cancer therapy treatments the shape of a nanoparticle governs the effectiveness of the nanoparticle at converting light to heat for tumor irradiation [84, 85, 34]. The charge of gold nanorods can also influence the ability of the nanorods to infiltrate tumor cells and collect at the appropriate cellular targets [86] necessitating careful control over surface charge to optimize treatment effectiveness.

## 2.4 Summary

Gold nanoparticles hold great promise for novel applications as a result of their unique optical and photothermal properties, availability of synthetic protocols that can tune the size and shape of the particles, ability to modify the surface and conjugate drugs/molecules to the nanorods, and relative biocompatibility. However, standard methods for determining raw nanoparticle synthesis quality, such as DLS and UV-Vis spectroscopy, have detection limits restricting measurements to bulk solution averages, which in turn prevent the characterization of nanoparticle polydispersity necessary for increasing their effectiveness in therapeutic applications. Furthermore, conformation microscopy techniques such as TEM analysis, although able to accurately determine the size and shape of particles also are not ideal as they do not allow for in-situ analysis. Therefore, further breakthroughs and industrial development of metallic nanoparticles require the in-situ rapid characterization of the size, shape, surface charge, and nanoparticle stability in a variety of environments. The forthcoming chapter investigates the potential of capillary electrophoresis and micro-capillary electrophoresis as an improved analytical approach to nanoparticle characterization in comparison with the aforementioned

standard characterization methods.

# Chapter 3

# Comparative Analysis of Nanoparticle Measurement Methods

## 3.1 Motivation

Engineered nanoparticles are broadly used in an array of applications as a result of their unique material properties. Of particular interest are gold nanoparticles due to their unique light scattering, electrical, and chemical properties enabling their use in applications such as biosensing[87], diagnosis[88], therapeutics[89, 90], photovoltaics[91], energy storage[92], reusable catalysts[93], chemical analysis[94], and water purification[95]. Successful application development requires the ability to carefully manipulate and control nanoparticle material properties. It is therefore critically important to be able to accurately, precisely, and completely characterize the nanoparticles during and after synthesis. Factors such as shape. size, and surface chemistry can heavily influence the final material properties, especially when the nanoparticles are non-spherical [84]. Characterization tools are also important outside of the laboratory as understanding how nanoparticles interact with the environment is vital for developing new nanoparticle applications and

therefore robust characterization tools are required that can distinguish the nanoparticle behavior apart from the myriad of external environmental factors and contaminants[96].

Similar to other nanoparticles, gold nanoparticles are characterized primarily using Transmission Electron Microscopy (TEM), Dynamic Light Scattering (DLS), and UV-Vis Spectroscopy. Specifically, gold nanorods are commonly characterized by their size using TEM [59, 60, 10, 61], their zeta potential using DLS [57, 62, 63, 64, 65, 66, 67, 68, 69, 70], and absorbance spectra using UV-Vis [57, 36, 71, 72]. Although widely adopted, these characterization methods are insufficient to fully characterize nanoparticle properties[6] as detailed in several excellent treatments by [79, 56, 61, 80]. As elucidated both in these reviews and from experimental literature, better characterization methods are required for the advancement of nanoparticle–based applications [81]. Specifically, new methods to perform the in-situ rapid characterization of the size, shape, surface charge, and nanoparticle stability in a variety of environments are critical to the progress of several different applications.

Researchers have been working to fill this analytical need by extending standard nanoparticle characterization techniques [65] or applying bioanalytical characterization techniques such as gel electrophoresis [51] and CE [97, 98, 99, 100, 101]; however, neither path has developed a technique that can fully describe both the size and shape distribution of synthesized gold nanorods.

Khlebtsov in 2004 worked on extending DLS and UV-Vis to better size gold nanoparticles by comparing peak absorption position from the UV-Vis to particle size from DLS with moderate success [102]. Perez-Juste and Luis M. Liz-Marzan continued to develop DLS for relatively short length ($< 100$nm) nanorods by incorporating translation and rotational diffusion calculations in the DLS measurement[66]. Khlebtsov continued his work with DLS nanoparticle sizing to better understand and resolve the false peak information generated by the rotating diffusion of nanorods [68]. They found that the DLS

peak width did not correspond to TEM measurements and concluded that the DLS was best suited for slow aggregation bio-conjugation studies of gold nanorods. Based upon this work, Compagnini [57] and Muschol [67] used depolarized DLS to try to improve DLS nanoparticle size measurements. While they found some improvements, the influence of gold nanorod diffusion (both translational and rotational) introduced a 10%–20% discrepancy as compared to TEM measurements[67].

Much of the work in adapting techniques from the bioanalytical field to nanoparticle analysis has centered on utilizing electrophoresis in either a gel or capillary to separate out populations of nanoparticles based upon size and shape [97]. While established as a workhorse technique for separating nanostructures such as DNA, gel electrophoresis has only been used in a few instances to characterize gold nanoparticles [103]. Both [104] and [51] published papers on using gel electrophoresis to separate gold nanorods and nanospheres, but with limited separation resolution. However, little work has been done since these two papers.

Overwhelmingly, researchers have focused on adapting CE to nanoparticle characterization. Capillary electrophoresis (CE) is a powerful and well-established technique for separating and analyzing charged species of interest[105]. Although traditionally used for the characterization of ionic and molecular analytes, researchers have demonstrated the efficacy of CE in characterizing both the size and surface charge of an array of nanoparticles[106] including AuNS[107] and quantum dots[108].

The use of CE in AuNP characterization is quite recent with [98] publishing some of the earliest work using CE to characterize the size distribution of synthesized gold nanospheres. They found moderate success in separating nanoparticles of different diameters. [109] published an early review on the use of CE of colloidal nanoparticles, a technique found to be successful in characterizing a variety of different nanoparticle size distributions. [52] used CE to separate gold nanospheres. They found that the surfactant

SDS was required to adequately separate the nanospheres in their buffer solution. They followed this work with another paper [110] where they examined the feasibility of employing CE to separate silver nanoparticles. They determined that without the addition of SDS to the running electrolyte, nanoparticle separations did not occur.

Improvements to separation resolution drove the work of [111] and [112] who both published on the use of reversed electrode polarity stacking mode (REPSM) in CE to enhance the detection and separation of mixtures of gold and silver nanospheres. [112] found that REPSM offered significant enhancement of nanoparticle separations compared to standard CE. An important point from this work is that they found a linear relationship between the electrophoretic mobilities and the sizes of the gold nanospheres with diameters from 5.3 to 59.9 nm where the relative standard deviations of the electrophoretic mobilities were below 0.6%. [106] published an excellent review of capillary electrophoretic characterization work to date and concludes that this nascent nanoparticle characterization technique holds much promise for developing a low-cost means of characterizing nanoparticles with great specificity and accuracy. We note that the primary focus of most of these studies have been on gold nanospheres and few studies exist characterizing anisotropic gold nanoparticles using CE.

Microchip CE ($\mu$CE), a recent subset of CE, has been extensively utilized with other forms of nanoparticles (e.g. DNA), but has not been explored in great detail for the study gold nanoparticles or gold nanorods [113], [106], [97]. Work by the Santiago [114] and Pennathur [53] groups have shown improved characterization methods using $\mu$CE for characterizing polystyrene nanoparticles. Although there is significant interest in integrating gold nanoparticles into microfluidic chips to improve $\mu$CE performance[115], to our knowledge, no $\mu$CE studies have been performed to characterize gold nanorods.

In this work, we characterize eight distinct populations of AuNPs, four AuNS and four AuNR, using TEM, DLS, and UV-Vis spectroscopy. We compare the performance

| Product Number | Type | SPR Peak (nm) | Diameter (nm) | Length (nm) | Concentration (nps/mL) |
|---|---|---|---|---|---|
| C16A1-10-CY488-TC-50 | Sphere | 529 | 10 | - | 4.60E+14 |
| C16A1-25-CY488-TC-50 | Sphere | 521 | 25 | - | 3.76E+13 |
| C16A1-100-CY488-TC-50 | Sphere | 583 | 100 | - | 3.77E+11 |
| C16A1-60-CY488-TC-50 | Sphere | 543 | 60 | - | 1.62E+11 |
| C16A2-25-700-CY488-TC-50 | Rod | 740 | 25 | 84 | 4.8E+12 |
| C16A2-25-980-CY488-TC-50 | Rod | 980 | 25 | 146 | 1.1E+12 |
| C16A2-40-700-CY488-TC-50 | Rod | 699 | 40 | 117 | 1.5E+12 |
| C16A2-50-700-CY488-TC-50 | Rod | 687 | 50 | 140 | 1.1E+12 |

Table 3.1: Commercial nanoparticles from Nanopartz with reported material values.

of these methods with both CE and $\mu$CE to evaluate the efficacy of CE and $\mu$CE as improved methods for analyzing AuNPs.

## 3.2 Materials and Methods

### 3.2.1 Chemicals

Sodium tetraborate decahydrate ($B_4Na_2O_7 \cdot 10H_2O$, S249, Fisher), Acetone (A18P-4, Fisher), sodium hydroxide (NaOH, S318, Fisher), Fluorescein sodium salt (F6377, Sigma-Aldrich), 6-Carboxyfluorescein (C0662, Sigma-Aldrich) were used as received. All suspensions were prepared using Millipore 18.2 M$\Omega$·cm DI water. AuNS and AuNR were ordered from Nanopartz (Loveland, Co.) with Alexafluor 488 fluorescent labels and carboxyl conjugation. Nanoparticle stock solutions were received highly concentrated (Optical Density: 50-60) in DI water and were diluted before use. Specific nanoparticle parameters are detailed in Table 3.1.

### 3.2.2 Methods and Instrumentation

#### Solution Preparation

*Buffer Preparation:* A stock solution of 150 mM borate buffer was prepared from sodium tetraborate in DI water. The final pH value was measured to be 9.2 at 22.1 C.

*Mobility Markers:* Stock solutions of 1 mM fluorescein (FL) and 6-carboxyfluorescein (6-FAM) were prepared from dry salts in DI water. A weak stock solution the combined dyes was used for µCE measurement such that the dye concentration in the final solution was 1 µM for both dyes FL and 6-FAM suspended in 10 mM borate buffer.

*Nanoparticle Suspensions (DLS, TEM, UV-Vis, CE)*: For each analysis solution, a 50 uL volume of concentrated nanoparticle sample was diluted to a final volume of 1 mL. The final solution had a background electrolyte concentration of 10 mM borate buffer and fluorescent mobility markers (50 µM [FL] and [6-FAM]).

*Nanoparticle Suspensions (µCE):* Prepared in the same was as previously described, µCE analytical solutions have a reduced mobility marker concentration to prevent camera signal saturation. Final concentrations are 0.5 µM for each dye.

We note that the concentration of the stock nanoparticle solutions is unknown due to the proprietary nature of Nanopartz's synthesis method. Per Nanopartz advertising, the nanoparticle solutions are synthesized using a non-citrate based gold nanosphere synthesis method. As an analogue, we hold the optical density constant among the nanoparticle samples.

#### Transmission Electron Microscopy

Transmission electron microscope (TEM) micrographs were taken using a FEI Tecnai G2 Sphera Microscope. TEM grids were prepared by drop-casting 10 µL of AuNPs onto a TEM copper grid (400 mesh, 01822, Ted Pella). AuNP dimensions were calculated from

a minimum of 300 nanoparticles for AuNRs and 1500 nanoparticles for AuNS. AuNR lengths and widths were measured with the image processing platform Macnification (Orbicule, OS X). AuNS dimensions were calculated from measured particle area using the particle analysis plugin available in ImageJ[116]. Statistical analysis performed using R.

### UV-Vis Spectroscopy

For AuNR absorbance spectral characterization, AuNPs (10 µL aliquots) were diluted with 990 µL DI water and placed in Eppendorf Uvette cuvettes. The absorbance spectra were acquired using a Beckman Coulter DU800 Spectrophotometer. Spectral measurements were recorded with 1 nm resolution with a range of 200 nm - 1100 nm. Before sample analysis, a solvent baseline measurement was recorded for use as a sample blank. AuNR aspect ratio measurements were calculated using the procedure outlined in [117]. AuNS particle diameters were calculated via fitting measured spectra to the Mie scattering model via Mathematica[118].

### Dynamic Light Scattering and Zeta Potential

Time resolved measurements of the AuNP hydrodynamic radius were obtained via dynamic light scattering (DLS) measurements using two instruments: a Wyatt Möbius (laser: 532 nm, 50 mW, $\theta = 163.5°$) and a Malvern Zetasizer Nano ZS (laser: 633 nm, 4 mW, $\theta = 173°$). For the Wyatt, the DLS acquisition time was 2 s and 10 acquisitions forming a measurement. Measurements were taken continuously for 15 min to monitor for time-dependent signal variations indicative of particle aggregation. The Malvern measurement duration was automatically determined with a cutoff defined as between 20 and 50 runs. The reported hydrodynamic radius for both measurements were calculated from the raw data using the cumulant method.

Both tools used phase amplitude light scattering (PALS) measurements to record AuNP mobility. The Wyatt used a 20 s PALS collection period, applied voltage intensity was 2.5 V, the electric field frequency was 10 Hz, and measurements were simultaneously recorded with the DLS measurements throughout the 15 min experiment. Malvern measurement duration was automatically determined with a cutoff defined as between 20 and 50 runs. All other parameters are automatically set. Zeta potential measurements were performed after the DLS measurements.

Measurements on the Wyatt were performed using a low-volume dip cell with a 60 µL sample volume. The Malvern measurements were taken using a plastic folded capillary cell with a sample volume of 1 mL. Each cell was cleaned before and after each measurement. The Wyatt dip cell was cleaned using the following procedure: 2 min DI rinse, 1 min Isopropyl Alcohol (IPA) rinse, and high-pressure drying with filtered house nitrogen (40 psi) until fully dry. The Malvern cell was cleaned by flushing 5 mL of DI, 1 mL of IPA, and 5 mL of DI through the capillary. All measurements were performed in triplicate.

### Capillary Zone Electrophoresis

A Hewlett Packard (now Agilent) Capillary Electrophoresis 3DCE system with a diode array detector (DAD) was used for all CE measurements. For each measurement, the DAD detector monitored five wavelength bands (260 nm, 488 nm, 520 nm, 550 nm, and 580 nm) ±10 nm simultaneously in real-time. Two identically prepared capillaries were used for all measurements with manually formed measurement windows. Capillaries were initially conditioned with a 5 min DI flush, 20 min NaOH flush, and a 10 min flush with the running electrolyte (10 mM borate buffer, pH 9.2). Each experiment preconditioned the capillary with a 3 min NaOH flush with a subsequent 3 min running electrolyte flush. Specific capillary dimensions and experimental conditions are detailed

in Table 3.2.

| CE Parameters | |
|---|---|
| Diameter (ID) | 50 µm |
| Length | 40.25 cm |
| Length to Detector | 31.75 cm |
| Applied Voltage | 16 kV |
| Injection Pressure | 15 kPa |
| Injection Time | 20 s |
| Temperature | 25.1 °C |
| Material | Fused Silica |

Table 3.2: Experimental conditions for the capillary electrophoresis measurements. All measurements were performed on an HP 3DCE system.

Optimization of injection conditions was conducted using a calibration sample of 1% Acetone, 50 µM FL, and 50 µM 6-FAM in 10 mM borate buffer with a 1 mL total volume. Selected injection pressure and time provided a maximized intensity peak with a gaussian plug shape. AuNP concentration was optimized for sensing and identified as 50 uL of concentrated stock solution diluted to a 1 mL final volume. No Acetone is present in AuNP solutions. The stock solutions were classified by Nanopartz such that they had similar optical densities enabling constant absorbance intensity measurements independent of nanoparticle shape / size via the CE DAD. Separation experiment length (time) was optimized to 12.5 min after varying experiment length from 7.5 min to 60 min. No peaks were observed via CE after 9.5 min for any AuNP sample.

Electroosmotic mobility was assessed using a calibration solution of 50 µM FL, 50 µM 6-FAM, 1% Acetone in 10 mM borate running buffer with a 1 mL total sample volume. All measurements were performed in triplicate. Calibration runs were performed after every 9 AuNP measurement runs to verify system performance and monitor drift in the CE system. Raw measurement data was smoothed via wavelet analysis[119] and analyzed using Matlab (v. R2014b), IgorPro (v. 6.1), and R (v. 3.2.2).

### Microchip Capillary Zone Electrophoresis

Microchip capillary electrophoresis measurements were conducted using a bespoke system built upon an inverted epifluorescent microscope (Olympus IX-71, Olympus, Inc.) with a 60X water immersion objective (UPLAPO-W 60X, Olympus, Inc.), laserport filtercube with fluorescent filters (Z488RDC, HQ525/50m, Chroma Technology), back illuminated EMCCD camera (Andor iXon Ultra 897, Andor), 0.5X demagnifier (Olympus, Inc.), automated stage (HLD117, Prior Scientific, Inc.), and 473 nm CW laser (Optotronics) as the excitation source for FITC-compatible fluorescent dyes. Excitation source power intensity limited to 5 mW to limit photobleaching and damage to optical components. Voltage is applied via a high voltage sequencer (LabSmith HVS448-6000D+LC). System is contained in a darkroom to eliminate stray light sources.

Borosilicate glass microfluidic cross-channel devices (Dolomite Ltd.) were used for all microchip capillary electrophoresis experiments. Fabricated using fusion-bonded D263 borosilicate glass wafers, the devices had the following channel lengths: North (N), South (S), West (W) channels - 5 mm (4.35 mm actual); East (E - separation) - 30 mm (29.35 mm actual). Microfluidic channels were wet-etched via hydrofluoric acid to a target depth of 20 µm. Starting channel width is 7 µm and the final width is 47 µm forming a 'D-shaped' cross-section profile. Bottom glass thickness is 0.5 mm and compensated by the correction collar on the 60X water objective. The microfluidic chip is held in a custom stainless steel / PEEK chipholder with integrated 60 µL reservoirs. The chipholder is cleaned prior to and after each experiment via manual washing with Alconox - Powdered Precision Cleaner (Alconox, Inc.) and subsequent flush with DI and IPA before drying with filtered high-pressure nitrogen.

Each microfluidic chip was conditioned prior to use using the following procedure: (1) DI channel hydration via capillary filling, (2) 5 min electroosmotic flow flushing with

DI (E: -300V, N/S/W: floating), (3) 30 min electroosmotic flow flushing with NaOH (E: -300V, N/S/W: floating), (4) 5 min electroosmotic flow flushing with DI (E: -300V, N/S/W: floating), 20 min electroosmotic flow flushing with running buffer (10 mM borate buffer, E: -300V, N/S/W: floating). Reservoir solutions are replaced every 5 min. all solutions are prepared with 0.2 µm filtered (190-9920, Nalgene) DI.

For all AuNP measurements, the camera was used with electron-multiplying (EM) gain set to 300 and a bias of +3 V. The exposure was set to 0.1 s with the detector positioned 16 mm from the cross-channel intersection. Additional experimental details are outlined in Table 3.3. The LabSmith sequencer was used to synchronize to the separation program a custom-fabricated laser shutter and the camera. This eliminated any delay between the application of the applied separation voltage and the start of detection while preventing possible photobleaching from scattered laser light.

| µCE Parameters | |
|---|---|
| Depth | 20 µm |
| Separation Length | 29.35 mm |
| Length to Detector | 16 mm |
| Applied Electric Field | -17.4 kV/m |
| Separation Time | 90 s |
| Temperature | 25 °C |
| Material | D263 |

Table 3.3: Experimental conditions for microchip capillary electrophoresis measurements.

Each measurement produced a single stacked .tif file of raw image intensity. These images were post-processed and analyzed using Matlab (v. R2014b), IgorPro (v. 6.1), and R (v. 3.2.2). The µCE solutions contain only FL and 6-FAM as mobility markers as the detection system uses fluorescence rather than absorbance rendering Acetone undetectable. The electroosmotic flow component is removed using the previously determined mobility values via CE for these markers.

**pH Determination**

Measurements were recorded using a calibrated pH meter (Oakton pH 11 Meter) in triplicate.

## 3.3 Results and Discussion

### 3.3.1 Characterization of Size and Polydispersity of Commercial AuNPs

The size distribution of eight distinct commercially synthesized (Nanopartz) AuNP samples (*Spheres*:NS10, NS25, NS60, NS100; *Rods*: NR25(700), NR25(980), NR40(700), NR50(700)) were characterized using UV-Vis spectroscopy, TEM, and DLS. These techniques comprise the primary and readily available suite of analytical methods for characterizing nanoparticles as reported in literature[120, 61, 121, 6].

UV-Vis absorbance spectroscopy was used to determine the localized surface plasmon resonance peak locations for the AuNP samples as shown in Figure 3.1. For the AuNS samples there is a single maxima, the location of which red-shifts with increasing AuNS diameter. The AuNR samples each exhibit two peaks as a result of their particle anisotropy with a transverse surface plasmon resonance peak (tSPR) located between 505 nm and 550 nm from the AuNR diameter and a longitudinal surface plasmon resonance peak (lSPR) from the AuNR length that red-shifts with increasing AuNR aspect ratio. As the location of these peaks relate to the fundamental morphology, particle composition, and dimensions of the nanoparticles, the measured spectra can be used to ascertain the size of the AuNPs via Mie scattering theory.

Mie scattering theory relates the optical properties of isolated colloids suspended in a medium to the colloid size with the extinction cross-section given by Equation 3.1

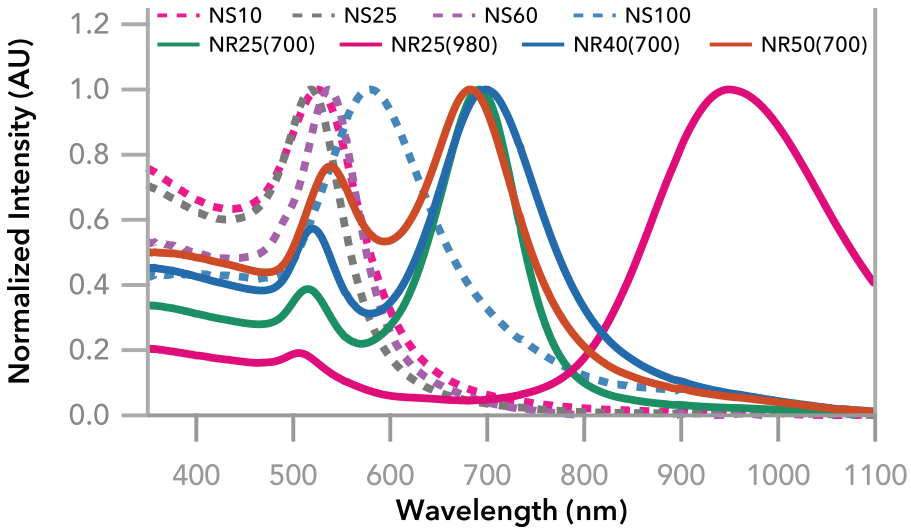


Figure 3.1: Spectra from UV-Vis absorbance spectroscopy measurements of the four populations of AuNS (NS10, NS25, NS60, NS100) and AuNRs (NR25(700), NR25(980), NR40(700), NR50(700)). The nanosphere spectra show the expected red-shift of the LSPR peak with the increase in nanosphere size. The nanorod populations have LSPR peaks nominally located at 700 nm and 980 nm, as ordered from the manufacturer. The location of this peak is aspect ratio dependent such that the three different nanorod populations (NR25(700), NR40(700), NR50(700)) have the same LSPR peak position, but different dimensions. AuNP samples are suspended in 10 mM borate buffer.

[122, 123].

$$C_{ext} = \frac{2\pi}{|k|^2} \sum (2L+1)\mathrm{Re}(a_L + b_L) \tag{3.1}$$

For this equation, $C_{ext}$ is the extinction cross-section, $k$ is the wave vector $k = 2\pi\sqrt{\frac{\varepsilon}{\lambda}}$, $a_L(R,\lambda)$ and $b_L(R,\lambda)$ are the scattering coefficients. $a_L(R,\lambda)$ and $b_L(R,\lambda)$ are defined in terms of Ricatti-Bessel functions as shown in Equation 3.2 and Equation 3.3.

$$a_L = \frac{m\psi_L(mx)\psi_L'(x) - \psi_L'(mx)\psi_L(x)}{m\psi_L(mx)\eta_L'(x) - \psi_L'(mx)\eta_L(x)} \tag{3.2}$$

$$b_L = \frac{\psi_L(mx)\psi_L'(x) - m\psi_L'(mx)\psi_L(x)}{\psi_L(mx)\eta_L'(x) - m\psi_L'(mx)\eta_L(x)} \tag{3.3}$$

Here the size parameter is defined as $x = kR$ and $m = \frac{\varepsilon}{\varepsilon_m}$ where $\varepsilon$ is the dielectric function of the colloids and $\varepsilon_m$ is the dielectric constant of the medium. For colloids such as gold nanospheres with radii significantly smaller than the wavelength of light ($\frac{R}{\lambda} < 0.1$) Equation 3.1 can be simplified by considering only the first electric dipole term (L=1)[124]. For gold nanoparticles, the experimental values from Johnson and Christy[125] are used for $\varepsilon_r$ and $\varepsilon_i$. The theoretical absorbance cross-section for a particular nanosphere size can be related to the measured absorbance spectra of a dilute nanosphere solution through Equation 3.4[124].

$$A = \frac{C_{ext}LN}{\ln(10)} \tag{3.4}$$

Where $L$ is the optical path length of the UV-Vis spectrophotometer and $N$ is the number of particles per unit volume. Using this method[118], AuNS diameters were calculated from the spectra in Figure 3.1 and provided in Table 3.4.

Gans[126] extended this theory from spheres to ellipsoidal particles and predicted the

| AuNS Size from Mie Scattering Theory | | |
|---|---|---|
| Sample | Diameter (nm) | Std. Dev (nm) |
| NS10 | 11.02 | 0.53 |
| NS25 | 15 | 4.82 |
| NS60 | 56.89 | 13.72 |
| NS100 | 96.43 | 2.94 |

Table 3.4: Calculated nanoparticle diameters for AuNS samples from UV-Vis absorbance spectroscopy using Mie scattering theory.

presence of two distinct surface plasmon modes: a transverse mode for the short axis (diameter) and a longitudinal mode for the long axis (length). First shown by Link[127] for AuNRs, the Gans theory can be used to theoretically simulate the absorbance spectrum of AuNRs as a function of aspect ratio. Calculating the extinction coefficient for AuNRs (approximated as prolate spheroids) is calculated via Equation 3.5:

$$C_{ext} = \frac{2\pi V N \varepsilon_m^{3/2}}{3\lambda} \sum_j \frac{\frac{1}{P_j^2}\varepsilon_i}{\varepsilon_r + (\frac{1-P_j}{P_j}\varepsilon_m)^2 + \varepsilon_i^2} \tag{3.5}$$

where $P_j$ is the depolarization factor and $V$ is the volume of the AuNR. For prolate spheroids, the depolarization factor is defined as:

$$P_{long} = \frac{1-e^2}{e^2}\left[\frac{1}{2e}\ln\left(\frac{1+e}{1-e}\right) - 1\right] \tag{3.6}$$

$$P_{short} = \frac{1 - P_{long}}{2} \tag{3.7}$$

where the ellipticity $e$ is:

$$e^2 = 1 - (AR)^{-2} \tag{3.8}$$

and $AR$ is the AuNR aspect ratio.

Whereas Mie scattering theory is often employed to estimate nanosphere size from UV-Vis absorbance spectra, using Gans theory to approximating AuNR aspect ratio is less common due to the challenges posed by particle geometry[122, 123]. For AuNRs, sample polydispersity and deviations of nanoparticle shape create different absorbance spectra than those calculated using Gans theory. Researchers[128] have demonstrated that Gans theory, when combined with a weighted-fitting algorithm, can estimate AuNR aspect ratio from UV-Vis absorbance spectra using only the longitudinal surface plasmon resonance peak providing a simple relationship between $\lambda_{max}$ and aspect ratio. However, other analytical approaches such as discrete-dipole approximation (DDA), T-matrix, and finite-difference time-domain (FDTD) have been used to provide more accurate approximations of AuNR aspect ratio. Based upon FDTD calculations, Hu *et al.*[117] describe an optical extinction spectroscopy (OES) method that uses the location of the AuNR longitudinal surface plasmon resonance (LSPR) peak and peak full-width half-max (FWHM) to determine the AuNR aspect ratio. Aspect ratios for each AuNR sample were calculated using this method and the AuNR spectra shown in Figure 3.1 as shown in Table 3.5.

| AuNR Size from Mie Scattering Theory | |
|---|---|
| Sample | Aspect Ratio |
| NR25(700) | 2.86 |
| NR25(980) | 5.35 |
| NR40(700) | 2.91 |
| NR50(700) | 2.98 |

Table 3.5: Calculated AuNR aspect ratios from UV-Vis absorbance spectroscopy using finite-difference time-domain calculations of AuNRs. Note this method yields a single value.

TEM analysis of the AuNP samples indicated that all samples were polydisperse with mean dimensions calculated as shown in Table 3.6. The relative standard deviation (RSD) is greater than 10% for the AuNS samples NS10, NS25, and NS60 and for AuNR samples NR25(700), NR40(700), and NR50(700). Typical RSD values for AuNR characterization

Table 3.6: Mean dimensions for AuNPs from TEM Analysis.

| TEM Analysis: AuNS | | | |
|---|---|---|---|
| Sample | Diameter (nm) | Std Dev. (nm) | RSD (%) |
| NS10 | 8.53 | 2.41 | 28.3 |
| NS25 | 18.92 | 3.52 | 18.6 |
| NS60 | 65.56 | 26.44 | 40.33 |
| NS100 | 108.32 | 10.37 | 9.57 |

(a) TEM Analysis of AuNS populations with mean diameter, standard deviation, and relative standard deviation (RSD).

| TEM Analysis: AuNR | | | | | |
|---|---|---|---|---|---|
| Sample | Diameter (mm) | Diam. Std Dev. (nm) | Length (nm) | Length Std Dev. (nm) | Max RSD (%) |
| NR25(700) | 32.17 | 6.15 | 73.24 | 12.04 | 19.1 |
| NR25(980) | 18.54 | 1.76 | 98.15 | 9.9 | 10.09 |
| NR40(700) | 47.13 | 5.62 | 106.64 | 15.6 | 14.63 |
| NR50(700) | 55.74 | 9.73 | 101.32 | 13.61 | 17.46 |

(b) TEM Analysis of AuNR populations with mean diameter, standard deviation, and relative standard deviation (RSD).

via TEM measurements are less than 12% [129]. The elevated RSD values for these AuNP samples indicates significant measurement variability. Histograms with relative density overlays of AuNS (Figure 3.2) and AuNR (Figure 3.3) TEM measurements reveal this variability results from sample polydispersity.

Figure 3.2 shows clear multimodal particle size distributions for each AuNS population except NS10. The NS10 distribution has only one primary distribution at 8.53 nm, but has a broad size distribution as observed via the RSD. The RSD, as defined by Eq. 3.9, provides an interpretation of the measurement variability with respect to the mean value ($\mu$) for a population. Due to the small diameter size of the NS10 sample, the apparently

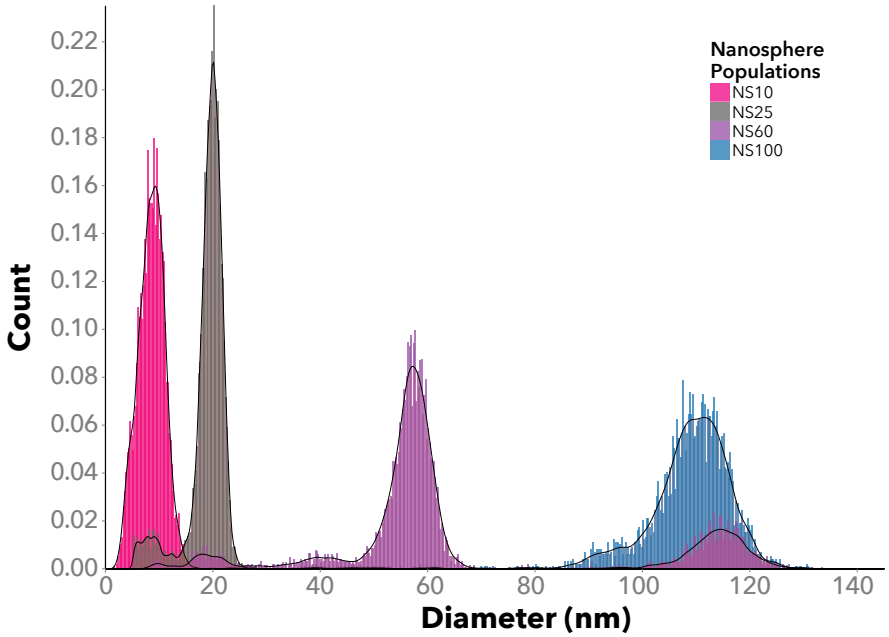


Figure 3.2: Density plot of measured diameters via Transmission Electron Microscopy of four AuNS populations (NS10, NS25, NS60, and NS100) with a histogram overlay. Although none of the AuNS populations are monodisperse, the NS10 population has the least variation in measured diameter with a mean diameter of 8.52 nm ±2.4 nm. The size distribution of the NS25 population is bimodal with a peak at 8.52 nm and 20.1 nm with a mean diameter of 18.92 nm ± 3.51 nm. The NS60 population has five distinct populations with four minor size distributions centered near 9 nm, 20 nm, 40 nm, and 112 nm, and a primary peak at 58 nm resulting in a mean diameter of 65.56 nm ± 26.44 nm. The NS100 population has a minor peak near 8 nm, but is primarily distributed at 108.28 nm ± 10 nm. Note that these measurements are of the AuNS core diameter. The histogram bin width is 0.25 nm. Number of particle measurements for the four populations are as follows: NS10 - 3960, NS25 - 7113, NS60 - 6079, NS100- 3964. Counts recorded from 20 different TEM micrographs per nanoparticle population from locations evenly distributed across a single copper TEM grid.

small standard deviation ($\sigma$) is actually a significant value.

$$RSD(\%) = \frac{\sigma}{\mu} \cdot 100 \tag{3.9}$$

The bimodal distribution of NS25 has two subpopulations of nanospheres centered at means 8.52 nm and 20.1 nm. The multimodal distribution for NS60 has nanosphere subpopulations centered at means of 9 nm, 20 nm, 40 nm, and 112 nm with the primary population located at 58 nm. This significant polydispersity is observed in the NS60 RSD value of 40.33%. The NS100 sample has less variability with an RSD value of 9.57%. However, as observed in Figure 3.2, the NS100 sample is not a normal distribution as with NS10, but has a distribution of sizes between 85 nm and 100 nm separate from the primary mean located at 108.28 nm.

Figure 3.3 shows distribution map of AuNR aspect ratios with density plots for both the diameter (Top) and length (Right). As aspect ratio is a derived value, a maximum RSD value is reported in Table 3.6B for each AuNR sample. From both these values and Figure 3.3, Each AuNR sample is polydisperse with broad distributions about a central mean aspect ratio with NR25/40/50(700) varied in both nanorod length and diameter as compared to N25(980) with a polydisperse length, but more monodisperse diameter. From Figure 3.3, we observe that NR25(700) and NR25(980) are distinct nanoparticle populations with respect to nanoparticle diameter and therefore aspect ratio. For NR25/40/50(700) samples to have the same LSPR peak (700 nm), the Gans extension to Mie scattering theory dictates that the populations must have the same aspect ratio. However, as the AuNR samples were expected to have narrow diameter distributions as a result of the synthesis process thereby forming distinct populations with similar spectral properties. As demonstrated by the spectral broadening of the AuNR absorbance peaks in Figure 3.1 and confirmed by Figure 3.3, the NR40/50(700) populations are nearly

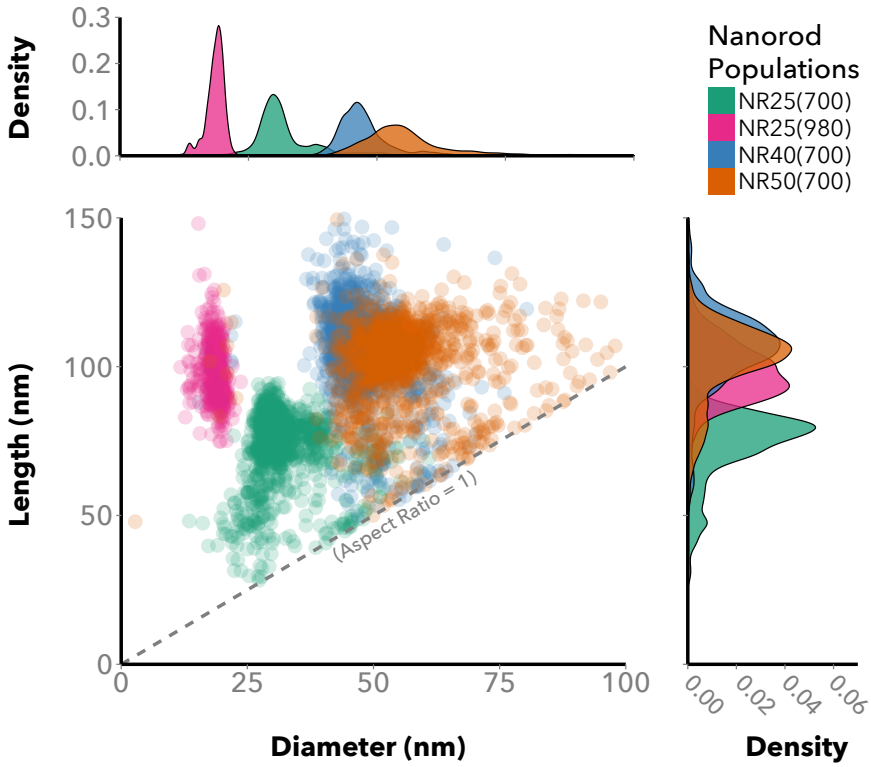


Figure 3.3: A scatter-plot of the measured aspect ratios (Length vs Diameter) via Transmission Electron Microscopy of four AuNR populations (NR25(700), NR25(980), NR40(700) and NR50(700)) with density maps of both the measured length and width. The dashed line indicates an aspect ratio of 1 (sphere) as the aspect ratio must be greater than 1. There is significant polydispersity in each AuNR population. The aspect ratios for each of the populations are as follows: NR25(700) is 2.34 $\pm$ 0.5, NR25(980) is 5.35 $\pm$ 0.87, NR40(700) is 2.31 $\pm$ 0.52 and NR50(700) is 1.88 $\pm$ 0.61. The density map of the measured diameter reveals that while the NR25(700) and NR25(980) populations are distinct, there is significant variation in the NR40(700) and NR50(700) diameters yielding little distinction between the two populations. The density map of the measured lengths indicate that the populations NR25(980), NR40(700), and NR50(700) all have similar lengths and polydispersity. Although similar in polydispersity, the NR25(700) nanorods are shorter with an increased differentiation from the other populations. Note that these measurements are of the AuNS core diameter. The histogram bin width is 0.25 nm. Number of particle measurements for the four populations are as follows: NR25(700) - 1156, NR25(980) - 370, NR40(700) - 1442 and NR50(700) - 1217. Counts recorded from 20 different TEM micrographs per nanoparticle population from locations evenly distributed across a single copper TEM grid. Note the NR25(980) measurements are less than the other populations due to unforeseen damage to the formvar coating on the copper TEM grid.

identical in composition with significant overlap in nanorod length and only moderate differences in diameter (NR40(700): 47.13 nm / NR50(700): 55.74 nm).

Comparing the AuNR samples using only aspect ratio measurements from TEM analysis with the theoretical fit from the UV-Vis spectroscopy measurements provides additional insight into the polydispersity of the AuNR samples. Table 3.7 shows the measured aspect ratios for each AuNR sample with each technique as well as the aspect ratio from manufacturer's certificate of analysis (CoA).

| Calculated AuNR Aspect Ratios | | | |
|---|---|---|---|
| Sample | AR - TEM | AR - UV-Vis | AR - Nanopartz |
| NR25(700) | 2.34 ± 0.5 | 2.86 | 2.88 |
| NR25(980) | 5.29 ± 0.87 | 5.35 | 5.84 |
| NR40(700) | 2.31 ± 0.52 | 2.91 | 2.925 |
| NR50(700) | 1.88 ± 0.61 | 2.98 | 2.8 |

Table 3.7: Calculated aspect ratios for AuNR samples via TEM analysis, UV-Vis spectroscopy analysis, and reported nanoparticle dimensions provided by the Nanopartz Certificate of Analysis.

As previously mentioned, the AuNR absorbance spectra from UV-Vis spectroscopy can be used to calculate nanorod aspect ratio. However, this technique is limited in providing insight into the sample composition to only offering a qualitative description of sample polydispersity through analysis of the lSPR peak band broadening. Figure 3.4 illustrates this limitation in that, as expected, NR25/40/50(700) have similar aspect ratios as they lSPR peaks located at 700 nm. Conversely, TEM analysis offers quantitative insight into the shape and size polydispersity of a AuNR sample through direct characterization of the metallic core dimensions. Aspect ratios from the TEM measurements can be used to develop a weighted approximation of the absorbance spectra (the inverse of the fitting technique). As observed in Figure 3.4, the calculated aspect ratios are significantly different than those from the UV-Vis technique. As a consequence, full characterization

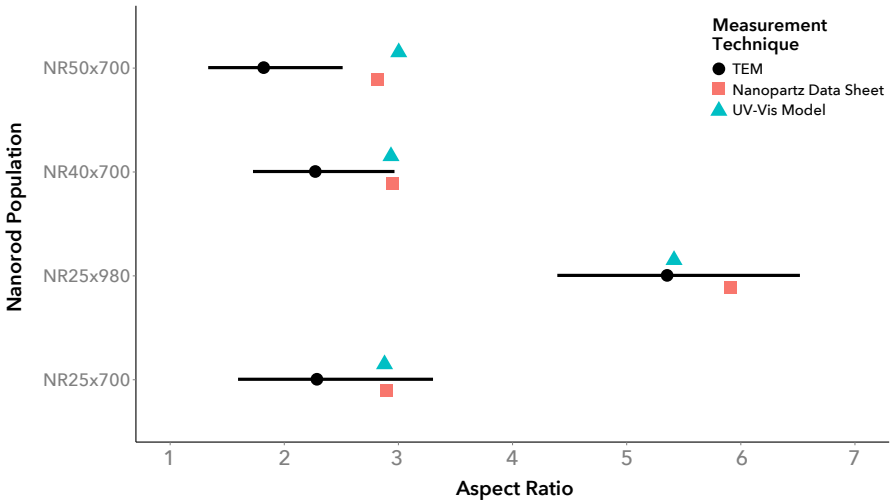


Figure 3.4: Comparison of AuNR aspect ratios calculated from Transmission Electron Microscopy and UV-Vis absorbance spectroscopy measurements with values reported from manufacturer certificate of analysis (Nanopartz). The TEM measurements of the nanorod core reveal significant population polydispersity. Nanopartz aspect ratio values are calculated from provided dimensions obtained via TEM analysis. UV-Vis absorbance spectroscopy aspect ratios obtained using previously described theoretical fitting procedure using lSPR peak location and peak FWHM. The difference between the UV-Vis and TEM aspect ratios are from the direct measurement of nanoparticle dimensions via TEM analysis. As the NR25/40/50(700) samples have similar lSPR peaks, according to Gans theory, these samples will have similar aspect ratios. Differences between the reported values from Nanopartz and the measurements recorded can not be attributed to changes in the nanorod populations as measured AuNRs exhibit no degradation or aggregation which.

of an AuNP population requires the use of additional measurement techniques such as Dynamic Light Scattering.

For the AuNP samples in this work, Dynamic Light Scattering (DLS) was used in addition to TEM and UV-Vis characterization to analyze the size distribution of the AuNP samples. Whereas TEM analysis directly measures the AuNP metallic core dimensions and UV-Vis spectroscopy uses the AuNP optical properties to determine the AuNP size / aspect ratio, DLS measurements measure the time-dependent fluctuations of light scattered by the nanoparticles in solution due to Brownian motion to assess particle size[121]. By measuring the signal rate-of-change in real-time, a fitting algorithm can be used to

relate the decay rate of the autocorrelation function of the scattered light intensity to the particle size distribution through the Stokes-Einstein equation (Equation 3.10)[130].

$$D_h = \frac{k_B T}{3\pi\eta D_t} \tag{3.10}$$

. Here, $D_h$ is the hydrodynamic radius, $k_B$ is Boltzmann's constant, $T$ is temperature (K), $\eta$ is the dynamic viscosity of the solvent, and $D_t$ is the translational diffusion coefficient. Specifically, by fitting either an single exponential function (Cumulants Analysis) or by using a Non-Negative Least Squares / CONTIN algorithm, the decay rate of the autocorrelation function is calculated and then converted to the translational diffusion coefficient via Equation 3.12[131]:

$$D_t = \frac{\Gamma}{q^2} \tag{3.11}$$

Where $\Gamma$ is the decay rate of the autocorrelation function and $q$ is the magnitude of the scattering vector defined as Equation 3.12:

$$q = \frac{4\pi n_0}{\lambda_0} \sin\left(\frac{\theta}{2}\right) \tag{3.12}$$

in which $n_0$ is the index of refraction for the solvent, $\lambda_0$ is the wavelength of incident light, and $\theta$ is the scattering angle.

For this work, two different DLS instruments were used to characterize the AuNP populations: the Malvern Zetasizer Nano ZS (industry standard) and the Wyatt Möbius. For both instruments, measured intensity data is interpreted via the Cumulants fit providing z-average (hydrodynamic diameter) and polydispersity index (PDI) where the PDI

is defined as:

$$PDI = \left(\frac{\sigma}{d}\right)^2 \tag{3.13}$$

where $\sigma$ is the standard deviation and d is the mean hydrodynamic diameter. Figure 3.5 shows the measured hydrodynamic radius for the AuNS samples along with the measured values from TEM and UV-Vis analysis. For each population, the DLS measurements report a significantly higher radius compared to the alternative measurement techniques, with the Malvern Zetasizer Nano ZS measuring higher hydrodynamic radius values and showing significant variability. Table 3.8 shows the specific measurements recorded by each instrument for the AuNS samples.

| | Malvern | | | Wyatt | | |
|---|---|---|---|---|---|---|
| Sample | Diameter (nm) | Std. Dev. (nm) | %RSD | Diameter (nm) | Std. Dev. (nm) | %RSD |
| NS10 | 42.97 | 20.53 | 47.78 | 41.65 | 21.12 | 50.7 |
| NS25 | 109.7 | 53.67 | 48.92 | 45.16 | 16.63 | 36.83 |
| NS60 | 102.2 | 39.14 | 38.3 | 81.33 | 24.35 | 29.94 |
| NS100 | 160.35 | 36.68 | 22.88 | 132.59 | 32.89 | 24.81 |

Table 3.8: AuNS diameters as measured by Dynamic Light Scattering.

The discrepancies between the DLS measurements and those from the other tools stems from the measurement technique itself. As described by Mahl *et al.*[61], DLS measurements typically report average particle sizes significantly larger than the core particle as DLS measures any surface coatings and the hydration layer in addition to the core nanoparticle. For their measurements of a bimodal distribution of gold and silver nanoparticles, they report that DLS values differed from other measurement techniques by a factor of 2-4. We observe similar deviations for the AuNS measurements but note that the Wyatt Möbius exhibited less variation and the reported hydrodynamic radii are closer to the values obtained via other characterization methods as compared to the

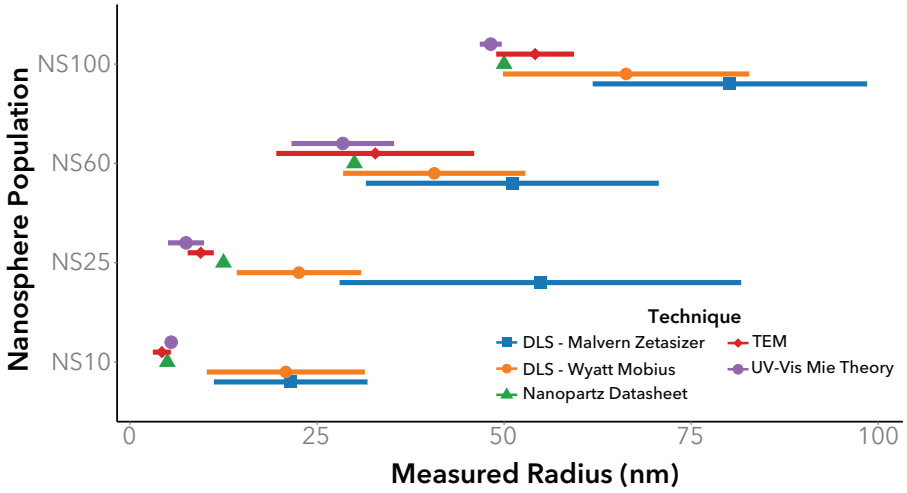


Figure 3.5: Comparison of the measured nanosphere radius for the four AuNS populations via Dynamic Light Scattering (Malvern, Wyatt), Transmission Electron Microscopy (TEM), and UV-Vis absorbance spectroscopy with reported certificate of analysis values (Nanopartz). The TEM measurements are of the AuNS metallic core, while both the DLS and UV-Vis measurements are of the nanospheres in suspension (10 mM borate buffer). For all nanosphere populations, the TEM and and UV-Vis measurements show good agreement. The reported value from the manufacturer also approximately matches these values except for NS25. However, independent of manufacturer, DLS measurements report increased particle sizes with a greater standard deviation than both TEM and UV-Vis. This variation stems from both the limitations of light-scattering methods in biasing measurements towards larger particles and the polydispersity of the nanosphere populations (as observed via TEM). This difference is not the result of particle aggregation or agglomeration as this phenomenon would also be observed in the UV-Vis spectroscopy measurements. The difference between the two DLS instruments stems from the increased sensitivity of the Wyatt Möbius.

Malvern Zetasizer Nano ZS.

The AuNR samples were also characterized via DLS measurements and subsequently compared to TEM measurements. Table 3.9 shows the specific measurements for the AuNR samples measured using the Wyatt Möbius and the Malvern Zetasizer Nano ZS.

| | Malvern | | | Wyatt | | |
|---|---|---|---|---|---|---|
| Sample | Diameter (nm) | Std. Dev. (nm) | %RSD | Diameter (nm) | Std. Dev. (nm) | %RSD |
| NR25(700) | 28.43 | 17.88 | 62.88 | 46.52 | 24.34 | 52.32 |
| NR25(980) | 30.315 | 21.47 | 70.83 | 43.34 | 29.96 | 69.13 |
| NR40(700) | 47.89 | 24.31 | 50.76 | 64.77 | 29.10 | 44.93 |
| NR50(700) | 60.96 | 29.15 | 47.82 | 79.46 | 31.91 | 40.16 |

Table 3.9: AuNR diameters as measured by Dynamic Light Scattering.

In the case of anisotropic particles, the measurements obtained by DLS are for a particle with the same average $D_t$ as a sphere since a sphere is the only particle shape that can be fully described by a single value[121]. The DLS measurements for AuNRs can not be compared to UV-Vis spectroscopy measurements without a priori information as Gans theory only yields an average aspect ratio, not dimensions, for a AuNR sample. TEM and the CoA dimensions were used to calculate the volume of a prolate spheroid (nanorod approximation) and subsequently used to calculate the radius of a sphere of equivalent volume. Specifically the equivalent radius ($R_e$) for a prolate spheroid is given as Equation 3.14[132]:

$$R_e = (ab^2)^{1/3} \tag{3.14}$$

where $a$ and $b$ are the radii of the long and short axes respectively. In contrast to the AuNS samples, when the DLS measurements for the AuNRs are compared to TEM and CoA values, the reported values do overlap as shown in Figure 3.6. However, the DLS measurements exhibit significant variability across both instruments as a consequence of

the spherical particle assumption and sample polydispersity.

### 3.3.2 Surface Characterization of Commercial AuNPs

In addition to assessing the size and polydispersity of a nanoparticle sample, accurately characterizing the nanoparticle surface is important for assessing nanoparticle colloidal stability in response to different suspension conditions (*i.e.* ionic strength, pH, other molecules / particles) or in understanding the efficacy of surface modification procedures (*i.e.* ligand exchange, molecule attachment, surface overcoating). Traditionally, nanoparticle surface properties are described by the widely-adopted zeta ($\zeta$) potential. The zeta potential for a nanoparticle measures the electrokinetic charge of a nanoparticle, specifically the value of the potential at the slipping-plane at the boundary between the particle's electric double layer and the ions in equilibrium surrounding the particle[74]. Consequently, the zeta potential is not necessarily a measure of the surface charge of the nanoparticle itself. The zeta potential is also highly dependent upon the properties of the solvent for the particles in suspension. As such, it is often used to characterize the stability of colloids in a suspension as it describes the potential between particles that keeps the colloids separated.

Nanoparticle zeta potential is typically measured using the Phase Analysis Light Scattering (PALS) technique where the intensity of light scattered by colloids in solution is monitored for small frequency shifts caused by particle motion under an applied electric field. By using a modulated reference beam mixed with scattered light signal, the particle velocity component due to the applied oscillating electric field can be quantified with the sign of the frequency shift determining particle direction. Specifically, Equation 3.15 is

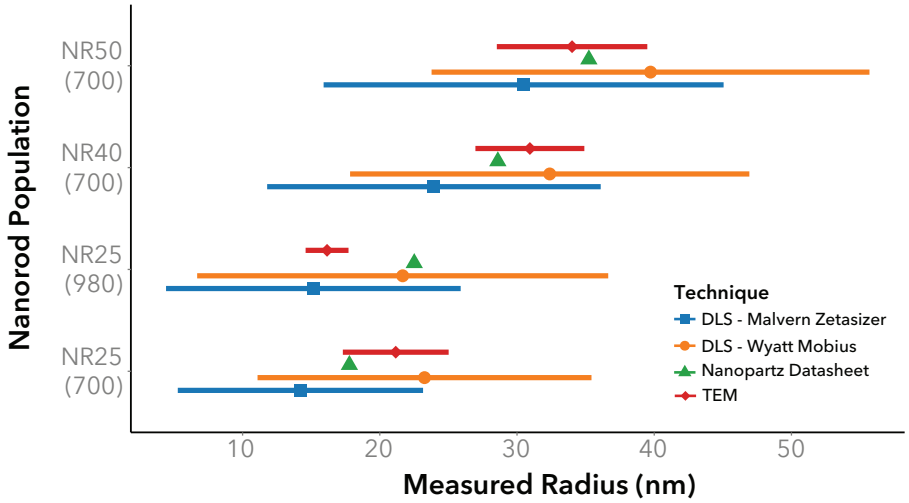


Figure 3.6: Comparison of the measured nanorod radius for the four AuNR populations via Dynamic Light Scattering (Malvern, Wyatt) and Transmission Electron Microscopy (TEM) with reported certificate of analysis values (Nanopartz). The TEM measurements are of the metallic nanorod core, while both the DLS and UV-Vis measurements are of the nanorods in suspension (10 mM borate buffer). For anisotropic particles DLS radius measurements are of an equivalent volume sphere. For accurate comparison, the TEM measurements are converted to yield the radius of an equivalent volume sphere by first calculating the volume of a prolate spheroid (approximate nanorod shape) from the measured nanorod dimensions. The TEM measurements have a smaller standard deviation compared to DLS measurements; however, in contrast to the nanosphere measurements, the DLS measurements overlap the recorded TEM measurements for all nanorod populations. However, independent of manufacturer, DLS measurements report increased particle sizes with a greater standard deviation than the TEM. This variation stems from the limitations of light-scattering methods in measuring anisotropic, polydisperse colloidal suspensions. The reported value from the manufacturer is based upon TEM measurements (also converted) and is contained within the standard deviation of the TEM measurements in all populations except NR25(980).

used to relate the measured frequency shift ($\omega$) to the particle velocity ($\vec{v}$)

$$\omega = \frac{2|\vec{v}|\sin\left(\frac{\theta}{2}\right)}{\lambda} \tag{3.15}$$

where $\theta$ is the measurement angle and $\lambda$ is the wavelength of illuminating light. It's important to note that the fundamental property measured with PALS is the particle electrophoretic velocity which is the particle velocity in response to an applied electric field[74].

$$\vec{v} = \mu\vec{E} \tag{3.16}$$

As shown in Equation 3.16, the particle electrophoretic velocity is defined by the applied electric field ($\vec{E}$) and the electrophoretic mobility ($\mu$). Accurately converting the particle electrophoretic mobility to zeta potential is a source of considerable research[74] due to a variety of factors including particle shape (Spheres[133, 134, 135, 136, 137], Anisotropic Particles[138, 139, 139, 140, 141, 142, 143, 144, 145, 146, 70, 147]), electrolyte composition[148, 149], particle surface coating[150] and charge [151, 152], particle concentration[153, 154, 155, 156, 157, 158, 159, 145], and composition[160, 161]. Even with considerable theoretical developments, typically either the Smoluchowski (Equation 3.17) or Hückel(Equation 3.18) formulas are used.

$$\mu = \frac{\varepsilon\varepsilon_0\zeta}{\eta} \tag{3.17}$$

$$\mu = \frac{2\varepsilon\varepsilon_0\zeta}{3\eta} \tag{3.18}$$

The suitability of the formula for a particular colloid system depends upon the particle electric double layer (EDL). Using the Debye screening length ($\kappa^{-1}$) and the particle

radius ($a$), the Smoluchowski formula is used for thin double layers ($\kappa a >> 1$) while the Hückel approximation is used for thick double layers ($\kappa a << 1$) as long as $|\zeta| \leq 25$mV for a given particle. Although throughout nanoparticle literature both formulas are found describing the same particles and solution conditions, in part due to the black-box nature of the PALS instruments, employing the wrong approximation can dramatically change the reported zeta potential for a given particle system. For particle systems that do not fall in either condition, the Henry formula is used as it bridges the two conditions for any ($\kappa a$) value and is given by Equation 3.19:

$$\mu = \frac{2\varepsilon\varepsilon_0\zeta}{3\eta} f_H(\kappa a) \tag{3.19}$$

Although Henry's function is the most frequently used since it can collapse to either the Smoluchowski or Hückel approximation, zeta potential is not trivial due to the wide variety of variables that can influence both the PALS slight scattering signal and subsequent interpretation from measured particle electrophoretic mobility. Furthermore, it has been shown that particles with different zeta potentials can still have the same electrophoretic mobility[162].

With the increasing importance of fully characterizing the surface properties of engineered nanoparticles for application development[6], researchers are transitioning to reporting nanoparticle electrophoretic mobility rather than the traditional zeta potential[163] as the mobility is directly measured via PALS.

As a consequence, the surface properties of the AuNPs in this work were characterized via PALS using both the Wyatt Möbius and the Malvern Zetasizer Nano ZS. We report the nanoparticle electrophoretic mobility rather than zeta potential for both AuNS (Table 3.10) and AuNR (Table 3.3.2) samples.

For all AuNP samples, the measured mean electrophoretic mobility is negative; how-

| | Malvern $(\mu m/s)/(V/cm)$ | | Wyatt $(\mu m/s)/(V/cm)$ | |
|---|---|---|---|---|
| Sample | Mobility | Std. Dev. | Mobility | Std. Dev. |
| NS10 | -0.91 | 1 | -0.69 | 0.46 |
| NS25 | -0.57 | 0.74 | -0.34 | 0.22 |
| NS60 | -0.61 | 1.15 | -1 | 0.33 |
| NS100 | -0.63 | 0.89 | -0.64 | 0.32 |

Table 3.10: AuNS electrophoretic mobility as measured by Phase Analysis Light Scattering.

| | Malvern $(\mu m/s)/(V/cm)$ | | Wyatt $(\mu m/s)/(V/cm)$ | |
|---|---|---|---|---|
| Sample | Mobility | Std. Dev. | Mobility | Std. Dev. |
| NR25(700) | -0.36 | 1.44 | -0.48 | 0.32 |
| NR25(980) | -0.83 | 1.28 | -0.91 | 0.71 |
| NR40(700) | -0.38 | 3.05 | -0.81 | 0.54 |
| NR50(700) | -0.42 | 1.61 | -0.48 | 0.19 |

Table 3.11: AuNR electrophoretic mobility as measured by Phase Analysis Light Scattering.

ever, the variability of these measurements, especially in the case of the Malvern Zetasizer Nano ZS, is significant. For the AuNS, the measurements from the Malvern Zetasizer Nano ZS had a standard deviation between 100-200 % of the observed value, while the Wyatt Möbius had standard deviations between 50-100 % of the observed value. For the AuNR samples, the WyattMöbius had similar standard deviations while the Malvern Zetasizer Nano ZS increased to 100-800%. Much of the variability in the measurement comes from the technique itself. As with DLS, a light scattering measurement will be biased by larger particles in solution due to the increase in scattering. This, combined with the known polydispersity and unknown efficacy of the proprietary surface coating performed by the manufacturer, makes this a difficult sample series to characterize leading to high variability in the measurement. The improvement of the Wyatt Möbius versus the Malvern Zetasizer Nano ZS is the result of both the use of 32 detectors in the Wyatt versus the Malvern and the ability to control the applied voltage to generate the electric field necessary for the PALS measurement. By using multiple detectors, the Wyatt instrument

is able to improve the sensitivity in detecting the frequency shift, decreasing variability. Additionally, a high applied voltage has been demonstrated to degrade the nanoparticles in solution, resulting in nanoparticle aggregation (therefore biasing the scattered light intensity). The Wyatt tool enables the precise control of the applied voltage, so for these measurements, we performed a set of optimization experiments (not shown) to determine the best applied voltage that prevented the degradation of the nanoparticle sample. Conversely, the Malvern Zetasizer Nano ZS, in favor of simple user control, does not offer that capability and thus some of that extreme variability might be the result of causing aggregation to occur in the nanoparticle samples. The challenge in interpreting these results stems from the fact that with the variability inherent in the system, the true mean particle mobility, or even whether the surface potential is positive or negative, is almost impossible to accurately determine. As a consequence, in order to precisely characterize the nanoparticle surface properties, an additional, independent method is required.

### 3.3.3 Electrophoretic Methods for Gold Nanoparticle Characterization

The surface properties of the AuNPs were also characterized using capillary electrophoresis (CE) and microchip capillary electrophoresis ($\mu$CE). Briefly, CE measurements are performed using a small-bore (20 - 100 $\mu$m inner-diameter, 350 $\mu$m outer-diameter) glass capillary, typically composed of fused-silica, filled with a buffer solution. A small amount of analyte is introduced into one end of the capillary via either applied pressure or electric field for analysis. Similar to the PALS, CE uses an applied electric field to induce analyte movement. However, whereas PALS uses an oscillating applied electric field, CE measurements use a steady-state applied voltage to generate the electric field across the length of the capillary. The velocity of the analyte is then determined by

measuring the time required for the analyte to pass a fixed-point detector, using either fluorescence or absorbance as the detection method. Using Equation 3.16 from PALS, the mobility of the analyte is determined from the measured velocity and the applied electric field.

CE is a separation technique in which the analyte can separate into its constitutive components as a result of the properties and composition of the analyte (*e.g.*, size, surface charge). The measured electrophoretic mobility is proportional to the force due to the applied electric field and inversely proportional to the drag forces the analyte experiences due to motion as described in Equation 3.20:

$$\mu_{ep} \propto \frac{F_E}{F_F} \tag{3.20}$$

where $F_E$ is the force due to the applied electric field and $F_F$ is force due to friction. For a spherical ion in solution, the force due to applied electric field is given as:

$$F_E = qE \tag{3.21}$$

and the force due to friction is given as:

$$F_F = -6\pi\eta r v \tag{3.22}$$

where $q$ is the charge of the ion, $E$ is the applied electric field, $r$ is the radius of the ion, $v$ is the velocity of the ion, and $\eta$ is the dynamic viscosity of the medium. In a CE measurement, these forces balance under steady-state conditions leading to the solution for electrophoretic mobility for an ion (Equation 3.23).

$$\mu_{ep} = \frac{q}{6\pi\eta r v} \tag{3.23}$$

From Equation 3.23, we observe that separation will occur under an applied electric field for particles that have the same charge but different radii or different charges but the same radii. We also note that the electrophoretic mobility depends both on the properties of the ion as well as the viscosity of the medium. This equation can also be used to classify particles by their mobility as highly charged, small particles will have high mobilities as compared to weakly charged, larger particles.

Fundamentally, a CE measurement (run) directly measures the apparent mobility $\mu_{app}$ of an analyte, not the electrophoretic mobility $\mu_{ep}$ due to the presence of bulk fluid flow in the capillary as well as analyte motion from the application of the electric field. Termed electroosmotic flow (EOF, $\mu_{EOF}$), this bulk flow arises from the movement of ions in the EDL along the capillary walls. The surface of the glass capillary is negatively charged due to the deprotonation of the silanol (SiOH) groups if the buffer has a pH $> 2$. Buffer cations, attracted to the negatively charged capillary surface, form both stationary layer and diffuse layer at the glass surface defined as the EDL. The bulk fluid movement, termed electroosmotic flow (EOF), is the result of the movement of the cations in the diffuse layer of the EDL, which, in turn, causes movement of the bulk, uncharged buffer solution in the capillary. The electroosmotic mobility is described by Equation 3.24:

$$\mu_{EOF} = \frac{\varepsilon \zeta_{wall}}{4\pi\eta} \tag{3.24}$$

where $\zeta_{wall}$ is the zeta potential at the wall of the capillary. For a general system, the wall zeta potential can be determined for a buffer system by using the current monitoring method to measure the velocity of the electroosmotic flow[164, 165]. The wall zeta potential is then calculated using the Smoluchowski equation (Equation 3.17) and the measured velocity.

As a result, the measured apparent mobility for an analyte is the combination of both

the electrophoretic and electroosmotic mobilities as shown in Equation 3.25.

$$\mu_{app} = \mu_{ep} + \mu_{eo} \tag{3.25}$$

For a CE system, $\mu_{app}$ is calculated via Equation 3.26:

$$\mu_{app} = \frac{v_{analyte}}{E} \tag{3.26}$$

where $v_{analyte}$ is the velocity of the analyte defined as Equation 3.27:

$$v_{analyte} = \frac{L_D}{t_{analyte}} \tag{3.27}$$

where $L_D$ is the length of the capillary (distance) the analyte peak travels to the detector and $t_{analyte}$ is the arrival time. For a neutral analyte, the $\mu_{app}$ is equal to $\mu_{EOF}$ as the movement of the neutral marker is the result of pure EOF flow.

For a CE measurement that has both the analyte of interest and a neutrally charged reference marker, Equation 3.25 can be written as Equation 3.28 using Equation 3.27 and the applied electric field (voltage ($V$) over the total capillary length ($L$)).

$$\mu_{app} = \frac{L_d L}{V(\frac{1}{t_{analyte}} - \frac{1}{t_{ref}})} + \mu_{ref} \tag{3.28}$$

For the CE measurements in this work, 6-Carboxyfluorescein and Fluorescein were used as fluorescent, highly-charged mobility reference markers in all AuNP samples. Although Fluorescein has an established electrophoretic mobility when suspended in 10 mM borate buffer[166], the electrophoretic mobility for 6-Carboxyfluorescein was determined from the apparent mobility by first measuring the EOF mobility using Acetone as a neutral marker and using Equation 3.25. Calibration measurements were recorded periodically to monitor for changes in EOF over the course of a series of measurements.

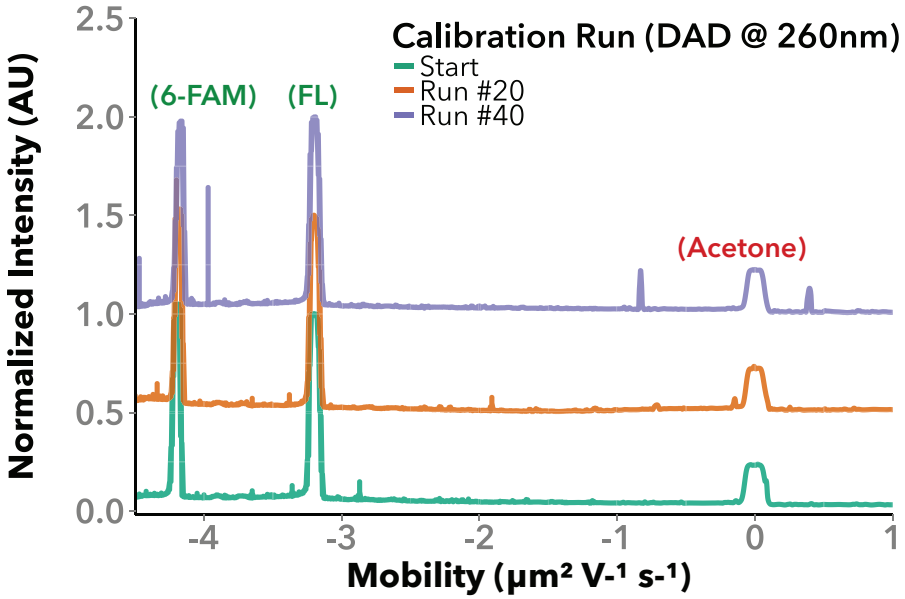


Figure 3.7: Electropherogram of calibration runs of electrophoretic mobility markers Acetone, Fluorescein (FL), and 6-Carboxyfluorescein (6-FAM) in a running buffer of 10 mM borate. Acetone provides a neutral mobility marker for the determination of the electro-osmotic mobility. The electrophoretic mobility of fluorescein is -3.20 $\mu m^2$ $V^{-1}$ $s^{-1}$ and 6-carboxyfluorescein is -4.29 $\mu m^2$ $V^{-1}$ $s^{-1}$. Changes in the capillary electrophoresis system are monitored through calibration runs at the beginning of a measurement series and after the completion of every 10 runs. Little variation is observed in apparent mobility. Traces are y-offset for clarity.

As shown in Figure 3.7, peak drift, indicative of a changing EOF, was not observed in the recorded electropherograms over one of the 40-run AuNP measurement series. From these calibration measurements, the electrophoretic mobility for fluorescein was measured to be -3.20 $\mu m^2$ $V^{-1}$ $s^{-1}$ and for 6-carboxyfluorescein to be -4.29 $\mu m^2$ $V^{-1}$ $s^{-1}$.

To prevent unexpected particle interactions, Acetone was not added to AuNP samples for measurement of the EOF. Alternatively, the values for the electrophoretic mobilities of the two fluorescent markers were used to solve for the EOF mobility as determined from the calibration measurements.

Normalized electropherograms for each of the four AuNS samples are shown in Figure 3.8. On aggregate, the electropherograms show close agreement in the electrophoretic mobility measurements for the two reference dyes with no observable variation between

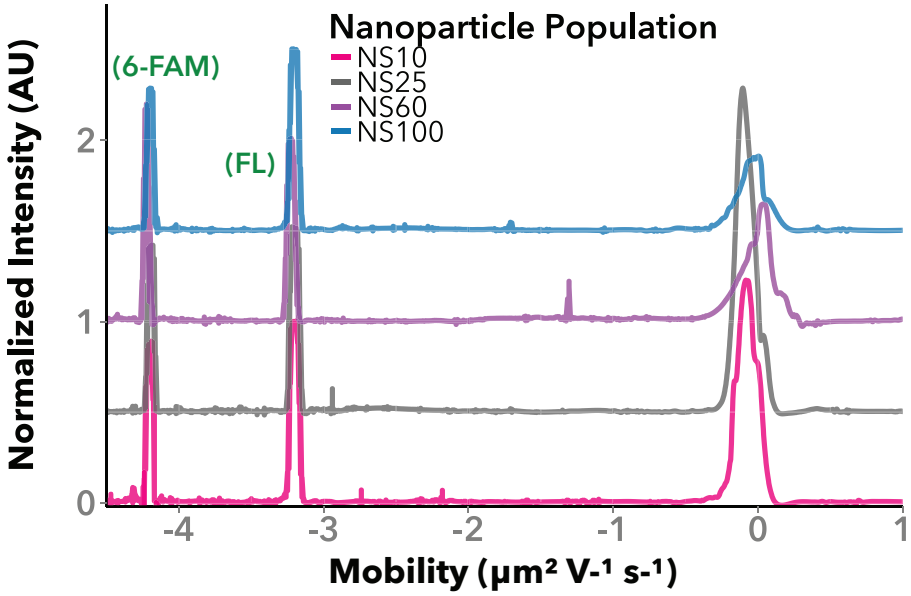


Figure 3.8: Separation electropherograms for each AuNS solution (NS10, NS25, NS60, and NS100) with added mobility markers (6-FAM, FL). Each AuNS population has a singular peak located near 0 $\mu m^2\ V^{-1}\ s^{-1}$ with a slight positive shift in peak location with increasing AuNS diameter. Multiple peaks are not observed within the broad AuNS peaks. The EOF flow component has been removed as previously described. Peak intensities normalized in relation to fluorescein peak (set to 1 AU). Traces y-offset for clarity. Signal: Absorbance measurement at 488 nm. Conditions: 20 s injection at 15 kPa, 10 mM borate running buffer, 16 kV applied voltage, 12.5 min separation length.

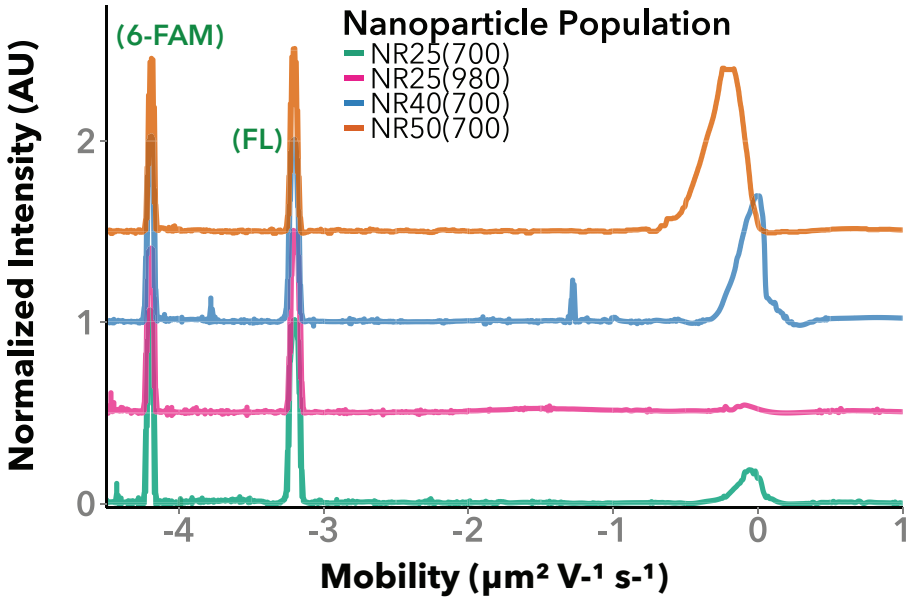


Figure 3.9: Separation electropherograms for each AuNR solution (NR25(700), NR25(980), NR40(700), and NR50(700)) with added mobility markers (6-FAM, FL). Each AuNR population has a singular peak located near 0 µm$^2$ V$^{-1}$ s$^{-1}$ with little variation in peak location for the NR25(700/980) and NR40(700) populations as compared to the negative shift of the NR50(700) peak. Multiple peaks are not observed within the AuNR peaks, but band broadening is observed for the NR40(700) and NR50(700) populations. The peak location of the NR25(980) is partially obscured due to y-axis scaling. The EOF flow component has been removed as previously described. Peak intensities normalized in relation to fluorescein peak (set to 1 AU). Traces y-offset for clarity. Signal: Absorbance measurement at 488 nm. Conditions: 20 s injection at 15 kPa, 10 mM borate running buffer, 16 kV applied voltage, 12.5 min separation length.

independent samples. Each AuNS population has a singular peak located near 0 µm$^2$ V$^{-1}$ s$^{-1}$ with a slight positive shift in peak location with increasing AuNS diameter. Multiple peaks are not observed within the broad AuNS peaks. The differences in peak intensity, although normalized to the Fluorescein peak (such that the Fluorescein marker has an intensity of unity), is not a quantitative comparison between samples due to each nanoparticle having an unknown number of fluorophores.

The AuNR samples were similar to the AuNS measurements as shown in Figure 3.9. As with the AuNS samples, each AuNR population has a singular peak located near 0

µm$^2$ V$^{-1}$ s$^{-1}$ with little variation in peak location for the NR25(700/980) and NR40(700) populations as compared to the negative shift of the NR50(700) peak. Multiple peaks are not observed within the AuNR peaks, but band broadening is observed for the NR40(700) and NR50(700) populations compared with the NR25(700/980) samples. The peak location of the NR25(980) is partially obscured due to significant differences in recorded peak intensity. This difference could be due to a difference in concentration or efficacy of the fluorophore coating on the nanoparticle surface.

These samples were also measured using $\mu$CE system. $\mu$CE measurement is a miniaturized version of CE in which a glass microfluidic device, typically of cross-channel geometry, is used instead of a fused-silica capillary. As a result of the smaller scale, $\mu$CE offers increased analytical speed and sensitivity through improved control over injected sample volume and smaller sample volumes[167]. In contrast to CE measurements, the analyte is injected into the separation channel via electrokinetics instead of pressure. For the $\mu$CE system used in this work, a fluorescent detection system is used instead of monitoring an absorbance signal. As a consequence, the measured electrophoretic mobilities of the fluorescent markers are used to determine the EOF mobility instead of a neutral marker. Although the separation channel is singificantly shorter than the fused-silica capillary (30 mm, 40.25 cm respectively), the applied electric fields were kept constant between systems at -17.4 kV/m.

The electropherograms for the AuNS samples are presented in Figure 3.10. In contrast to the CE measurements, the same AuNS samples have multiple peaks between 0 to -3.1 µm$^2$ V$^{-1}$ s$^{-1}$. The primary AuNS peak, located between 0 to -2 µm$^2$ V$^{-1}$ s$^{-1}$, becomes increasingly negative with increasing AuNS size. No peaks are observed above -3.2 µm$^2$ V$^{-1}$ s$^{-1}$ as verified through solutions with mobility markers absent (not shown).

Figure 3.11 provides a non-offset, y-axis truncated view of the peak mobility positions. From this, the clear evolution of the 0 to -2 µm$^2$ V$^{-1}$ s$^{-1}$ peak from the NS10/NS25

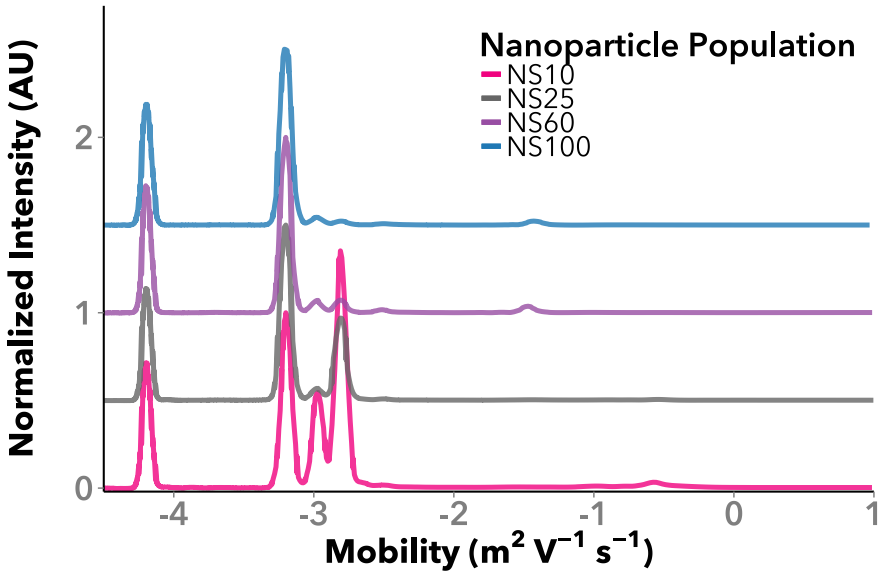


Figure 3.10: Separation electropherograms for each AuNS solution (NS10, NS25, NS60, and NS100) with added mobility markers (6-FAM, FL). Each AuNS population has multiple peaks. The primary AuNS peak located between 0 to -2 $\mu m^2$ $V^{-1}$ $s^{-1}$ becomes increasingly negative with increasing AuNS size. Peaks located between -2 to -3.2 $\mu m^2$ $V^{-1}$ $s^{-1}$ remain fixed in position but vary in intensity with intensity inversely proportional to AuNS size. No peaks are observed above -3.2 $\mu m^2$ $V^{-1}$ $s^{-1}$ as verified through solutions with mobility markers absent (not shown). Peak intensities normalized in relation to fluorescein peak (set to 1 AU). Traces y-offset for clarity. Signal: Fluorescence measurement with FITC fluorescence filter. Conditions: 90 s separation with an applied -17.4 kV/m electric field, 10 mM borate running buffer, detector located 16 mm from cross-section.

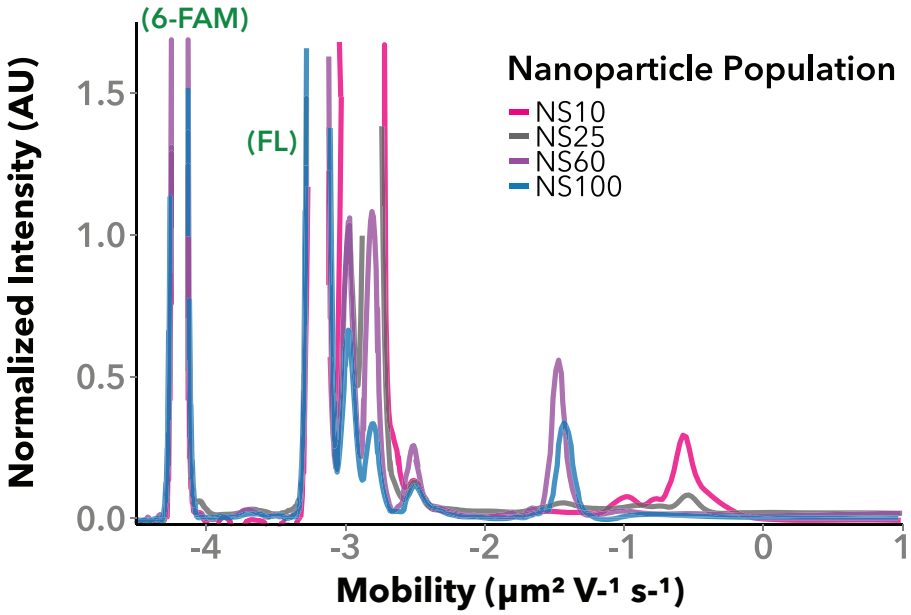


Figure 3.11: A non-offset, y-axis truncated view of the peak mobility positions for the AuNS samples. In this manner, the electropherograms show the clear evolution of the 0 to -2 µm$^2$ V$^{-1}$ s$^{-1}$ peak from the NS10/NS25 position located between 0 to -1 µm$^2$ V$^{-1}$ s$^{-1}$ to -1 to -2 µm$^2$ V$^{-1}$ s$^{-1}$ for the NS60/NS100 samples.

position located between 0 to -1 µm$^2$ V$^{-1}$ s$^{-1}$ to -1 to -2 µm$^2$ V$^{-1}$ s$^{-1}$ for the NS60/NS100 samples.

For the stationary peaks between -2.5 to -3.1 µm$^2$ V$^{-1}$ s$^{-1}$, Figure 3.12 provides a similar perspective. The intensities, although not quantitative due to an absence of information regarding the efficacy of the fluorescent surface coating, provides a qualitative means of comparison when normalized to the fluorescein peak. As shown, the peaks located between -2 to -3.2 µm$^2$ V$^{-1}$ s$^{-1}$ remain fixed in position regardless of AuNS sample, but vary in intensity with intensity inversely proportional to AuNS size.

Figure 3.13 truncates the y-axis to show the intensity continues to decrease for the NS60/NS100; however, the intensity for the NS60 peaks are approximately equal in intensity.

The AuNR samples were characterized in a manner similar to the AuNS populations. The recorded electropherograms for the samples, presented in Figure 3.14, show that in a

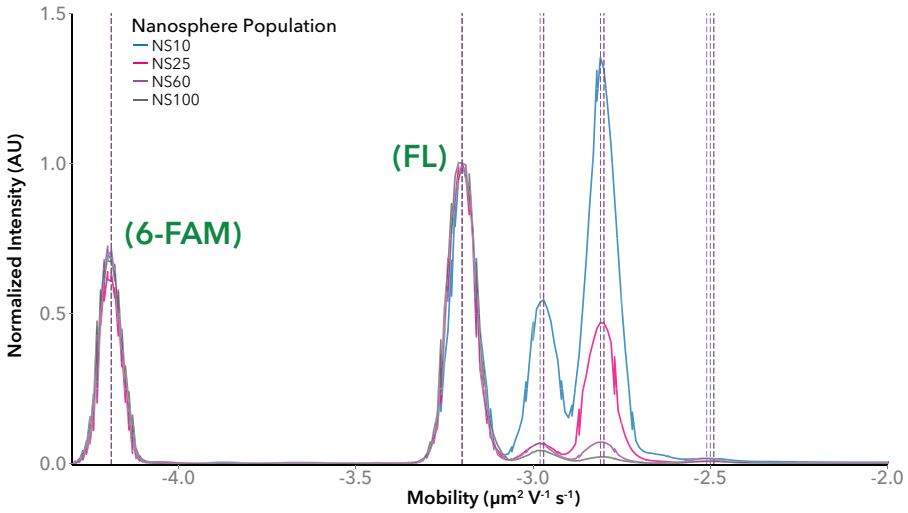


Figure 3.12: A non-offset, y-axis truncated view of the peak mobility positions for the AuNS samples between -2.5 to -3.1 $\mu m^2\ V^{-1}\ s^{-1}$. The peaks located between -2 to -3.2 $\mu m^2\ V^{-1}\ s^{-1}$ remain fixed in position regardless of AuNS sample, but vary in intensity with intensity inversely proportional to AuNS size. Vertical lines indicate detected peak location with color indicating nanoparticle population.

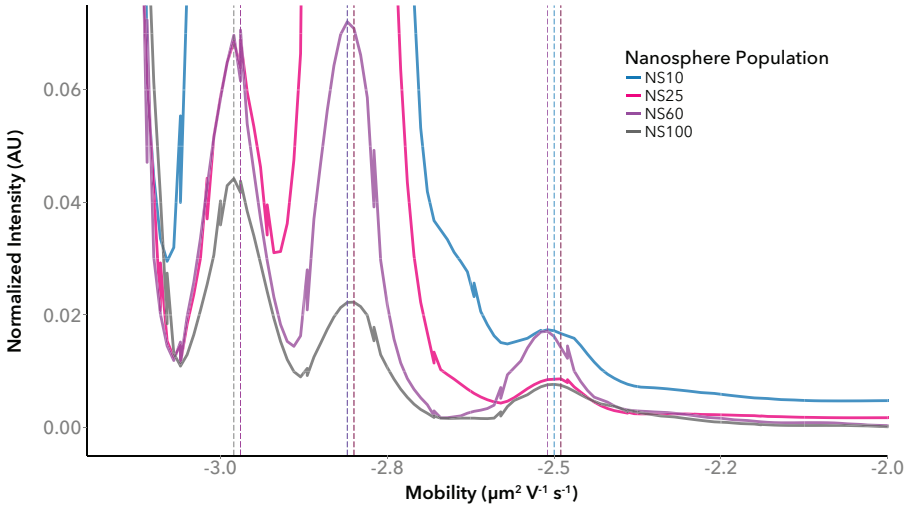


Figure 3.13: A non-offset, y-axis truncated view of the peak mobility positions for the AuNS samples between -2.5 to -3.1 $\mu m^2\ V^{-1}\ s^{-1}$ illustrating the continued decrease in intensity for the NS60/NS100 samples. Vertical lines indicate detected peak location with color indicating nanoparticle population.

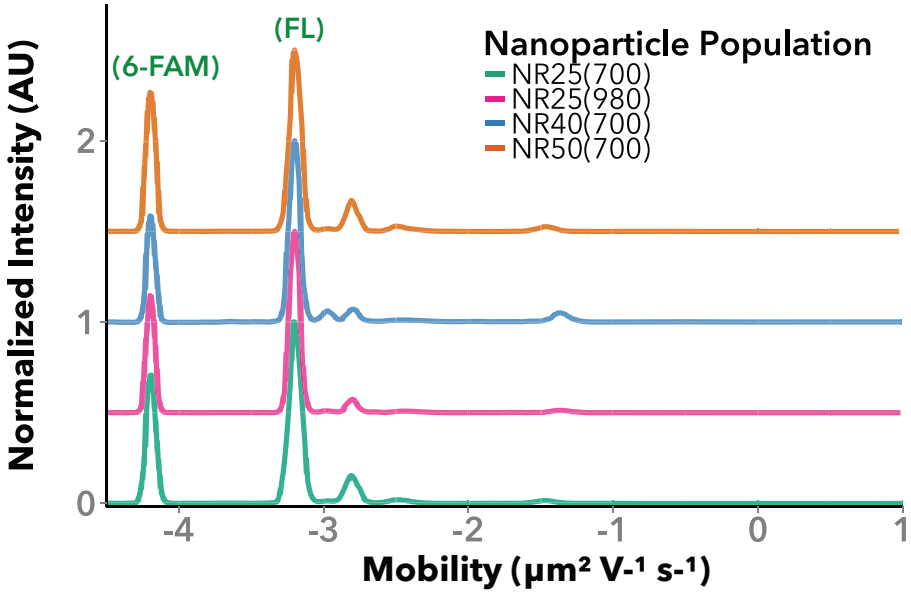


Figure 3.14: Separation electropherograms for each AuNR solution (NR25(700), NR25(980), NR40(700), and NR50(700)) with added mobility markers (6-FAM, FL). Each AuNR population has multiple peaks. The primary AuNR peak is located between -1 to -2 µm$^2$ V$^{-1}$ s$^{-1}$ but varies in position. As with the AuNS samples, peaks located between -2 and -3.2 µm$^2$ V$^{-1}$ s$^{-1}$ remain fixed in position but vary in intensity. No peaks are observed above -3.2 µm$^2$ V$^{-1}$ s$^{-1}$ as verified through solutions with mobility markers absent (not shown). Peak intensities normalized in relation to fluorescein peak (set to 1 AU). Traces y-offset for clarity. Signal: Fluorescence measurement with FITC fluorescence filter. Conditions: 90 s separation with an applied -17.4 kV/m electric field, 10 mM borate running buffer, detector located 16 mm from cross-section.

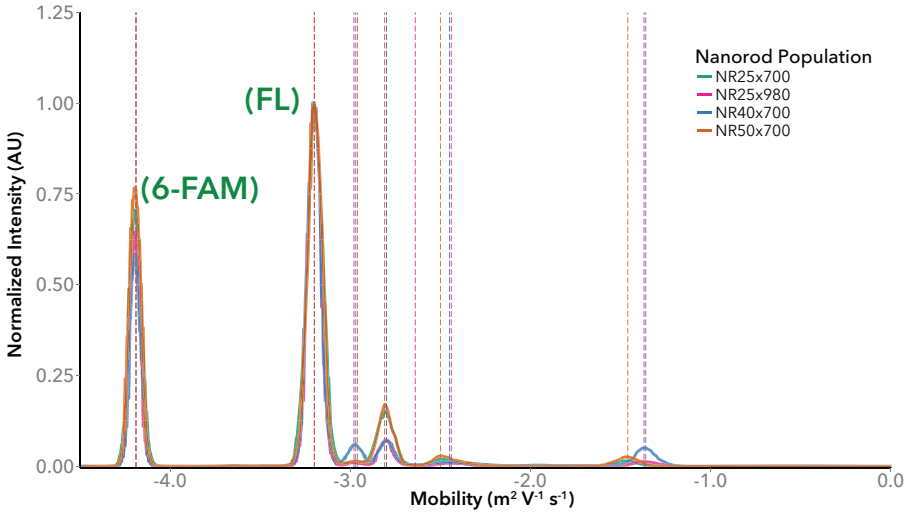


Figure 3.15: A non-offset view of the peak mobility positions for the AuNR samples. Whereas there is a clear evolution and shift of peaks in the AuNS samples, for the AuNR populations, the mobility peak locations exhibit little shift in response to AuNR size or shape, but instead, display clear differences in recorded peak intensities.

manner similar to the AuNS samples, but in contrast to the CE measurements, multiple peaks are present for each of the AuNR samples. The primary AuNR peak is located between -1 to -2 $\mu m^2\ V^{-1}\ s^{-1}$ but varies in position. As with the AuNS samples, peaks located between -2 and -3.2 $\mu m^2\ V^{-1}\ s^{-1}$ remain fixed in position but vary in intensity. No peaks are observed above -3.2 $\mu m^2\ V^{-1}\ s^{-1}$ as verified through solutions with mobility markers absent (not shown).

Figure 3.15 provides a non-offset, y-axis truncated view of the peak mobility positions for the AuNR samples. Whereas there is a clear evolution and shift of peaks in the AuNS samples, for the AuNR populations, the mobility peak locations exhibit little shift in response to AuNR size or shape, but instead, display clear differences in recorded peak intensities.

As seen in Figure 3.16, although some differences exist in both intensity and location for the peak near -1.5 $\mu m^2\ V^{-1}\ s^{-1}$ for the different AuNR samples, direct correlation can not be drawn between morphology and peak evolution as a result of the inconclusive

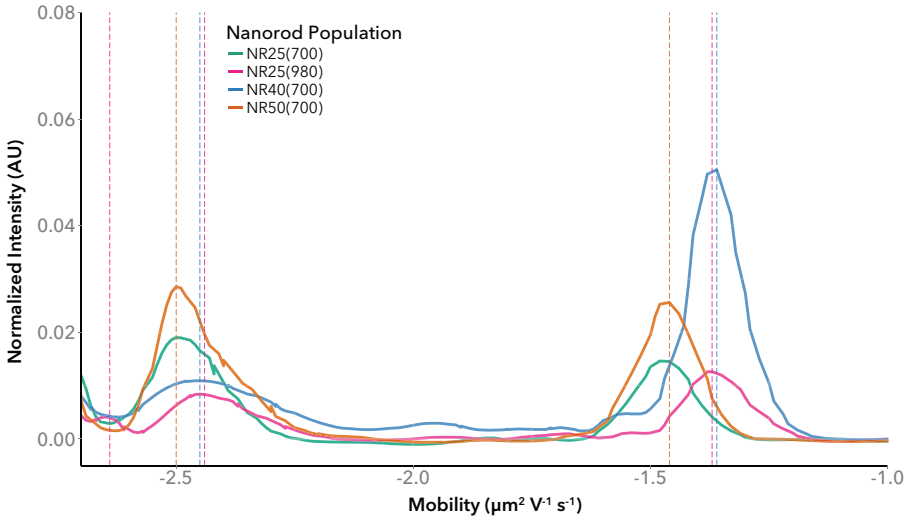


Figure 3.16: A non-offset, y-axis truncated view of the peak mobility positions for the AuNR samples between -1 and -2.7 µm$^2$ V$^{-1}$ s$^{-1}$. Whereas there is a clear evolution and shift of peaks in the AuNS samples, for the AuNR populations, the mobility peak locations exhibit little shift in response to AuNR size or shape, but instead, display clear differences in recorded peak intensities

relationship between the two properties.

The CE and $\mu$CE measurement techniques provide an alternative approach PALS for characterizing AuNP surface properties via analyzing the measured electrophoretic mobilities. Figure 3.17 shows the recorded mobilities for the AuNS samples while Figure 3.17 shows those for the AuNR samples. For both populations, the CE measurements indicate that the AuNPs are universally close to neutral in charge (electrophoretic mobility $\approx 0$ µm$^2$ V$^{-1}$ s$^{-1}$) in contrast to $\mu$CE and PALS measurements. Of particular interest is that for both populations, there is significant variation in the reported PALS measurements. Although the Wyatt Möbius demonstrates significantly less variability than the Malvern Zetasizer Nano ZS, both report at least a range of $\pm 0.5$ m$^2$ V$^{-1}$ s$^{-1}$ for each of the AuNP samples. For the $\mu$CE experiments, multiple peaks are observed for each AuNP sample indicative of variation present within each sample.

As seen in Figure 3.17, the primary peaks in each of the analyzed AuNS samples overlap with the PALS measurements for the NS10/25/60 samples, but the NS100 does

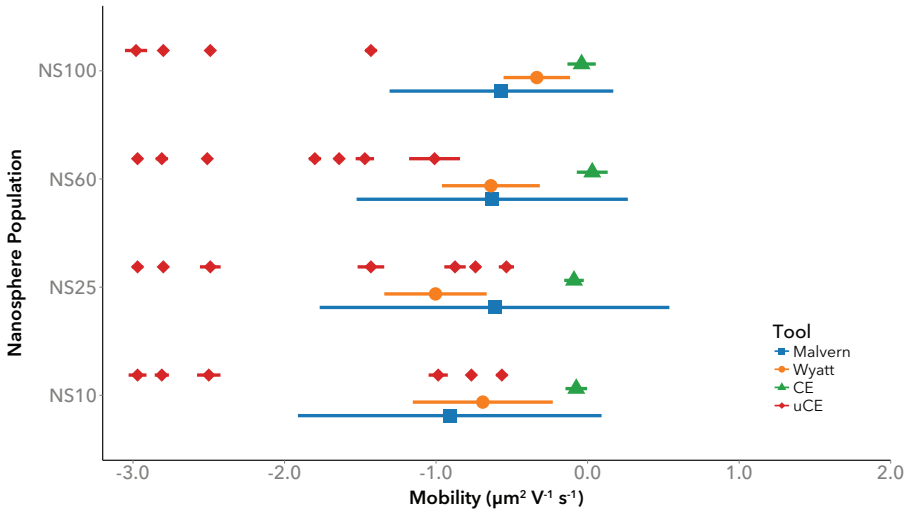


Figure 3.17: Measured electrophoretic mobilities for AuNS samples using PALS (Malvern, Wyatt), CE, and $\mu$CE. The CE measurements indicate that the AuNS are universally close to neutral in charge (electrophoretic mobility $\approx 0$ μm$^2$ V$^{-1}$ s$^{-1}$) in contrast to $\mu$CE and PALS measurements. Of particular interest is the significant variation in the reported PALS measurements. Although the Wyatt Möbius demonstrates significantly less variability than the Malvern Zetasizer Nano ZS, both report at least a range of $\pm 0.5$ m$^2$ V$^{-1}$ s$^{-1}$ for each of the AuNP samples. For the $\mu$CE experiments, multiple peaks are observed for each AuNP sample and indicative of variation present within each sample.

not. The presence of multiple peaks in the $\mu$CE measurements as well as some of the variation in the PALS measurements stems from the known polydispersity in the samples (Figure 3.2). Another source of variation could be non-uniform AuNS surface functionalization. Little is known about the commercial functionalization process due to trade-secret protections, but the manufacturer implies that the functionalization process involves modification of the surface with a propriety polymer coating instead of a silica encapsulation. Although claimed to be immune to salt-based aggregation, supported by measurements in this work in solutions with low ionic strength, selective degradation of the polymer on the AuNS surface or in variations in coating thickness within a functionalized batch would cause variations in the measured electrophoretic mobility. In contrast to PALS, $\mu$CE is a separation-based analytical platform and uses a high sensitivity fluorescent detection modality for this particular system of functionalized particles. Whereas with PALS the measurement is exponentially biased towards light-scattering by larger particles, the $\mu$CE measurement, as indicated by the multiple peaks, reveals the composition of the AuNS components. The limitation of this method, however, is that by using fluorescence as the detection modality in characterizing a polydisperse sample, the specific nature of the measured peaks can not be conclusively related to the actual AuNS sample composition. $\mu$CE measurements clearly show that the AuNS samples are polydisperse and that the polydispersity changes for each AuNS sample / AuNS size. However, relating peak position to sample composition is not possible without additional and specific detection, such as using absorbance spectroscopy to measure the LSPR peak wavelength in addition to fluorescence.

Similar differences are also observed for the measured AuNR samples as shown in Figure 3.18. However, in contrast to the AuNS measurements, the peaks present in the $\mu$CE measurements only overlap both PALS measurements for the NR25(980) and NR40(700) samples, while the NR25/50(700) samples overlap only the PALS measurements from the

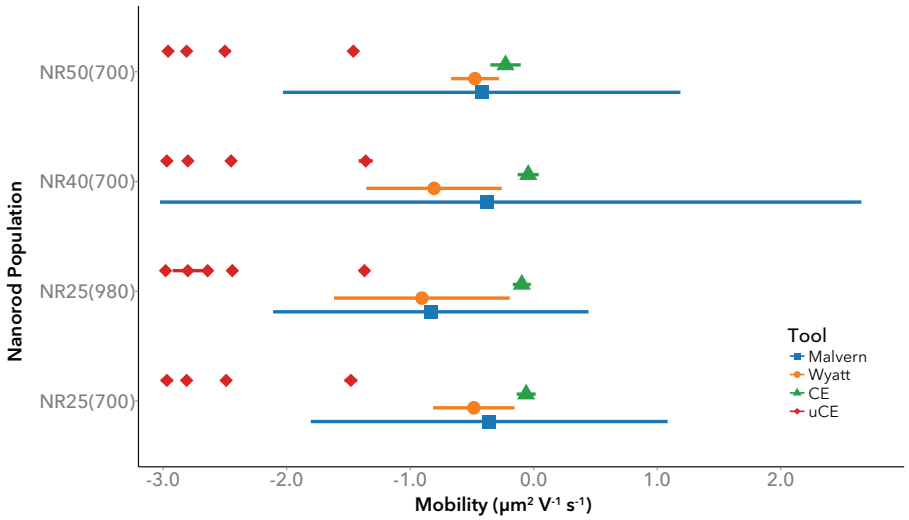


Figure 3.18: Measured electrophoretic mobilities for AuNR samples using PALS (Malvern, Wyatt), CE, and $\mu$CE. The CE measurements indicate that the AuNRs are universally close to neutral in charge (electrophoretic mobility $\approx 0$ $\mu m^2$ $V^{-1}$ $s^{-1}$) in contrast to $\mu$CE and PALS measurements. Of particular interest is the significant variation in the reported PALS measurements. Although the Wyatt Möbius demonstrates significantly less variability than the Malvern Zetasizer Nano ZS, both report at least a range of $\pm 0.5$ $m^2$ $V^{-1}$ $s^{-1}$ for each of the AuNP samples. For the $\mu$CE experiments, multiple peaks are observed for each AuNP sample with a single peak located and indicative of variation present within each sample.

Malvern Zetasizer Nano ZS. As with the AuNS samples, the variations in the PALS measurements may be the result of either the known polydispersity of the AuNR samples or in non-uniform surface functionalization. With the measurement of AuNRs, there is the additional concern of the particle anisotropy affecting the measurements due to variations in scattering from particle rotation, not simply particle motion due to the applied electric field. For the $\mu$CE measurements, the single primary peak varies only slightly between populations. Although specific identification as to the components of each peak can not be determined as previously discussed, TEM analysis (Figure 3.3) shows that the AuNR populations are not fully-segregated with regards to nanoparticle dimensions. This lack of distinction between populations would then yield similar characterization results, with differences arising from other factors such as polydispersity and surface functionalization. As with the AuNS samples, an additional detection system beyond fluorescence is required to better elucidate the composition of each of the recorded peaks.

It should be noted that the dramatic variation in measured values for the Wyatt Möbius as compared with the Malvern Zetasizer Nano ZS is the result of sample degradation due to the sampling methodology of the Malvern Zetasizer Nano ZS. The Malvern system applies a high, automatically calculated voltage to generate the electric field necessary for recording a measurement. The Wyatt system, due to a difference in capillary construction, requires a significantly smaller electric field and thus applied voltage to perform with similar efficacy. This difference is the presumed source of the excessive variation in the measurements produced by the Malvern system as when a large voltage was applied using the Wyatt system to the AuNP samples, high variability due to sample degradation was observed. We also note that comparison was not possible to the reported manufacturer CoA values as only the AuNP zeta potential was provided. As the manufacturer was unable to provide the raw data for the samples, electrophoretic mobilities could not be ascertained.

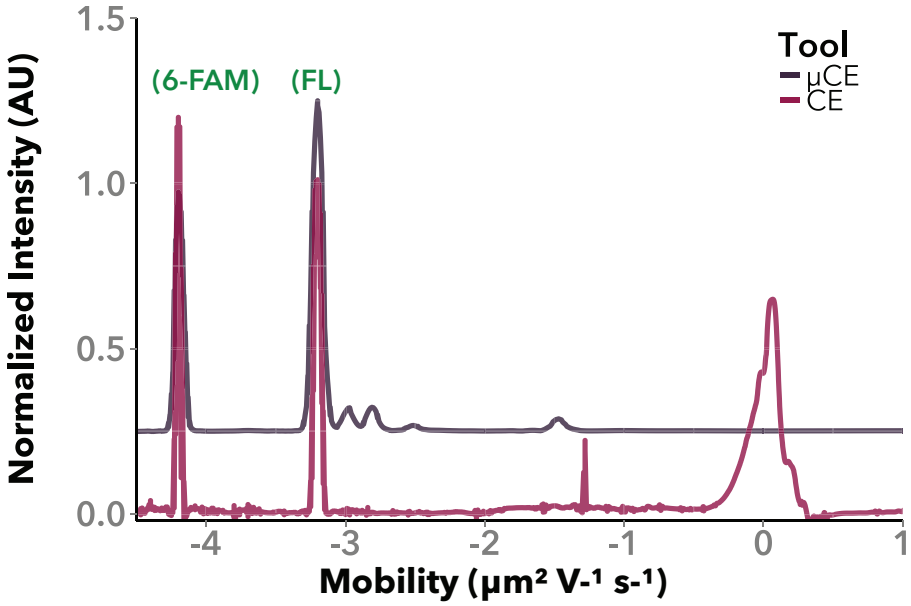


Figure 3.19: Comparison of the electropherograms from CE and $\mu$CE measurements of the NS60 sample.

For both AuNS and AuNR populations, the performance of the $\mu$CE and CE are markedly different. Whereas for all populations the CE measurements indicate that the AuNPs are almost neutral in charge, the $\mu$CE measurements indicate the opposite. Fundamentally the same measurement, but performed on different scales, close agreement was expected between the two methods. However, as shown in Figure 3.19, as comparison of the electropherograms from each method for the same AuNS sample reveal, the measured primary peak in CE does not appear in the $\mu$CE experiments, but nor do separations appear in the CE experiments. Exploring possible causes included the possibility of not fully injecting a sample into the $\mu$CE separation column due to the use of electrokinetic sample loading. This was proven to not be the cause of the discrepancies by using vacuum-driven flow to introduce the sample and then monitoring each of the channels at the cross-section for evidence of counter-flow of the analyte. As none was detected, it was concluded that the sample was indeed being fully introduced and characterized in the $\mu$CE experiments. Effect of possible concentration differences and sample

preparation was investigated by preparing a single sample and splitting it between the two measurement tools. No difference was observed between the recored measurements and the previously recorded measurements. One fundamental difference between the two methods is in the use of absorbance for detection in the CE system versus fluorescence in the $\mu$CE system. As the camera used in the $\mu$CE system has a quantum efficiency above 90% for between 480 nm and 720 nm, it is possible to detect extremely low levels of fluorescence. In contrast, the absorbance system used for the CE measurement can not detect concentrations of fluorescein below $\approx 10$ $\mu$M. It is also important to note that the sample to separation length ratio for the $\mu$CE system is significantly higher than the CE system. As an accepted practice for optimized detection, the analyte of interest should be about 2% of the total length of the capillary. However, due to the superior fluid handling and smaller volume of the $\mu$CE system, the analyte sample is only 0.16% of the total separation channel length. The result of this difference is that the $\mu$CE system provides additional opportunity for the analyte to separate. However, it's important to note that while this would increase the resolution, it does not change the fundamental electrophoretic mobilities of the AuNPs.

Previous studies of CE separations of AuNS have noted that without the addition of surfactant (SDS) to the running electrolyte, separations between different AuNS sizes did not occur[52, 168, 169, 170, 171, 172]. As described by Qu *et al.*[169], the surfactant molecules self-assemble on the surface of the AuNPs thereby forming a monolayer. The separation is the result of the proportional differences in surface charge to surface area due to the number of bound surfactant molecules. Although this separation provides a method for assessing the size distribution of a AuNP sample, it does not provide a compatible method for comparison to PALS measurements as the electrophoretic mobility is a result of bound SDS molecules, not the inherent AuNP surface functionalization.

## 3.4 Conclusion

The efficacy of many nanoparticle applications, especially those using AuNPs, depend upon accurate characterization of the size and polydispersity of a nanoparticle sample. This is especially true for commercially synthesized nanoparticles as they commonly used by non-chemists and potentially lack access to resources used by people developing their own nanoparticle samples. For a population of commercially obtained AuNS and AuNR samples, we rigorously analyzed the size and sample polydispersity using commonly available methods: TEM, UV-Vis Spectroscopy, and DLS.

As summarized in Figures 3.5 and 3.6, significant variability exists both within the sample population itself and between measurement techniques. This only further highlighted when the measured values are compared to the independent characterization provided in the CoA. The CoA values were calculated from reported TEM dimensions (without provided standard deviations) and show clear discrepancies with the values not only provided by our TEM analysis, but with other measurement techniques as well.

The AuNP surface properties were also characterized using PALS, CE, and $\mu$CE and reported using electrophoretic mobility rather than zeta potential to eliminate the assumptions of particle surface charge inherent in the zeta potential calculation. For both populations of AuNPs, the PALS measurements exhibited significant variability with the Wyatt Möbius having a narrower distribution than the Malvern Zetasizer Nano ZS. The CE measurements reported that all AuNPs were almost neutral in charge, in contrast to the values reported by both PALs and $\mu$CE. The $\mu$CE measurements showed component separation of the AuNP samples into smaller subpopulations. The primary subpopulation mobility measurements were similar to those reported by PALS for the AuNS sample, but reported a higher negatively charge for the AuNRs as compared to PALS. Without an alternative detection method to fluorescence for $\mu$CE, further elucidation of the nature

of these subpopulations is not possible. The presence of the subpopulations is to be expected as indicated by the polydispersity in the measurements from both TEM and DLS. The discrepancy between the electrophoretic mobilities reported by CE and $\mu$CE is hypothesized to be the result of a combination of lack of detection sensitivity in the CE system and increased resolution of the $\mu$CE system. Further work is required to better understand the nature of these differences.

From this extensive characterization of AuNP samples, two conclusions can be drawn: (1) regardless of the nanoparticle source, independent laboratory measurements outside of the manufacturer are necessary before any application use and (2) additional measurement techniques are required to fully characterize nanoparticle samples beyond spectral (UV-Vis), microscopy-based (TEM) analysis, and light scattering (DLS). As additional methods for nanoparticle characterization are being developed, the critical nature of characterizing nanoparticle size, polydispersity, and surface properties necessitates not only the standardization of nanoparticle characterization methods, but also the use of multiple, alternative characterization techniques beyond the current heavy reliance upon TEM and DLS/PALS analysis.

# Chapter 4

# Quantification of Colloidal Stability of Gold Nanoparticles via UV-Vis Spectroscopy

## 4.1 Motivation

Engineered nanoparticles (NPs) exhibit unique size-dependent thermal, electrical, chemical, and optical properties[173] that enable their use in a broad array of applications in fields as diverse as medicine (biosensing,[87] diagnosis,[90] therapeutics[174]) and chemical analysis.[94] The efficacy of NPs in each application is intrinsically linked to their stability in suspension;[175, 174] however, small changes to the solution (*e.g.* background salt concentration, temperature, pH) or changes to the NPs (*e.g.* surface coating or concentration) can substantially affect stability.[122] For example, in the case of gold nanorod (AuNR) stability, researchers have studied individually the effects of sample purification,[176, 177, 178, 179, 180, 181, 182] surface coating,[177, 183, 184, 185, 186, 182, 175] solution pH,[187, 188, 189, 190, 191, 192, 193, 194, 195, 181, 196] presence

of salt,[197, 183, 176, 195, 198, 179, 199, 200, 185, 181, 84] temperature,[201, 181] and solvent composition.[198, 184, 181, 186, 202]

Although colloid science is a well-established field, aggregation characterization of NPs in response to different destabilizing factors is not yet a standardized process.[173, 120] Table S1 in the Supplemental Information shows the common methods utilized in colloidal stability studies, particularly those focused on AuNRs, including the physical property measured, features of each method, and their limitations. One of the most developed, non-destructive analytical techniques is UV-Vis spectroscopy, which measures the changes in transmitted light due to the light scattered (turbidimetry) or absorbed (absorbance) by NPs in suspension.[203] Turbidimetry is an established method for assessing colloidal aggregation, especially for micron-sized particle systems.[204, 205, 206] However, since the measured signal changes both with particle volume-fraction and size, turbidimetry is limited to qualitative measurements when both parameters change simultaneously.[204] For plasmonic nanoparticles that exhibit strong light absorbance, UV-Vis absorbance spectroscopy overcomes this limitation as the absorbance response is strongly coupled with physical properties of the nanoparticle itself.

For noble metal nanoparticles this strong light absorbance results from their surface plasmon resonant properties. Specifically, noble metal nanoparticles exhibit surface plasmon resonance (SPR) absorption with the SPR frequency highly dependent on the nanoparticle size, shape, aspect ratio, and composition.[207] In particular, noble metal nanorods exhibit tunable SPR absorption in the visible spectrum [90] with localized surface plasmon resonance (LSPR) absorbance peaks corresponding to both their diameter (transverse surface plasmon resonance peak - tSPR) and length (longitudinal surface plasmon resonance peak - lSPR). There have been many studies, both theoretical and experimental, that have characterized changes in spectral absorbance and mapped them to both physical changes to the AuNRs as well as their behavior in suspension,[207, 208]

which, in turn, yields information regarding colloidal stability.

Weisbecker was first to define a "flocculation parameter" (FP)[209] based upon changes to the UV-Vis absorbance spectra of gold nanospheres (AuNS). This parameter incorporates both particle aggregation (irreversible) and agglomeration (reversible) and is calculated by integrating the measured absorbance values from 600 nm to 800 nm and increases as "flocculation" increases[209]. Mayya[210] proposed a modification to the FP by first normalizing the AuNS absorbance spectra using the peak LSPR intensity and then subtracting the integrated area from 600 nm to 800 nm for a sample from a reference spectra to account for any decreases in AuNS concentration over time due to flocculation. This modified FP has continued to be used by groups to characterize the flocculation of AuNS under different conditions[211]. However, this method is limited to characterizing spherical particles as changes in the selected wavelength range correspond directly to the growth of AuNS aggregates through the resulting band broadening and red-shift of the LSPR peak [212].

With regards to anisotropic particles, particularly AuNRs, researchers have used several different methods to relate aggregation behavior to spectral changes. Universally, researchers use the lSPR peak present in the AuNR absorbance spectra and measure either the lSPR peak intensity [176, 177], the ratio of the lSPR peak and tSPR peak intensities[213], or percent decrease of intensity at the original lSPR peak wavelength[183, 191]. Recently, Kah[175] proposed a derivative method based upon the work of Weisbecker *et.al.*[209] to monitor AuNR aggregation by integrating the area under the lSPR peak normalized to peak intensity. Kah redefines the FP as an aggregation index (AI) and uses this measure of the peak spectral broadening as an indication of AuNR stability in suspension. However, due to the specific definition of the index and the lack of a referential measurement, the AI fails to accurately and quantitatively capture the aggregation behavior of AuNRs. Therefore, a unified, robust, generalizable assessment

method of instability in nanoparticle colloidal suspensions is required.

We define a *Particle Instability Parameter* (PIP) as a universal method for quantitatively characterizing stability of plasmonic materials based upon UV-Vis absorbance spectroscopy that is both independent of the colloid system and fully captures the evolution of the system over time. In the next section we present our methodology and results that support the development of the PIP. We demonstrate the efficacy of this method through a systematic characterization of AuNRs over a variety of salts, buffers, and pH conditions. We describe the influence of sample preparation, handling, and methodology in performing stability studies of plasmonic colloids. We reaffirm the importance of characterizing the concentration of free surfactant (Cetyltrimethylammonium bromide - CTAB) in solution and its influence on AuNR colloidal stability. Finally, our work is contextualized within the literature of AuNR stability research and we compare methodologies and AuNR stability results.

## 4.2 Experimental Section

### 4.2.1 Materials

Cetyltrimethylammonium bromide (CTAB, H9151), Gold(III) chloride trihydrate ($HAuCl_4 \cdot 3H_2O$, 520918), silver nitrate ($AgNO_3$, S8157) were obtained from Sigma-Aldrich and used as received. Sodium borohydride ($H_4BNa$, S678), ascorbic acid ($C_6H_8O_6$, A61) were obtained from Fisher Chemical and used as received. Sodium chloride (NaCl, S271), sodium bromide (NaBr, S255), sodium tetraborate decahydrate ($B_4Na_2O_7 \cdot 10H_2O$, S249), Tris Base (BP152), HEPES (BP310), sodium acetate trihydrate ($CH_3COONa \cdot 3H_2O$, S608), hydrochloric acid (HCl, A144), sodium hydroxide (NaOH, S318) were all obtained from Fisher Chemical and used as received. All glassware used for AuNR synthesis was

cleaned with aqua regia and rinsed with Millipore 18.2 MΩ·cm DI water. All suspensions were prepared using Millipore 18.2 MΩ·cm DI water.

### 4.2.2 Methods

#### Nanorod Synthesis

AuNRs were synthesized using the seed-mediated method first described by Murphy[214] and El-Sayed[215]. Briefly, a seed solution was prepared by adding 200 $\mu$L of 0.01 M $HAuCl_4$ to 9.75 mL 0.1 M CTAB with vigorous mixing. 600 $\mu$L ice cold 0.01 M $NaBH_4$ was added and mixed for an additional 2 min during which the solution turned a dark brown. The seed solution was kept in a 33 °C incubator for 2 h before subsequent use. The AuNR growth solution was prepared by adding 400 $\mu$L 0.01 M $AgNO_3$ to 95 mL 0.1 M CTAB in a glass Erlenmeyer flask with vigorous mixing. 5 mL of 0.01 M $HAuCl_4$ was added to this solution with vigorous mixing. With the addition of 550 $\mu$L of freshly prepared 0.1 M ascorbic acid the solution turned clear. 120 $\mu$L of the seed solution was added to this solution and after gentle mixing, the solution was left overnight (16 h) in a 33 °C incubator. 15 reactions were performed simultaneously to synthesize a final volume of 1.5 L of AuNRs. After synthesis, AuNRs were aliquoted into 25 mL batches and purified once via centrifugation (14k RCF, 20 min) using a Sorvall Legend X1 centrifuge with Fiberlite 6×100 mL rotor. Synthesized AuNRs had dimensions of 45±8 nm × 17±4 nm as measured via TEM.

#### Buffer Preparation

Stock solutions were prepared at concentrations of 2 M, 1 M, 200 mM, 100 mM, 20 mM, 2 mM to be diluted 1:1 to the desired concentrations upon the addition of an AuNR suspension. The supplemental info section contains further information regarding buffer

preparation.

### Physical Characterization

Transmission electron microscope (TEM) micrographs were taken using a FEI Tecnai G2 Sphera Microscope. TEM grids were prepared by drop-casting 10 $\mu$L of AuNRs onto a TEM copper grid (400 mesh, 01822, Ted Pella). AuNR dimensions were calculated from the average of 3000 AuNR measurements.

### Dynamic Light Scattering

Time resolved measurements of the AuNR hydrodynamic radius were obtained using a Wyatt Mobius with cuvette attachment. Each recorded measurement consisted of 4 sub-runs with a 2 s sample integration time taken continuously at 30 s intervals for 15 min from the introduction of the analyte to a AuNR suspension. The reported hydrodynamic radius was calculated from the raw data using the cumulant method.

### UV-Vis Spectroscopy

For AuNR absorbance spectral characterization, AuNRs (1 mL aliquots) were centrifuged into pellets (14000 RCF, 4 min) and the supernate removed. The samples were resuspended in 1 mL DI water and placed in Eppendorf Uvette cuvettes. Samples were prepared to fully sweep all concentrations of a parameter (*e.g.* salt, pH) in triplicate in a single experiment to eliminate operator bias. We note that the concentration of free-CTAB in solution was held constant across all measured solutions as described in additional detail in the SI.

The absorbance spectra were acquired using a Shimadzu UV-1800 Spectrophotometer. Spectral measurements were recorded with 1 nm resolution with a range of 300 nm - 1100 nm. Before sample analysis, a solvent baseline measurement was recorded for use as a

sample blank. For AuNR stability analysis, measurements were recorded immediately after the addition and mixing (5 s, vortex) of the analyte into the AuNR sample. A 5 s wait time before starting the acquisition was used to ensure the absence of microbubbles in the cuvette as a result of vortex mixing. Acquisition occurred at 1 min intervals for the first 10 min followed by a measurement at 15 min continuing at 15 min intervals until 2 h with a final measurement at 24 h.

**Free-CTAB Analysis**

For assessment of the influence of CTAB on colloidal stability, aliquots of AuNRs were purified as described, but resuspended in 1 mM CTAB solution. Solutions of NaCl at 2 M, 1 M, 200 mM, 20 mM, 2 mM concentrations were added in a 1:1 ratio to the prepared aliquots and analyzed using both DLS and UV-Vis spectroscopy techniques.

**Gold Nanorod Concentration Analysis**

For determination of AuNR concentration influence, aliquots of diluted AuNR suspensions were prepared. Initial stock AuNR concentration estimated to be $4.8_{\mathrm{E}}12$ AuNRs/mL. For AuNR-2 the stock suspension was diluted 1:2 with DI water. For AuNR-4 the stock suspension was diluted 1:4 with DI water. Initial AuNR concentrations were calculated from the suspension UV-Vis absorbance spectrum (See SI for further details).

## 4.3 Results and Discussion

### 4.3.1 Particle Instability Parameter

To derive the PIP, we systematically studied how changes in peak height, peak wavelength, spectral skewness, spectral shape, and derivatives of spectra described the stabil-

ity of AuNRs in suspension (see SI). Although all parameters can be used as a measure of particle instability and aggregation, our study showed that by observing changes both in peak intensity and location (*e.g.* wavelength shift), the colloidal stability of a AuNR system could be accurately assessed. Furthermore, we developed a parameter that monitors the actual peak position and intensity, essentially tracking spectral profile evolution. The PIP requires two UV-Vis absorbance spectra: a reference spectrum of the nanoparticles and the data spectrum of the nanoparticles with the analyte of interest. Note that this is unlike both the FP[209] and AI[175] which are fundamentally based on averaged changes in a spectral profile within a specific wavelength range.

To define the PIP, we begin with a weighted intensity value ($I^*$) as Eq. 4.1:

$$I^* = \frac{\Delta I}{I_o} = \frac{I_o - I_n}{I_o} \tag{4.1}$$

where $I^*$ relates a change in peak intensity, $\Delta I$, to the reference peak intensity, $I_o$ at $n$ point in time.

The weighted wavelength shift is defined as Eq. 4.2.

$$\lambda^* = C\Delta\lambda = C(\lambda_o - \lambda_n) \tag{4.2}$$

where $\lambda_o$ is the reference peak wavelength position, $\lambda_n$ is the peak position at $n$ point in time, and $C$ is a weighting

function defined as Eq. 4.3:

$$C = \frac{I^*_{thresh}}{\Delta\lambda^*_{thresh}} \tag{4.3}$$

This normalizes the two parameters and eliminates the bias from an unequal parameter weighting. Typically, the distinction between a stable or unstable colloid system has been either a binary determination [206] or a qualitative assessment based on peak

changes [209, 175]. Our parameter, however, allows us to assign a number to the spectra which enables the quantitative comparison of different spectra using the PIP. Furthermore, we define that a suspension is stable when the measured absorbance spectra is less than 10% of an initial reference peak. This cutoff number is derived from both the literature[175, 173] and the assessment of over 600 experimental data points (See SI for additional details). Thus, we define $I^*_{\text{thresh}}$ as 0.1 and $\Delta\lambda^*_{\text{thresh}}$ as 10 such that an unstable system is defined by a 10% change in intensity or a wavelength shift of 10 nm.

Thus, the PIP is defined as Eq. 4.4:

$$\text{PIP} = \sqrt{(I^*)^2 + (\lambda^*)^2} \tag{4.4}$$

We note that by using a reference spectrum, the PIP is a concentration independent measurement as long as the reference and data suspensions are held at the same initial concentration. As a consequence, the PIP can capture changes in fundamental spectral structure such as the disappearance or emergence of peaks not present in a control sample.

To verify the performance of the PIP, we compared our index to the recently proposed AI. Figure 4.1 shows the PIP versus the AI for a theoretical data set of metallic nanorods with a lSPR peak at 700 nm. We created the set of data to mimic AuNRs aggregating over time such that each Gaussian represents the AuNR absorption spectrum from 600 to 800 nm at a particular instance in time with later times representing decreasing peak height. The AI as defined[175, 181, 202] divides the area under the lSPR peak by the measured peak intensity to maintain concentration independence; however, changes primarily in peak height over time can result in a constant AI, which incorrectly suggests a stable suspension. Practically, this can be realized when nanoparticles precipitate out of suspension without a change in size, shape, or inter-particle spacing, an inherently unstable response. Furthermore, the actual value of AI, much like FP, is an

arbitrary determination of stability and must therefore be compared to either a stable or unstable suspension to provide meaning.

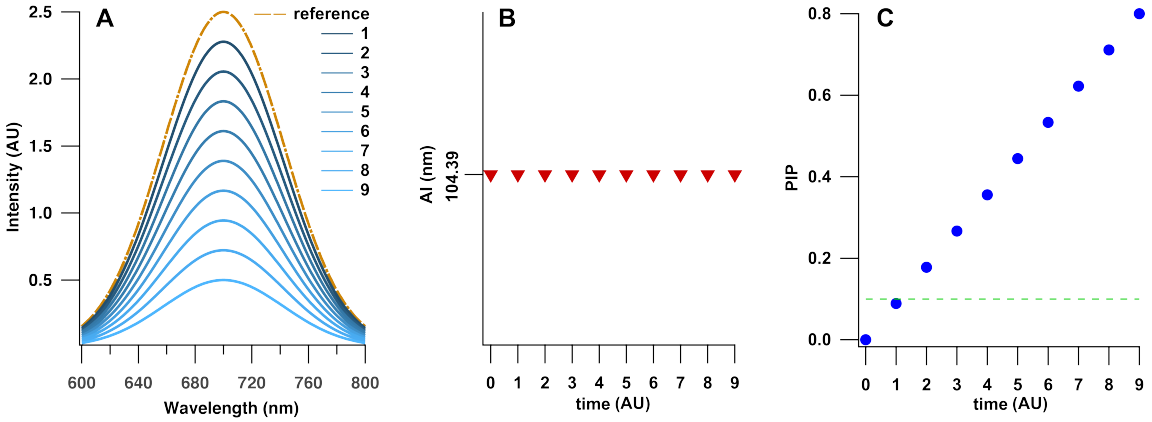


Figure 4.1: Performance of PIP to AI using a simulated data set of aggregating AuNRs. The spectra shown in (A) was computationally fabricated to simulate the aggregation of AuNRs over time as one would observe using UV-Vis absorbance spectroscopy over 24 h. In this case, we created the data to simulate AuNRs with a lSPR peak at 700 nm aggregating and thus decreasing in peak intensity without a wavelength shift. (B) shows AI[175], defined as the normalized area between 600 nm and 800 nm, vs. time directly corresponding to the simulated spectra in (A). Note that the AI shows no difference over time. (C) PIP vs. time for the simulated spectra in (A). Here, we note that PIP captures the change (or AuNR aggregation) of the data set as it is based upon a weighted combination of change in peak intensity and peak wavelength shift from an established reference spectrum (control).

Figure 4.1 shows we can capture instability in this particular case study since changes in the suspension are compared to a reference spectrum. Furthermore, PIP is quantitative on an absolute scale due to our 10% cutoff value. Although comprehensively studying stability over different factors, many studies[176, 179, 182, 195, 196, 185, 184, 175, 177, 193, 197, 190, 192, 178, 191] may not accurately give an assessment of stability because there is only one data point at one particular point in time which may falsely indicate stability (see Figure 4.1). However, one possible false negative to our method could be if the peak position changes as a result of the refractive index change. Although changes in refractive index can indicate the binding of an analyte to a NP surface, the addition of salt or other additive to a NP suspension could change the refractive index of the

suspension as compared to a reference spectrum.

To verify the accuracy of our method for assessing colloidal stability, we compared characterization of AuNR stability using both Dynamic Light Scattering (DLS), a more prevalently utilized technique in literature[120], and our method outlined above. DLS calculates NP size by measuring the radius of particles or aggregates in suspension through light scattering techniques[216]. We examined AuNR stability in a salt solution (NaCl in de-ionized (DI) water) at five different concentrations (1 mM, 10 mM, 100 mM, 500 mM, 1 M) with data shown in Figure 4.2. The AuNRs in different concentrations of salt were monitored over 15 min at 1 min intervals. As literature has shown, free-CTAB in solution can strongly affect AuNR stability[177]. To account for this influence, two different suspensions of AuNRs were used: (1) a purified suspension that was twice-centrifuged and (2) a suspension where the AuNRs were resuspended in 1 mM CTAB solution to establish a known free-CTAB concentration. Finally, control measurements were recorded using both DLS and PIP to serve as reference measurements for the free-CTAB comparison study. Based on DLS measurements the average NP hydrodynamic radius for the AuNR suspensions (in water) with and without added CTAB was calculated to be 7.5 nm and 10.1 nm, respectively. This difference is the result of the DLS fitting model in which the additional CTAB increases the average radius (See SI). In general, as salt concentration increases, measured radius increases. This trend is more observable for the twice-centrifuged samples, where the same conditions were measured with UV-Vis spectroscopy. We observe that all salt concentrations for the twice-centrifuged AuNR samples are above the stability threshold established by PIP. This is in contrast to the added CTAB suspensions where both 1 mM and 10 mM salt concentrations are identified as stable while 100 mM, 500 mM, and 1 M salt solutions are unstable.

We note that both characterization techniques identify the twice-centrifuged samples in all cases to be unstable from these data. We observe a similar trend for AuNRs

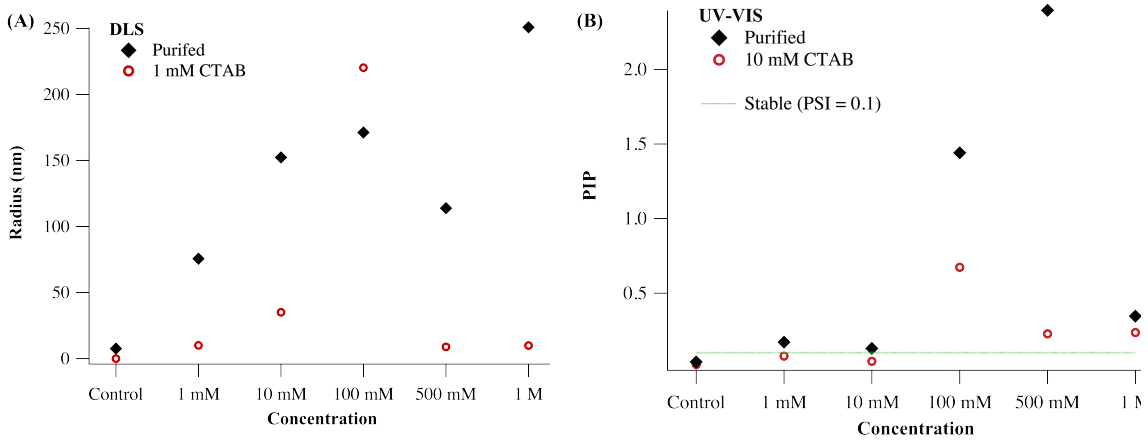


Figure 4.2: AuNR stability in pure salt (NaCl) at five different concentrations (1 mM, 10 mM, 100 mM, 500 mM, 1 M) after 15 min. AuNRs were suspended in either twice-centrifuged (purified) DI water or 1 mM CTAB solution and characterized by both (A) DLS and (B) UV-Vis spectroscopy over a continuously monitored 15 min time interval. DLS measurements showed that for the purified AuNR suspension the hydrodynamic radius progressively increased in average size with increasing salt concentration. For the 1 mM CTAB solution, the hydrodynamic radius significantly increased as compared to the control only for the 10 mM and 100 mM salt concentrations. UV-Vis spectroscopy measurements revealed similar trends with the purified solution being unstable (PIP $>$ 0.1). The 1 mM CTAB solution was stable at 1 mM and 10 mM and unstable for 100 mM, 500 mM, and 1 M salt concentrations. All AuNR solutions (both purified and 1 mM CTAB) had the same AuNR nanoparticle concentrations (Additional discussion regarding the DLS measurements is found in the SI).

suspended in 1 mM CTAB for both measurement techniques. Although not in full agreement, differences between the two measurements can be attributed to each technique's method of measurement. For the DLS measurements, increases in the hydrodynamic radius could be attributed to one of several factors: the formation of several large, but stable, aggregates; changes to the NP inter-particle spacing (but not unstable); and/or the formation of large, unstable aggregates. In the absence of an alternative analytical technique, only inferences to the causes of the changes in the derived hydrodynamic radius may be made from DLS measurements.[61] Conversely, as PIP is a reference-based measuremen (t, spectral changes recorded by the UV-Vis spectrophotometer can provide greater detail for understanding the aggregation behavior of the colloidal system. For

example, large changes in the spectra directly correlate to changes in NP morphology as a result of aggregation and therefore appear as a large increase in PIP. An intensity decrease without spectral profile change indicates a change in NP concentration, not necessarily the result of aggregation (*e.g.* sedimentation), which would change PIP slightly. As a consequence of using the physical NP properties, PIP could indicate that such a colloidal suspension is in fact stable in contrast to DLS measurements of the same suspension. Therefore, we believe UV-Vis spectroscopy still to be the best form of stability characterization.

To both experimentally verify our stability parameter and increase understanding of AuNR stability in response to different environments, we examined over 600 spectra of AuNRs in response to different salts (NaCl, NaBr), salt concentration, pH, and buffer type as well as AuNR concentration. These conditions were selected both for their broad importance in nanoparticle processing and to understand nanoparticle stability in biological / physiologically relevant conditions. A summary of our data using PIP is shown in Figures 4.3 and 4.4. Note, these were also visually compared to UV-Vis spectra to confirm that PIP is an accurate measure of stability (See SI).

Figure 4.3 shows the stability response of AuNRs to different salt and buffer concentrations at both 2 h and 24 h. Black indicates stable, where red indicates unstable. In general, as salt concentration increases, AuNRs become increasingly unstable. For a commonly utilized salt (NaCl), the AuNRs are unstable through the full range of concentrations studied (1 mM to 1 M) and the degree of instability increases with increasing salt concentration. However, for different ionic species (NaBr), AuNRs are stable at both 1 mM and 10 mM and are unstable above 100 mM. For HEPES, we observe that the AuNRs are unstable regardless of buffer concentration after 24 h, whereas using Tris buffer, AuNRs are stable regardless of buffer concentration. For borate buffer, we observe that at low concentrations, the AuNRs are unstable (1 mM) after 24 h but at concen-

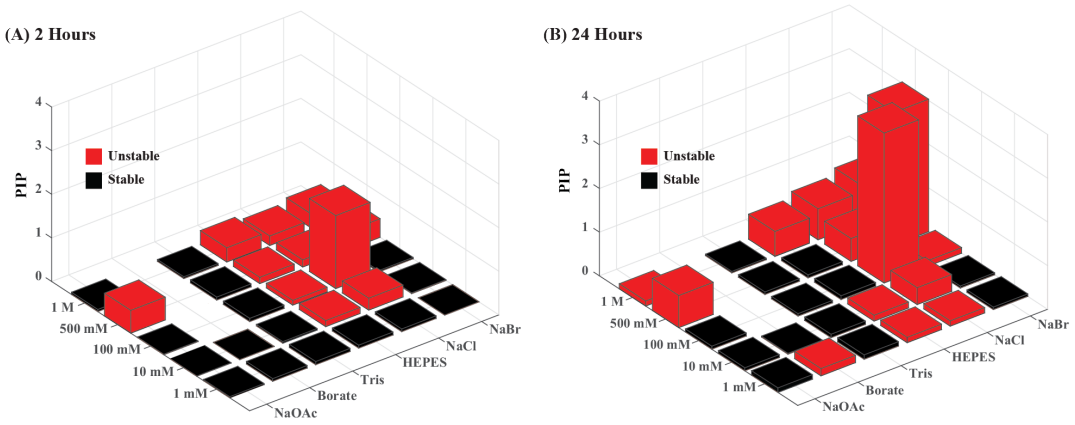


Figure 4.3: Stability bar graph of AuNRs in response to different salts (sodium acetate-NaOAc, borate, Tris, HEPES, sodium chloride-NaCl, and sodium bromide-NaBr) and different concentrations (1 mM, 10 mM, 50 mM, 100 mM, 500 mM, and 1 M) at 2 h (A) and 24 h (B) intervals. This chart shows the parameter space as a function of PIP with unstable values (PIP>0.1) indicated as red. A suspension of twice-centrifuged AuNRs served as the starting suspension for all measurements and we performed each measurement in triplicate. We observe that AuNRs suspended in Tris were stable across all concentrations examined, while NaCl was unstable across all concentrations after 24 h. NaBr and NaOAc became unstable at higher salt concentrations and borate buffer was unstable after 24 h, but not at 2 h. Absence of data for borate buffer above 100 mM is due to the insolubility of sodium tetraborate in water at these concentrations. An expanded figure with borate buffer stability data at 50 mM is available in SI.

trations up to buffer saturation (above 100 mM), the AuNRs are increasingly stable. Finally, we observe with sodium acetate (NaOAc), AuNRs are stable between 10 mM and 100 mM but unstable outside of that range. With regard to time, in general, 2 h is a good indication of stability; however, we notice, for the 1 mM electrolyte concentration case, waiting 24 h does make the system go from stable to unstable in some buffers and salts.

In addition, we examined the effect of solution pH, as shown in Figure 4.4. Our data shows that AuNRs are stable through a wide range of pH values with instability occurring only at pH 13. Since the stability at 24 h was the same as that at 2 h (with PIP only increasing in an already unstable system) we show only the values at 24 h for brevity.

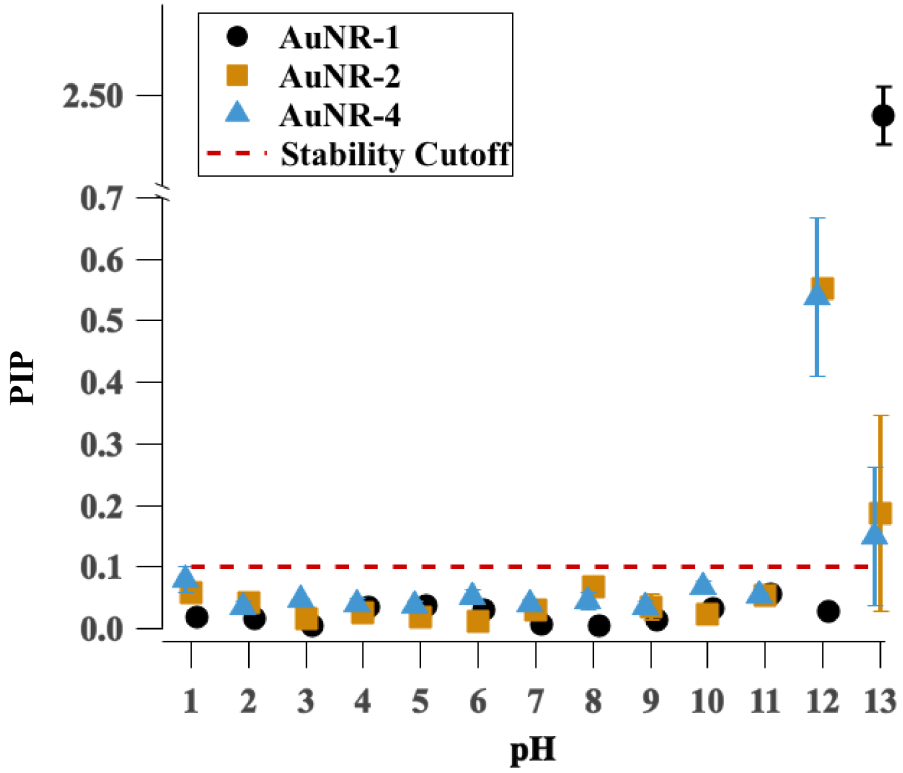


Figure 4.4: Stability response of AuNRs as a function of solution pH and AuNR concentration. AuNR-1 is the initial AuNR suspension with AuNR-2 and AuNR-4 consisting of a 1:2 and 1:4 dilution (respectively) with DI water. Our data shows that AuNRs are stable through a wide range of pH values with instability occurring only at pH 13. Since the stability at 24 h was the same as that at 2 h (with PIP only increasing in an already unstable system) we show only the values at 24 h for brevity.

With both the salt studies and pH sweep, we examined what effect AuNR concentration had on their colloidal stability. Figure 4.5 shows PIP values of AuNR concentrations diluted by a factor of 2 (AuNR-2) and 4 (AuNR-4) for our salt and buffer sweep. We observe that below 10 mM concentration decreasing AuNR concentration decreases stability except in HEPES and Tris buffer. We also observe suspensions become unstable as AuNR concentration decreases with AuNR-2 and AuNR-4 being more unstable; however, suspensions are generally not affected by pH with the only exception being at high pH

values (12 and 13).

### 4.3.2 Comparison with to studies in literature

One major motivation for developing PIP is for the facile and quantitative comparison of results from different colloidal stability studies. Study comparisons are inherently difficult due to differences in measurement states (*in-situ* [61] vs *ex-situ* [197]) or techniques[204, 205, 206]. Regardless, there have been approximately 30 different studies on AuNR colloidal stability in response to changes in purification methods, pH, salt, buffer, physiological media, and temperature. Systematic studies have focused on solution ionic strength (salt) not only because of physiological applications (Normal Saline NaCl concentration is 150 mM)[217], but also because of functionalization of AuNRs with various surface coatings[184]. Although most studies have focused on NaCl [195, 179, 199, 200, 181, 176], Nikoobakht *et al.*[197] examined the influence of ion size (NaCl, NaBr, NaI, and NaOH). Many researchers have systematically studied the effect of pH using UV-Vis[196, 191, 192, 193, 194, 195, 181] and found no change or degradation below a pH value of 7. Others[183, 181] explored differences in response between synthesized and functionalized AuNRs. However, there are few studies on the effect of AuNR concentration. Therefore, in this section, using these studies, our data, and PIP, we discuss the importance of sample preparation and purification in measuring nanoparticle stability, demonstrate the importance of experimental methodology, compare different pH, salt concentration, and buffer types, and provide an overview of other considerations influencing AuNR stability.

Throughout literature AuNR stability has been shown to be sensitive to both synthesis conditions and purification methods[178, 218]. The most widely used AuNR synthesis method is the bottom-up seed mediated approach developed by the Murphy[214] and

El-Sayed[215] groups. Although an established method, slight differences in reagents, environmental conditions (temperature), or laboratory techniques during synthesis would change the resulting AuNR surface coating, shape, and concentration thereby influencing the AuNR colloidal stability[208, 218]. John *et al.* [218] optimized the method through a systematic study of variable synthesis parameters. We use the seed-mediated approach as recommended for synthesis of the AuNRs used in this work (see Methods).

After synthesis, AuNRs must be purified from the growth solution. Multiple studies have already examined the effect that purification methods (primarily centrifugation) have on AuNR colloidal stability with respect to different parameters (centrifugation speed[180], number of washes[181, 182]), and removal of free surfactant (CTAB) in solution[176, 177, 178, 179, 182]. Universally, these studies conclude that careful selection of an appropriate purification method is critical to maintaining AuNR stability as excessive centrifugation causes both aggregation[178] and morphological changes[219] due, in part, to the removal of CTAB from solution. Indeed, as shown in Figure 4.2, AuNR colloidal stability increases with an increasing amount of free-CTAB in solution that remains after centrifugation. Several groups [177, 178, 182] have examined the importance of the equilibrium between the free-CTAB in solution and that bound on the AuNR surface in maintaining AuNR colloidal stability. Similar to Figure 4.2, other work has shown that the excess removal of free-CTAB from solution leads to AuNR aggregation. In order to maintain equilibrium, CTAB desorbs from the AuNR surface thereby causing defects in the AuNR surface coating which induce aggregation. Through an extensive systematic study, Ferhan *et al.*[179] conclude that, although centrifugation may cause defects to appear in CTAB surface coatings, two centrifugation washes is optimal to extract the AuNRs from the growth solution and to remove excess free surfactant (CTAB) without inducing AuNR aggregation[182]. Although twice purified AuNRs exhibited increased instability in our initial experiments (Figure 4.2), we remained consistent with literature

for our systematic study with each sample consisting of twice-centrifuged AuNRs and the amount of free-CTAB held constant.

After purification, AuNR preparation for subsequent use requires a solvent exchange (mixing) with a biological buffer or different solution. However, as part of developing a standardized method for assessing nanoparticle colloidal stability, we observed that the exchange method after purification can greatly influence AuNR stability. As many AuNR stability papers lack specifically outlined exchange methods, variations in technique may contribute to observed colloidal behavior and thus inter-study differences. The results of our study are included in the SI. Based upon our results, all AuNR suspensions were mixed *via* vortex mixing to ensure well-mixing before analysis.

One aspect of the utility of the PIP is the ability to easily and directly compare different data sets. Figure 4.6 compares two UV-Vis data sets from literature that investigate aggregation in the presence of salt [220, 194] with our data sets taken at 2 h and 24 h. Studies from literature show AuNR instability between 10 mM and 100 mM NaCl; AuNRs are stable outside this range. Our data shows similar results but only at 2 h after analyte addition (blue upright triangle). However, we observe increased instability at different concentrations after 24 h (yellow diamond). We attribute the differences in stability at low and high salt concentrations to two possible phenomena. (1) At low concentrations, the electric double layers (EDL) surrounding the AuNRs are thick, offering enhanced electrostatic repulsion and thus colloidal stability. (2) At higher concentrations an equilibrium between the CTAB in the free solution with that on the AuNR surface. As discussed in literature[221], CTAB is not covalently bound to the AuNRs but rather coordinates and thus may dissociate from the AuNR surface to reach an equilibrium with the solvent. At high AuNR concentrations, there is an abundance of AuNRs and surrounding CTAB and thus less CTAB dissociates from the AuNR surface, effectively limiting numbers of surface coating defects for the salt to induce irreversible aggregation.

Finally, these data comparisons suggest that the UV-Vis studies from literature used AuNR / salt suspensions that had not reached equilibrium. They also suggest that if one only observes the AuNRs shortly after addition of salt, the resulting value is only a measure of short term AuNR stability while extended incubation (*e.g.* 24 h) may result in aggregation.

In addition to the influence of salt, the effect of suspension pH on the stability of CTAB-coated AuNRs has been systematically studied by several groups [196, 191, 192, 193, 194, 195, 181]. Broadly, these studies monitor AuNRs for aggregation using UV-Vis spectroscopy and find that AuNRs in suspension experience no change or degradation below a pH value of 7 [176, 192, 181]. Above this value, AuNRs are observed to irreversibly aggregate [194, 196]. However, some groups observed different AuNR behavior at different pH values such as reversible changes in absorbance. For example, Kozlovskaya *et al.*[193] failed to observe AuNR aggregation but did observe a reversible change in the shape of the AuNR lSPR peak width in response to solution pH values. Specifically they observe that the lSPR peak width narrows when AuNRs are at low pH (pH 3) while broadening at higher pH values (pH 8). Tiwari *et al.*[191] observed similar behavior with changes in the peak LSPR spectra above pH 8 that is especially pronounced for longer aspect ratio AuNRs. While this does not establish the suspension as unstable, it does indicate that the suspensions change in response to pH. Although many studies found CTAB-coated AuNRs to be unstable at higher pH values, some research such as that by Zhan *et al.*[195] found inverted trends where AuNRs are stable above pH 6 / 7 but highly unstable below pH 5.5. The different AuNR responses to pH stem most likely from differences in sample purification methods, acid addition methods, or analytical technique.

Our data aligns well with the bulk of pH / AuNR studies; however, we observe no aggregation or structural change until a solution value of pH 12. We hypothesize that

this increased stability is the result of both the sample mixing method as well as the purification method employed. By systematically controlling the amount of free-CTAB in solution as well as ensuring that the sample is well-mixed using a vortex mixer without introducing nucleation points, the AuNR response to pH is primarily chemistry based. As synthesized AuNRs, before any functionalization, have a highly positive surface charge independent of pH [187, 188, 189, 192], aggregation observed in previous studies at lower pH values may be the result of surface coating defects rather than purely an AuNR response to pH.

Beyond salt concentration and pH, much literature has investigated the effect of buffered solutions for stability of surface functionalized AuNRs (*e.g.* ligand modified[221, 202]); however, there exist only a few systematic studies with unmodified, CTAB-only AuNRs. Nikoobakht[197] showed that unbuffered solutions containing only NaCl induced the best aggregation, consistent with our results (Figure 4.3). In general, we hypothesize that buffers are more stable than salt solutions (NaCl) because of the size of the buffer ion as well as the kind of buffer. For example, sodium tetraborate is known to stabilize gold suspensions[195], and thus our result of stable AuNR suspensions with increasing concentrations of borate is sound. Furthermore, all other buffer ions tested are larger than Cl-, which will allow for a larger ion cloud and a more stabilizing effect. For example, Tris is a large, soft ion, which promotes stability consistent with our data showing stable suspensions across all concentrations. Although this particular result is not consistent with literature (*e.g.* Knecht[176] examined the stability of unmodified, CTAB-only AuNRs in response to Tris and showed AuNR instability at Tris concentrations between 10 mM and 100 mM), this could easily be a result of a different concentration of free-CTAB in solution. HEPES was shown to be unstable at very high (1 M) and intermediate (10 mM) concentrations. Since this is a zwitterionic buffering molecule, the behavior at various concentrations is very complex and the HEPES molecule may have limited interaction

with the AuNRs. Finally, as seen in Figure 4.3, there is a general trend of instability as the buffer concentration increases. We attribute this behavior to the decrease of the EDL thickness and the charges not being screened as effectively, thus promoting aggregation.

Relatively few studies have explored the implications of AuNR concentration on colloidal stability[177]. Our results show that it is an important factor for stability. In general, more AuNRs in suspension tend to have higher colloidal stability. However, this is not true in low salt solutions (1 mM) where stability decreases with nanoparticle concentration. At higher concentrations of AuNRs in suspension, there is more CTAB bound on the surface and less in solution. As described by Hafner *et al.*,[177] the interplay of the equilibrium between these two species is important in maintaining colloidal stability. Assuming an unchanged equilibrium constant for the dissociation of CTAB from AuNRs, increasing the concentration of AuNRs in suspension will result in an increased concentration of CTAB in solution, effectively stabilizing the higher concentration AuNR samples. At lower concentrations of AuNRs, there is less CTAB bound to the surface of the AuNRs due to a greater quantity of CTAB dissociating from the surface to maintain equilibrium. This creates non-uniformities on the surface coating of the AuNRs which enables more particle-particle interactions. However, at very low salt concentrations, the EDL is thicker and thereby prevents AuNRs from attaching to each other and increase suspension stability at higher concentrations where the double layers may be overlapping, promoting adhesion.

Although not investigated by us, several groups have examined the stability of AuNRs in organic solvents[184], physiological buffers with proteins in solution [198, 181], artificial biological fluids [186], and cell culture media [202] and all conclude from their measurements that without changing the amphiphilic ligand surface coating on AuNRs (CTAB), the AuNRs generally aggregate when suspended in the aforementioned solutions. Other groups have examined stability in response to temperature at both physiological condi-

tions (37 °C and below) [181] and at very high temperatures (up to 250 °C) [201] and find both aggregation and morphological changes in AuNRs under different temperature regimes. Specifically, at temperatures above 40 °C, AuNRs were found to lose their anisotropy, transitioning into a more energetically favorable spherical shape. Although important for the use of AuNRs in a physiological application, such morphology changes greatly influence the plasmonic response of the AuNRs.

## 4.4 Conclusion

In summary, the LSPR spectral response of AuNRs has been used for the quantitative characterization of colloidal instability through the derived Particle Instability Parameter. For the test case of AuNR instability due to various concentrations of NaCl, the PIP was found to fully capture the onset of colloidal instability as compared to other characterization methods. The PIP was used to evaluate the stability of AuNRs in response to several parameters: salt, pH, and buffer concentration. Both salt concentration and buffer type were found to initiate colloidal instability in CTAB-coated AuNR suspensions whereas solution pH was found to have little effect. We studied the influence of both the amount of free-CTAB in solution and nanoparticle concentration on the measured colloidal instability. Free-CTAB in solution and nanoparticle concentration were shown to have a strong effect on stability, with high CTAB concentration and low nanoparticle concentration tending to lead to solution instability. Although in many cases, our results showed similar trends as literature, there were unique difference, most likely due to uncertainty in sample preparation and handling. These findings demonstrate the critical need for a standardized method of assessing nanoparticle colloidal instability. The PIP offers a quantitative, robust method for characterizing colloidal instability for both AuNRs and plasmonic nanoparticles as a whole.

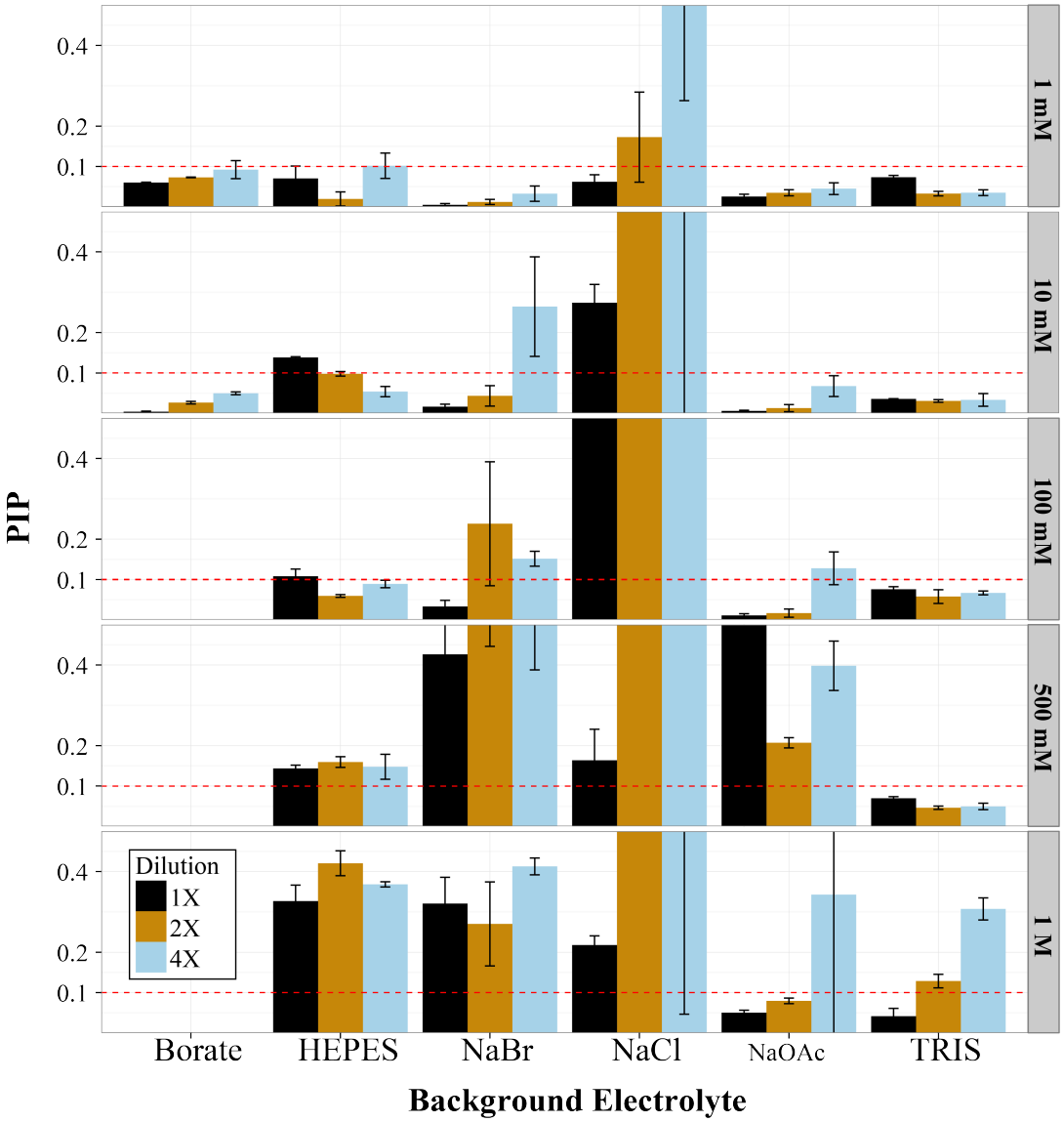


Figure 4.5: Bar graph comparing colloidal stability of AuNRs in response to different salts (borate, HEPES, sodium bromide-NaBr, sodium chloride-NaCl, sodium acetate–NaOAc, and Tris) and AuNR concentration (1X, 2X, and 4X dilutions) at each salt concentration (1 mM, 10 mM, 100 mM, 500 mM, and 1 M) at 2 h. AuNR suspensions were prepared so the final analyzed AuNR concentrations were constant between salt solutions with the initial (1X) suspension serially diluted to make 2-fold (2X) and 4-fold (4X) diluted suspensions. Generally the borate, NaBr, NaCl, and NaOAc salt solutions exhibited increased instability as AuNR concentration decreased across all salt concentrations. Exceptions include 100 mM and 1 M NaBr as well as 500 mM NaOAc. AuNR concentration only slightly influenced the AuNR suspension colloidal stability in response to HEPES and Tris across the salt concentration range studied. NaCl exhibited the most AuNR concentration dependent instability across the entire salt concentration range. Measurements were performed in triplicate. To maintain consistent relative scale, the plots are truncated at PIP = 0.5. Full plot is available in SI.

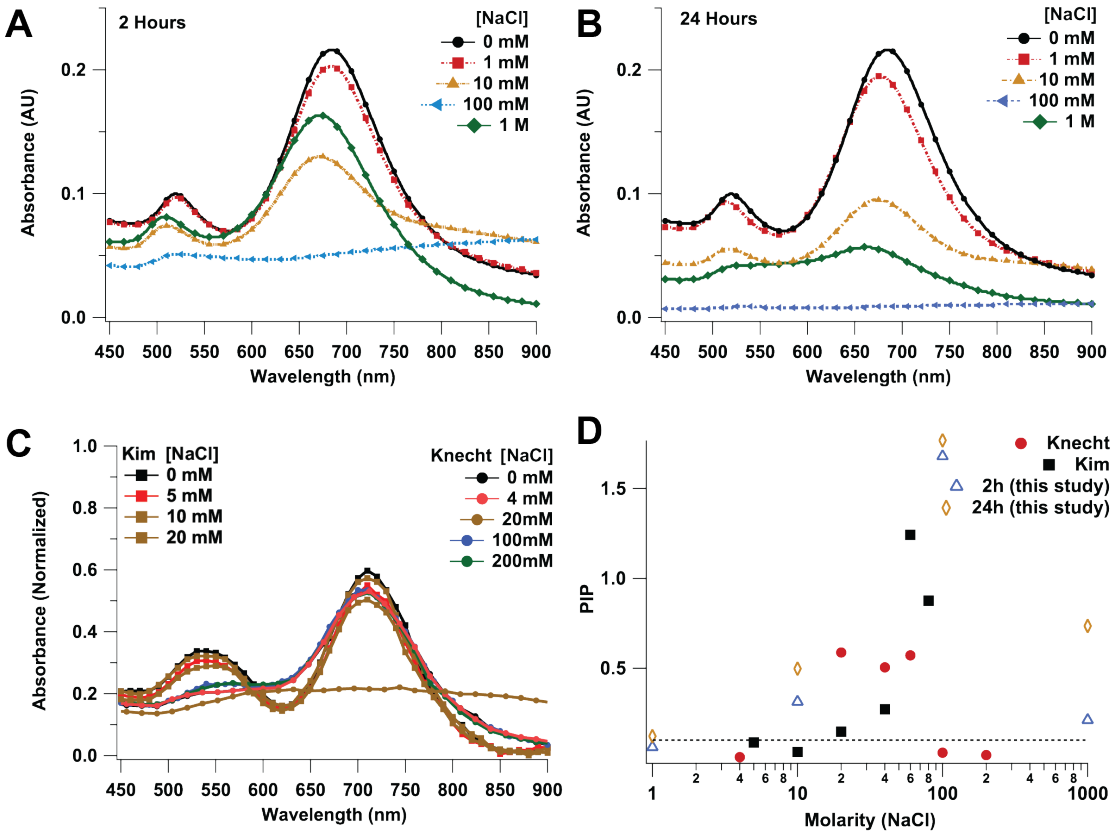


Figure 4.6: Comparison of our data set taken at 2 h (A) and 24 h (B) with two UV-Vis data sets from the literature that investigate aggregation in the presence of salt (Kim[179] and Knecht[194]) (C). The suspensions in Knecht were measured immediately after the introduction of salt while the suspensions in Kim were measured after 10 min. The spectral data at 2 h (A) is similar to literature (C) but after 24 h increased AuNR instability is observed through spectral changes (B). (D) shows the PIP values of all the data shown in (A), (B) and (C). When compared using PIP, data suggests that the UV-Vis studies from literature may have not reached equilibrium. It also suggests that if one only observes the AuNRs shortly after addition of salt, the resulting value is only a measure of short term AuNR stability while extended incubation (*e.g.* 24 h) may promote aggregation.

# Chapter 5

# Towards bio-analytical applications of gold nanoparticles

## 5.1 Motivation

The virulent pathogenic bacterium, Streptococcus pneumoniae, is a leading cause of pathogenic diseases and is responsible for a large variety of ailments including pneumonia, meningitis, sepsis, otitis media, endocarditis and more, occurring commonly in young children and the elderly[222]. At present, diagnosis is made by a variety of methods and a conclusive diagnosis requires a time scale of 24–48 hours[223]. These tests require the growing of bacteria cultures with an incubation time that requires a longer timescale[224]. Depending on the severity and the invasiveness of the disease, immediate diagnosis is crucial for early and effective treatment.

The ability to detect and characterize biological targets of interest accurately and with high sensitivity is vitally important to a wide array of fields ranging from drug discovery and health diagnostics to threat detection and bio-material development. Microfluidic lab–on–a–chip devices have demonstrated considerable promise toward this goal. Re-

search developments have continued to yield improvements, not only in analysis time, sensitivity, and specificity, but also in providing a better fundamental understanding of biological interactions. Despite these advances, however, current microfluidic technology suffers from at least two distinct limitations: It is currently difficult to resolve the presence of similar analytes in an electrophoretic separation, and lab–on–a–chip analytical systems generally require bulky and expensive off–chip detection methods that preclude the development of cost–effective and portable analytical systems.

One approach to addressing this issue would be using a metallic nanoparticle platform for rapidly and cost-effectively identify bacterial causes of early stage sepsis in patients in whole blood. Using this method the platform could directly image bacteria bound to antibody-conjugated gold nanorods with finely tuned absorbance spectra exhibiting near-infrared localized surface plasmon resonance peaks at wavelengths of light where blood is transparent with either an IR camera or a spectrophotometer. This innovation will allow not only for early stage detection of sepsis, but allow for the detection in undiluted whole blood, as well as novel studies revolving around the fractions of bacteria that remain in the blood but cannot otherwise be detected.

An important extension of the work presented here is the development of a novel microfluidic-based analytical technique for the rapid detection and analysis of pathogenic bacteria in whole blood. This technique combines the speed, low sample volume, and integration of lab-on-chip microfluidic analysis with the unique optical properties of surface-functionalized gold nanorods into a high-sensitivity biosensing platform. We postulate that by introducing gold nanorods functionalized with S. pneumonia antibodies into a septic whole-blood sample, the nanorods will preferentially bind and thereby tag both whole and partial S. pneumonia bacteria. Gold nanorods exhibit unique size-dependent localized surface plasmon resonance with tunable absorption peaks in the visible and near-infrared (NIR) spectra. Utilizing nanorods with absorption peaks within the NIR

transmission window of biological fluids enables the detection of nanorod-tagged bacteria in whole blood through absorption spectroscopy. This technique flows the nanorod/whole blood sample through a microfluidic capillary chip and monitors the absorption spectra in real time using a fiber-coupled spectrophotometer to rapidly analyze the entire sample thereby monitoring the presence of and quantifying the concentration of S. pneumonia. The preliminary results demonstrate both the absence of non-specific binding of the nanorods and the ability to clearly detect gold nanorods with NIR absorption peaks in undiluted whole blood. If proved successful, this technique is not limited to S. pneumonia, but can be further extended to perform the simultaneous analyses of multiple strains of pathogenic bacteria by monitoring the absorption spectra of multiple nanorod sizes, each having been functionalized to a specific bacterial target.

## 5.2 Experimental Methods

All nanorods used in this work were synthesized via the previously described seed-mediated approach unless otherwise described.

### 5.2.1 UV-Vis Absorbance Spectroscopy

1 mL of NS20(860) nanorods were purified and resuspended in 1 mL of undiluted mouse whole blood (Bioreclaimation, Inc). Dilution measurements were with 1X Phosphate Buffered Saline (PBS, Fisher Scientific).

### 5.2.2 Streptococcus pneumoniae detection

NHS functionalized gold nanorods (NR20(860), Nanopartz, Inc.) were functionalized with Streptococcus pneumoniae Monoclonal antibody (Pierce, MA1-10835) by incubating

the nanorods with the antibody for 1 h. Functionalized nanorod samples divided into 500 $\mu$L alloquots. Mouse blood infected with Streptococcus pneumoniae isolate D39 was obtained from the Marth lab at UCSB[225]. For both the infected and control samples, 1 nanorod alloquot is purified via centrifugation (3 m, 14000 RCF), and nanorods are resuspended in 1 mL of blood. Samples are incubated for 15 m before analysis. 50 $\mu$L of sample is pipetted onto a clean glass microscope slide with cover slip. A Nikon Eclipse L-150 upright microscope with halogen illumination is used for sample analysis.

### 5.2.3 Resonant Light Scattering Detection

All work was performed using an Olympus BX41 Upright Microscope. Glancing, scattering illumination was provided by four different laser diodes (Thorlabs) with collimating, free-space optics with wavelengths of either 632 nm, 658 nm, 690 nm, and 785 nm. Each laser beam was directed onto the microfluidic chip at a glancing angle of 72° (from normal) with a spot size of 1 mm centered in the field of view of the microscope objective. Experiments were imaged using an Andor Luca EMCCD camera. Vacuum driven flow was provided through the use of hand-held syringes connected to the chip by 100 $\mu$m ID Tygon tubing.

### 5.2.4 Microchip Microspectrophotometry Analysis

Measurements recorded on a custom-fabricated system based upon an Olympus BX-41 upright microscope with attached spectrograph (Andor Shamrock 303i). Spectra recorded using a Newton (Andor) camera. A Luca EMCCD (Andor) camera is used to chip alignment verification. Illumination provided either via halogen lamp (BX-41 internal source) with custom Chroma flattening filter (for more uniform spectral profile) or mercury illuminator (U-HGLGPS, Olympus) with Chroma daylight filter. Spectrograph

measurements recorded using 0.005 s exposure, 10 accumulations per measurement, full vertical binning, and a diffraction grating with a 7500 blaze, 600 l/mm groove density. Vacuum driven flow was provided through the use of hand-held syringes connected to the chip by 100 $\mu$m ID Tygon tubing.

### 5.2.5 Device Fabrication

Three microfluidic test devices were fabricated to understand the detection efficacy at distinguishing between different populations of nanorods and to improve the sensitivity of detection non-fluorescently functionalized nanorods in solution using microchip capillary electrophoresis.

**Device 1: 3-Sheath Flow Device** A three-sheath flow device was developed to determine whether the gold nanorods could be detected and distinguished while flowing through a microfluidic channel. The device was a composite chip made from a silicon substrate with 5um of thermally grown silicon oxide, PDMS side-walls, and a sealing layer of fused-silica glass with fluidic vias.

**Device 2: Microchip Capillary Electrophoresis** A microfluidic capillary injection chip was developed to determine whether the gold nanorods could be injected and detected in a microfluidic channel. The device was a composite chip made from a silicon substrate with 5um of thermally grown silicon oxide, PDMS side-walls, and a sealing layer of fused-silica glass with fluidic vias.

Both devices were fabricated using a 200 $\mu$m thick sheet of precast polydimethylsiloxane (PDMS) to define the channel walls. The cut PDMS sheet was bonded via oxygen plasma to a silicon wafer with a 5 $\mu$m thermal oxide layer and a fused-silica wafer with drilled fluidic access ports.

Figure 5.1 shows the three different components of the sheath flow and microchip CE devices. The use of PDMS enabled the rapid prototyping of different microfluidic channel configurations.


Figure 5.1: A render of the three different components of the PDMS microfluidic devices. The pattern of the PDMS could easily be changed to enable the use of standard top and bottom substrates to enable rapid prototyping.

**Device 3: Microchip Microspectrophotometry Device** A fused silica microfluidic channel was fabricated via wet etching and direct bonding. Channel dimensions are 50 mm length, 50 $\mu$m width, and 20 $\mu$m depth. Port connectors (Labsmith) are bonded to drilled fluidic vias for interfacing.

## 5.3 Platform Validation

The LSPR spectrum of the gold nanorod sensors is tunable from visible wavelengths to the near-infrared. Both whole blood and water are transparent in the near infrared (NIR). By using gold nanorods with an LSPR peak wavelength in the NIR, changes in the measured LSPR spectrum will indicate the presence of target, not interference from the fluidic medium. Figure 5.2 shows the absorbance spectra for several different gold nanorod samples with an overlay of the biological transparency window[226].

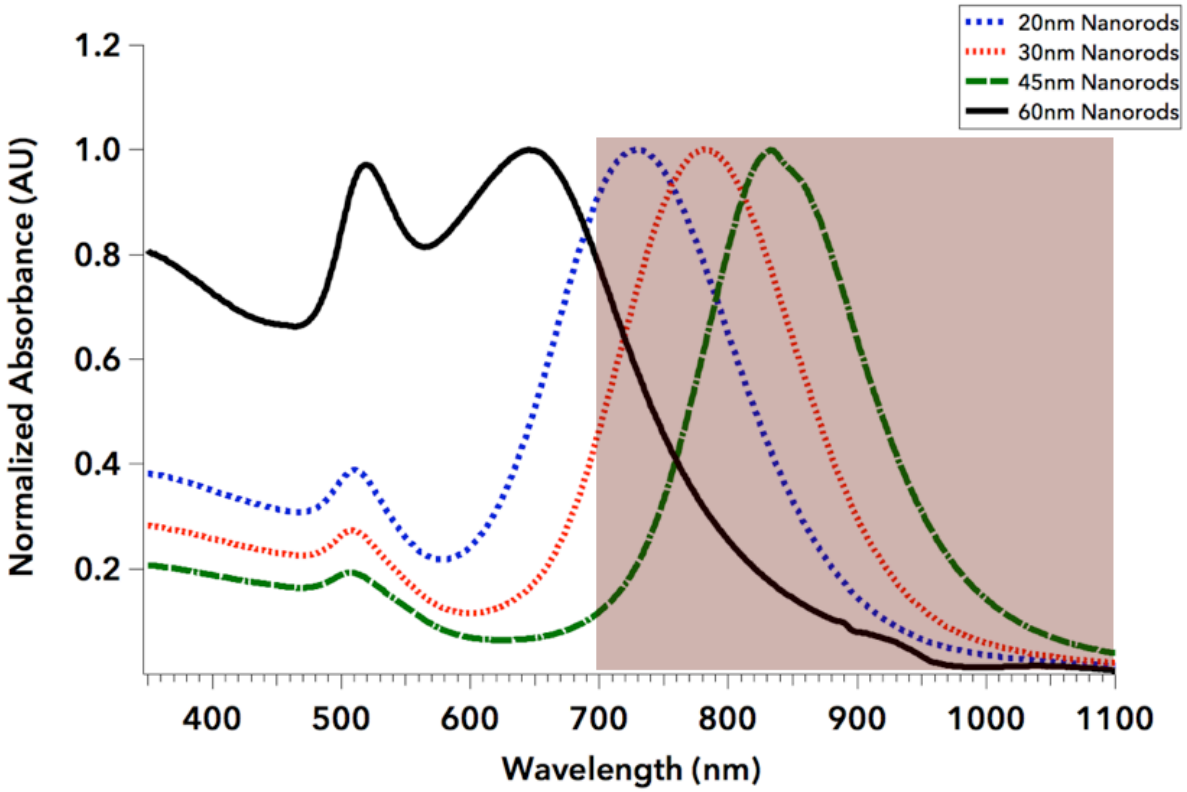


Figure 5.2: The absorbance spectra four different lab–synthesized gold nanorods showing the tunable nature of the absorbance peak. The shaded region of the chart is the blood transparency window[226]. The spectra were measured using a UV-Vis. The legend refers to the nanorod length.

Figure 5.3 shows the detection of NR20(860) nanorods in whole blood using UV-Vis spectroscopy. Although the LSPR peak blue shifts as compared to the peak measured in

DI water, it is clearly detected and only a moderate improvement in measured intensity is observed when the whole blood solution is further diluted with 1X PBS.

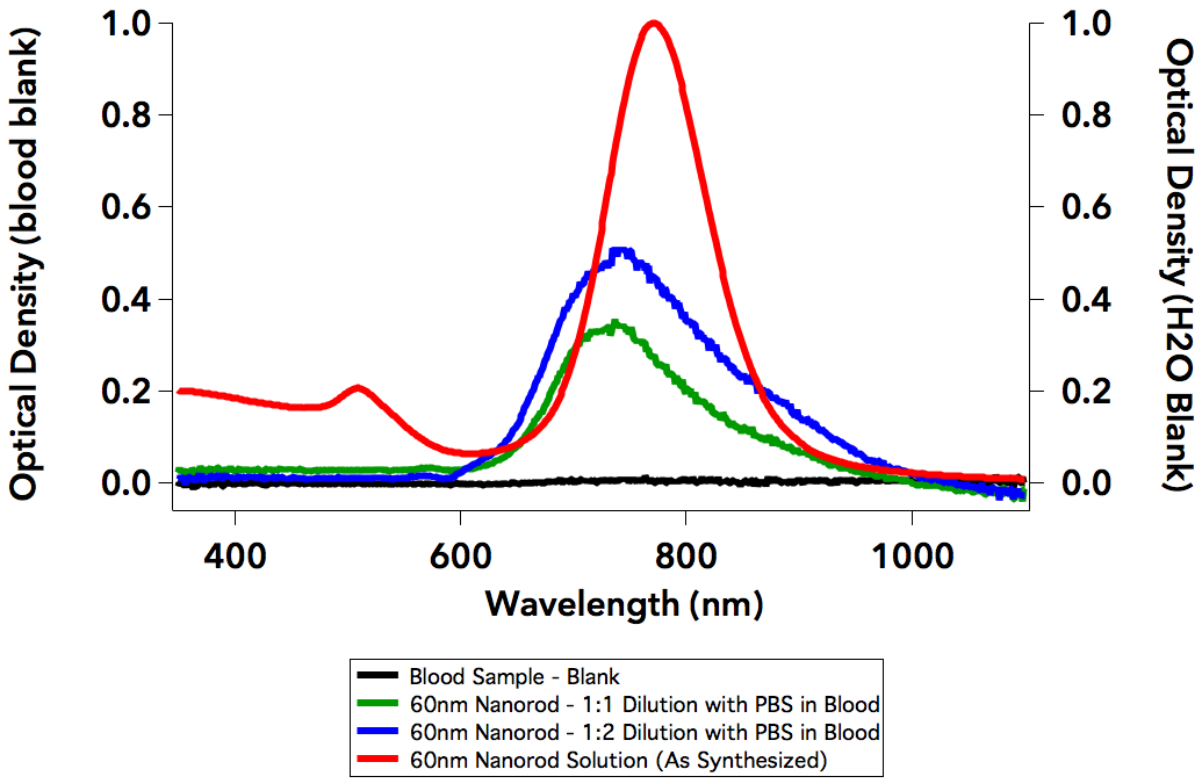


Figure 5.3: Absorbance spectra of NR20(860) nanorods in both DI water and diluted whole blood (1:1, 1:2 1X PBS). The NR20(860) sample is clearly observed in whole blood with only a moderate blue shift away from the absorbance peak measured without the presence of blood.

Darkfield microscopy is used to detect gold nanorods by observing the light scattered by the particles. To verify the ability to optically detect gold nanorods in whole blood, a series of control experiments were performed as summarized in Figure 5.4. Figure 5.4A shows a darkfield image of NS20(860) nanorods in solution without the presence of blood, Figure 5.4B shows a brightfield image of blood cells without the presence of nanorods, Figure 5.4C shows a darkfield image of the NS20(860) nanorod / blood mixture with the blood cells under flow, while Figure 5.4D shows a picture of the same mixture under

darkfield conditions under stationary conditions. The NS20(860) nanorods can be clearly observed in whole blood. The blood cells, while still detected in darkfield microscopy, do not impede the detection of the nanorods. The streaks in Figure 5.4B and C are from the movement of the blood cells during exposure as the solution as the solution is under flow as compared to the stationary conditions of Figure 5.4D. The stationary blood cells in Figure 5.4B are blood cells that have stuck to the substrate surface.

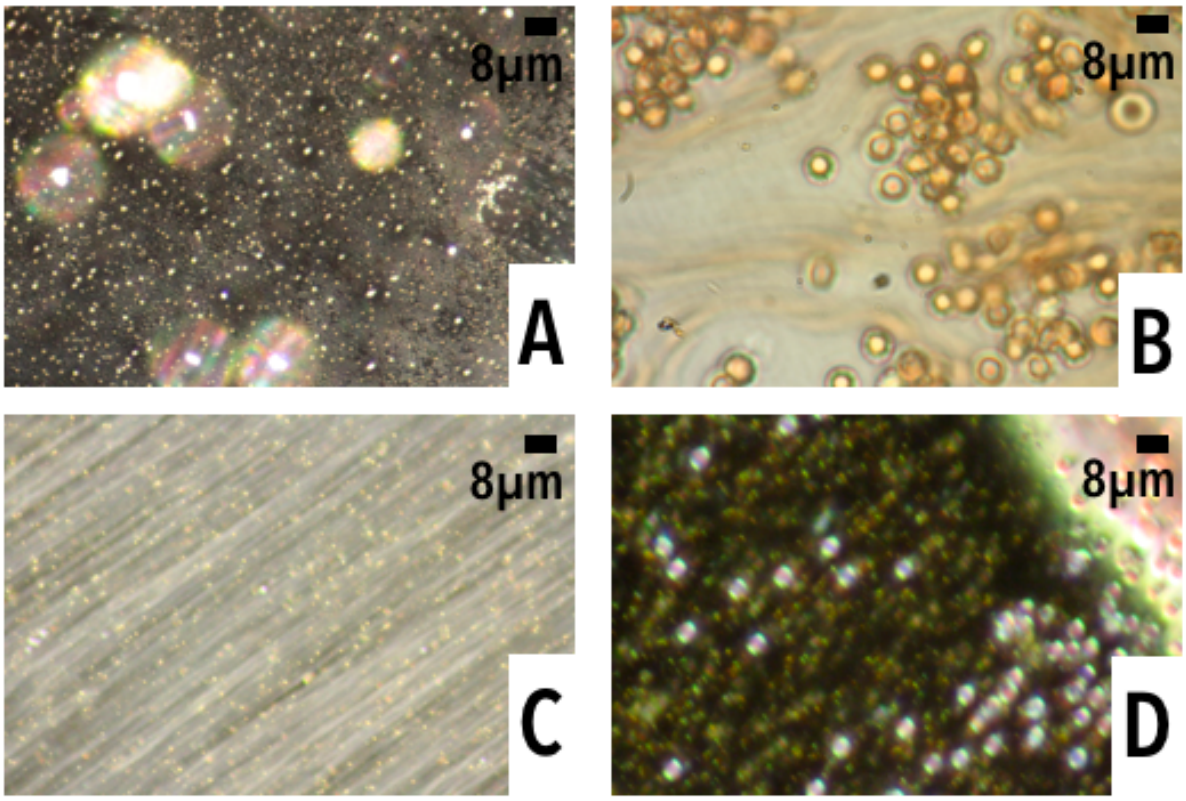


Figure 5.4: (A) Shows a darkfield image of NS20(860) nanorods in solution without the presence of blood. (B) Shows a brightfield image of blood cells without the presence of nanorods. (C) Shows a darkfield image of the NS20(860) nanorod / blood mixture with the blood cells moving. (D) Shows a picture of the mixture under darkfield conditions with the blood cells stationary. These images show that the NS20(860) nanorods can be clearly observed in the presence of blood and that the blood cells, while still detected in darkfield microscopy, do not impede the detection of the nanorods. The streaks in (B) and (C) are from the movement of the blood cells during exposure. The stationary blood cells in (B) are blood cells that have stuck to the substrate surface. All images were taken using a Canon 7D on a Nikon Eclipse L-150 Microscope at 100X magnification under halogen lamp illumination.

The detection modality was validated using NR20(860) nanorods functionalized with Streptococcus pneumoniae Monoclonal antibody to detect the presence of Streptococcus pneumoniae in a whole blood sample using darkfield microscopy. Figure 5.5 shows the performance of the functionalized nanorods as sensors for detecting bacterial presence. Identical areas imaged using brightfield and darkfield microscopy show that for the control system of whole blood with Streptococcus pneumoniae the bacteria is visible only in brightfield imaging. However, for the system with functionalized nanorods, clear bright spots are observed in darkfield imaging. These spots, when merged with the brightfield image, match the locations of bacteria, even when obscured by cells. Based upon this performance validation, a microfluidic sampling platform was designed for full sample interrogation.

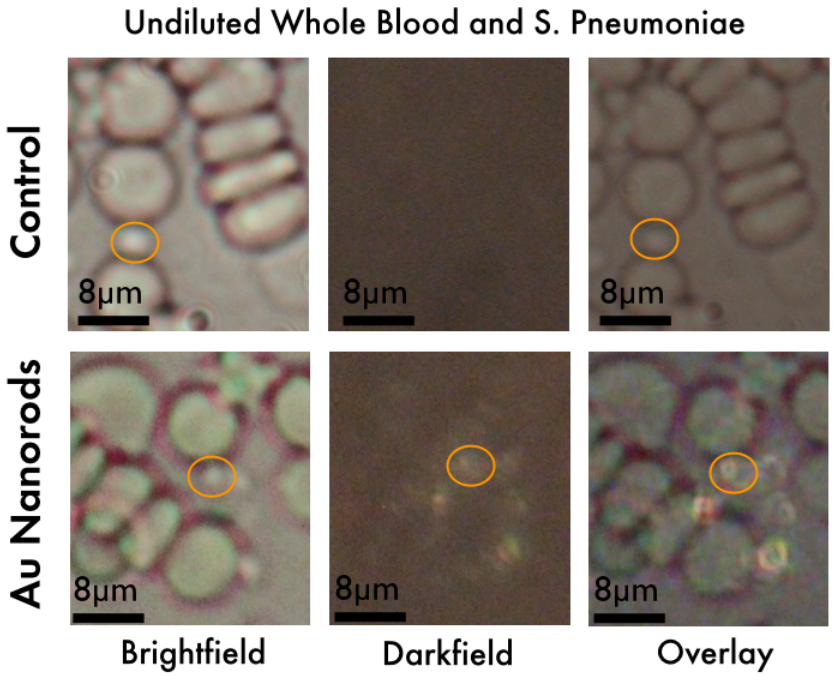


Figure 5.5: Detection of Streptococcus pneumoniae isolate D39 using functionalized N20(860) nanorods imaged using brightfield and darkfield microscopy. For the control system of whole blood and Streptococcus pneumoniae, the bacteria is clearly observed amongst the blood cells under brightfield microscopy. Neither was observed in darkfield microscopy. When functionalized nanorods are included in the sample, there is clear, observable scattering detected using darkfield microscopy. When the darkfield and brightfield images are merged, the scattering points and bacteria match locations. Non-specific binding is not observed.

## 5.4 Microfluidic absorbance-based gold nanoparticle detection

Initial platform development required validation of the detection of nanorod absorbance in a microfluidic channel. Several designs were developed to understand the detection sensitivity at small path lengths (20 $\mu$m) for dilute nanoparticle samples.

### 5.4.1 Substrate Material Characterization

To determine the optimal substrate for imaging gold nanoparticles in microfluidic channels using light scattering, initial detection measurements were recorded using darkfield microscopy. A darkfield image of N20(700) nanorods on a silicon / silicon–oxide substrate in solution underneath a glass coverslip at 50X magnification is shown in Figure 5.6. The nanorods were illuminated with the built-in halogen lamp of the Nikon Eclipse L-150 Upright Microscope.

The same N20(700) nanorods were then imaged on a borosilicate glass substrate in solution under the same illumination conditions through a glass coverslip at 50X, but as a result of the substrate's transparency, the nanorods could not be imaged in solution through a coverslip.

This set of experiments was then repeated using glancing–angle illumination from a laser diode both on and off peak resonance for the gold nanorod sample. The N20(700) nanorod sample was imaged in solution on both a silicon / silicon–oxide substrate and borosilicate glass substrate through a glass coverslip. The nanorod sample has an absorption peak near 690 nm as seen in the chart of Figure 5.7, corresponding to a common laser diode illumination source. Figure 5.7A shows the nanorod sample under illumination at a wavelength near the absorption peak. Figure 5.7B shows the nanorod sample

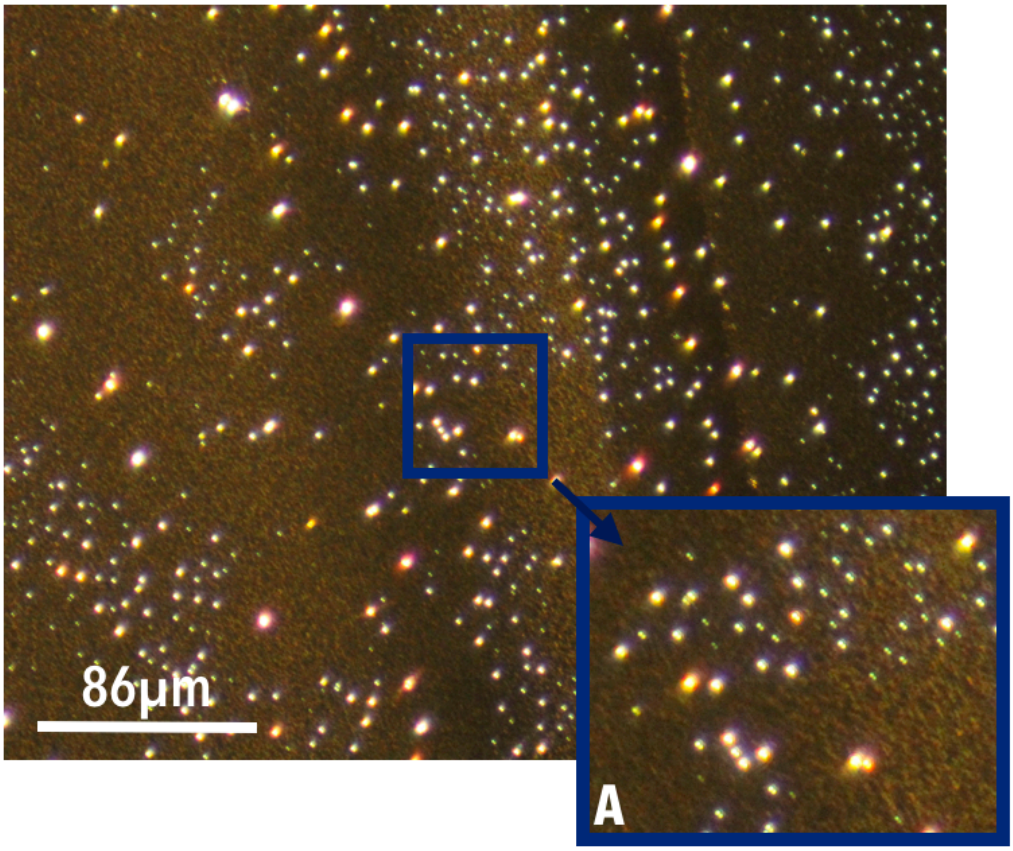


Figure 5.6: A darkfield image of N20(700) nanorods on a silicon / silicon-oxide substrate taken at 50X on a Nikon Eclipse L-150 Upright Microscope under halogen lamp illumination. The large bright spots are aggregated nanoparticles, while the small points are the light scattered by individual or dimer / trimer nanorod assemblies. The subfigure (A) is a 200% digitally magnified image of the identified region to show the difference between the individual nanoparticle points and the larger aggregated assemblies.

illuminated at a wavelength off the peak absorption wavelength, which for this sample is 785 nm.

As nanorods respond differently when illuminated with light at the peak and off–peak absorbance wavelengths, verification was required to determine if these differences could be observed in microfluidic channels. Using a three-sheath flow PDMS channel, the three nanorod samples were each introduced into the channel, illuminated on and off wavelength by the laser diodes, and the intensity across the channel measured. The samples were

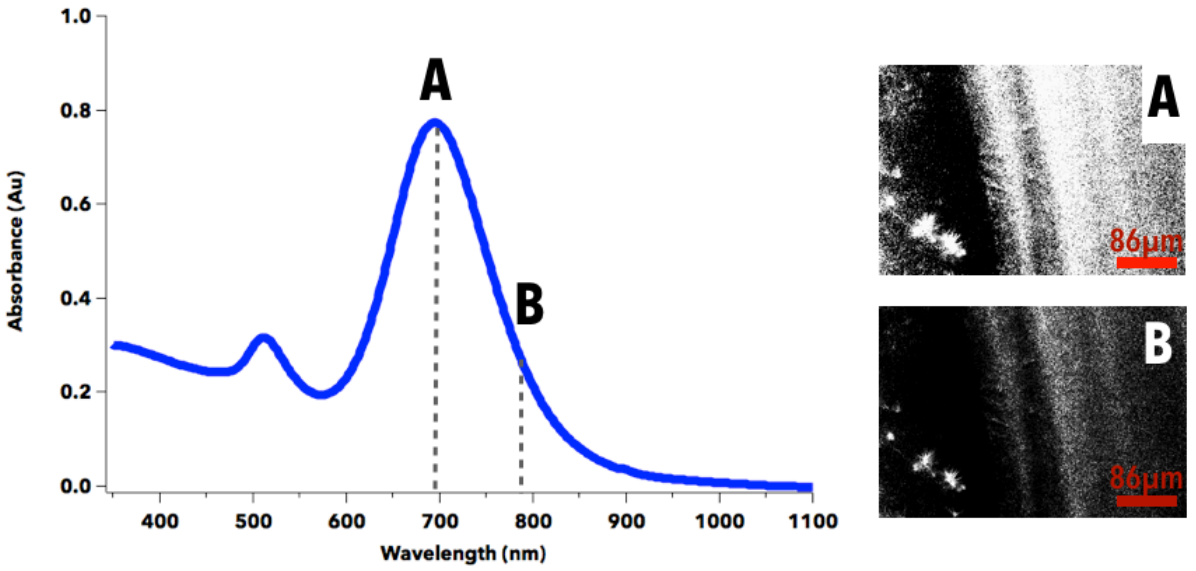


Figure 5.7: Laser Scattering Illumination. For the N20(700) nanorod, the absorbance spectra shows a clear absorbance peak (A) near 690 nm, the lasing wavelength of one of the laser diode illumination sources. By illuminating at that wavelength, the nanorods in solution on a silicon / silicon–oxide substrate are easily observed when imaged on an upright microscope (Nikon Eclipse L-150) at 50X magnification. When illuminated off–resonance at 785nm (B), the larger aggregates of nanorods are visible, but the individual nanorods no–longer exhibit the strong surface plasmon resonance as seen at 690 nm.

then simultaneously introduced to the channel and imaged at an illumination wavelength corresponding to one of the nanorod samples' absorbance peak.

In one example case, the channel is illuminated with the 690 nm wavelength laser corresponding to the absorbance peak of the N20(700) nanorods. Figure 5.8 shows the expected intensities of each nanorod sample at the 690 nm illumination wavelength as determined by comparing nanorod absorbance spectra. From this comparison, the N20(700) nanorods should be the brightest when illuminated at this wavelength, followed by the N20(650) nanorods and the N20(800) nanorods.

When the intensity is measured across the width of the channel, three clear, distinct intensity plateaus appear that correspond to the three different nanorod samples flowing through the sheath flow microfluidic device as seen in figure 5.9. It should be noted

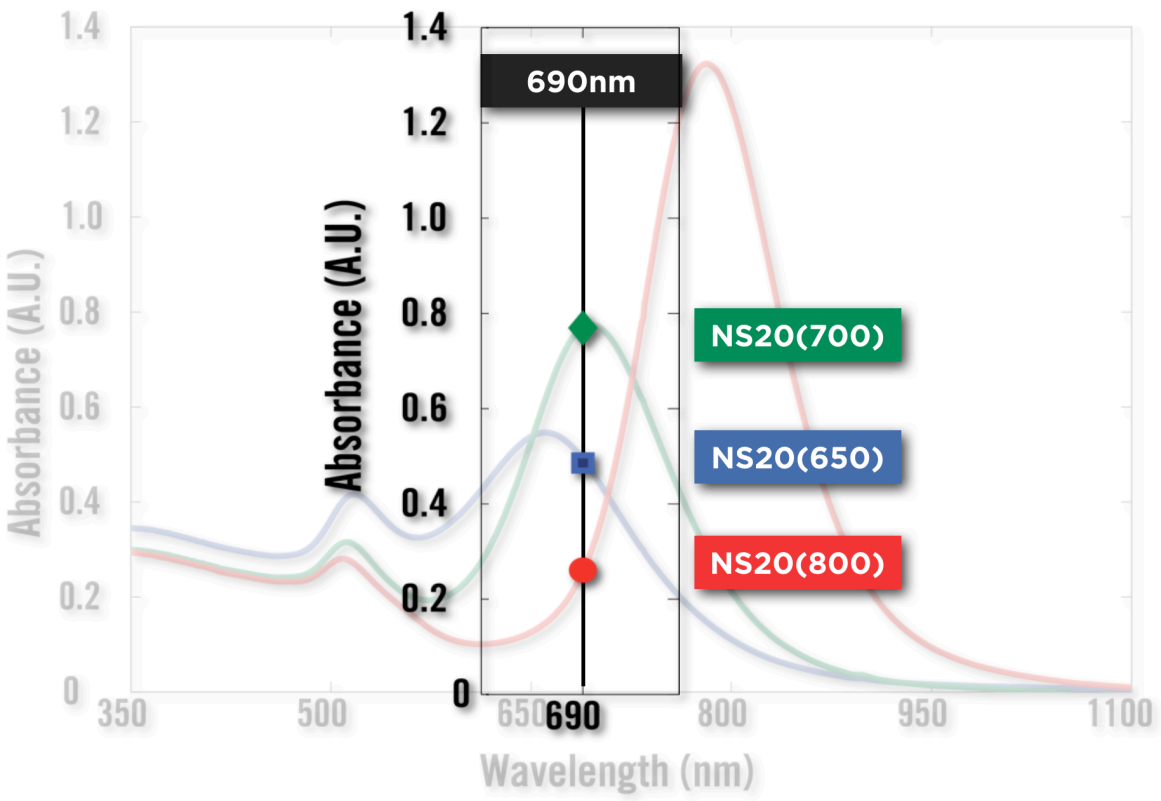


Figure 5.8: Comparison of the different nanorod samples relative absorption intensity at one illumination wavelength (690 nm) which corresponds to the absorption peak of the N20(700) nanorod sample. From this comparison, the 45nm nanorods should be the brightest when illuminated at this wavelength, followed by the N20(650) nanorods and the N20(800) nanorods.

that the pixel intensity measurements have been vertically binned while maintaining horizontal pixel fidelity.

As a consequence of these experiments, it was determined that different nanorods could be detected in microfluidic channels by using glancing–angle laser illumination at the surface plasmon resonance peak for different nanorod samples.

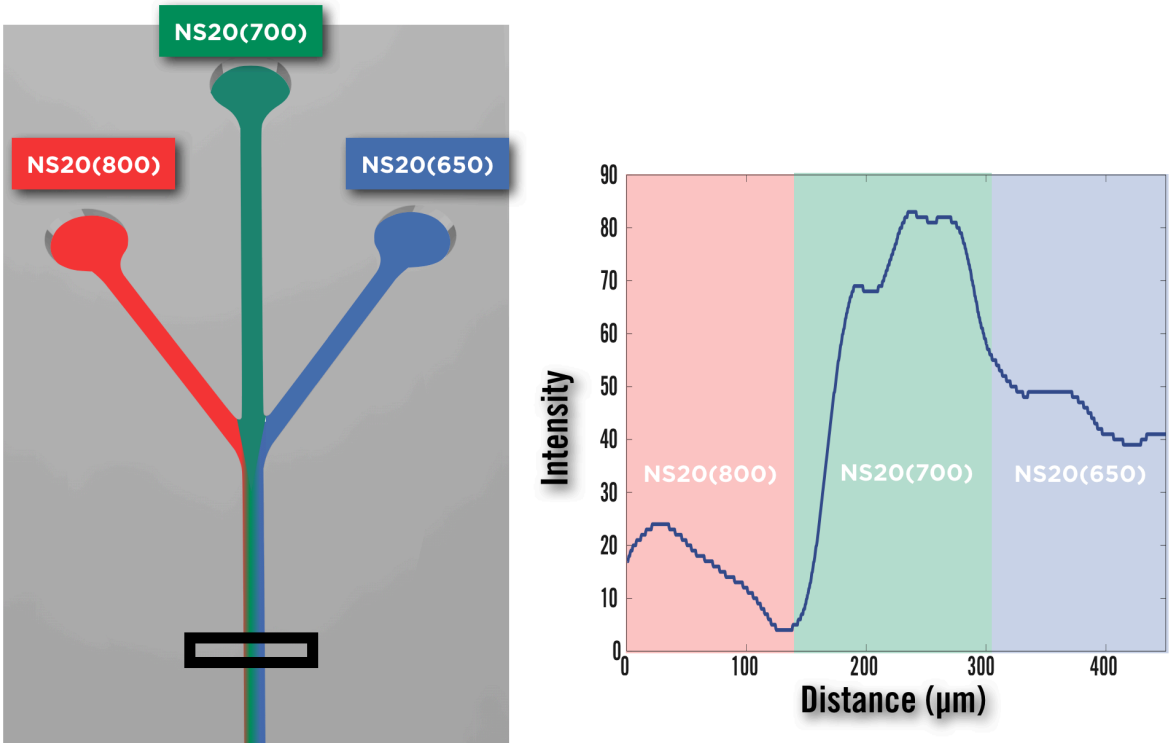


Figure 5.9: Sheath flow measurement of nanorod intensities under 690 nm laser illumination as imaged across the width of the microfluidic channel. The *left* figure is a schematic of the three-sheath flow microfluidic device with the position of the nanorod samples. The *right* figure is the pixel intensity measurement recorded by the Andor Luca EMCCD camera. The intensities have been vertically binned while maintaining horizontal pixel fidelity.

Although effective, the limitation of this approach is the reliance on specified illumination wavelengths corresponding to the LSPR absorbance peaks of the nanoparticle samples. Integrating microspectrophotometry to the microfluidic system would enable multiplexed nanoparticle detection without *a priori* information about the nanoparticle system. Multispectral detection would also enable the monitoring of changes in the LSPR peaks due to changes in surface functionalization, critical to both the bacterial detection platform along with general nanoparticle characterization.

To achieve this detection modality, a spectrophotometer was integrated into the optical path of an upright microscope as shown schematically in Figure 5.10. Figure 5.11 shows the actual instrumental setup. By integrating a white-light illumination source, the full absorbance spectra can be measured for a nanoparticle sample thereby providing a facile means to distinguish between nanoparticle populations.

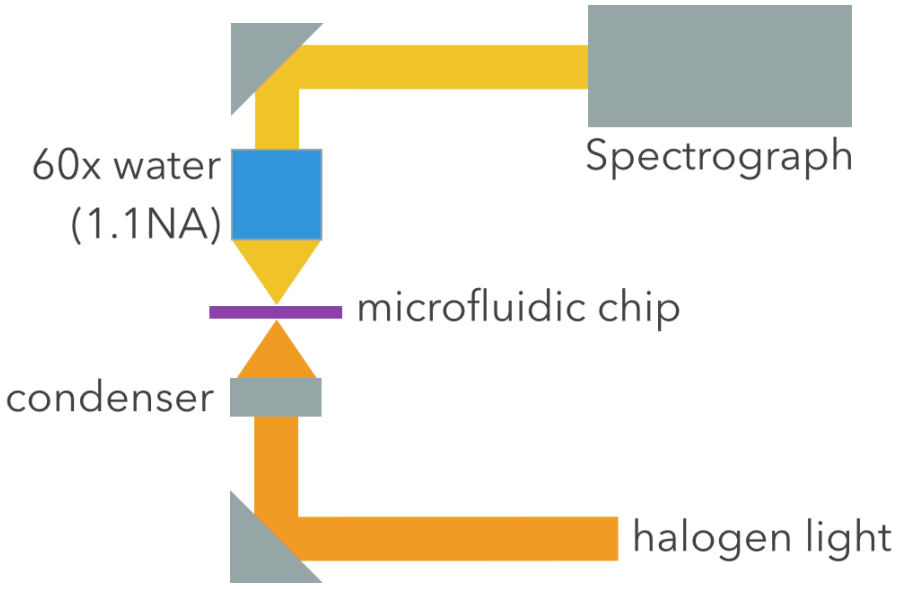


Figure 5.10: Schematic of the microfluidic-based microspectrophotometry system developed for nanorod characterization. White light illumination from a halogen source is coupled into a microfluidic channel and collected for detection using a spectrograph. Through this method, the full absorbance spectra is recorded for a nanoparticle population.

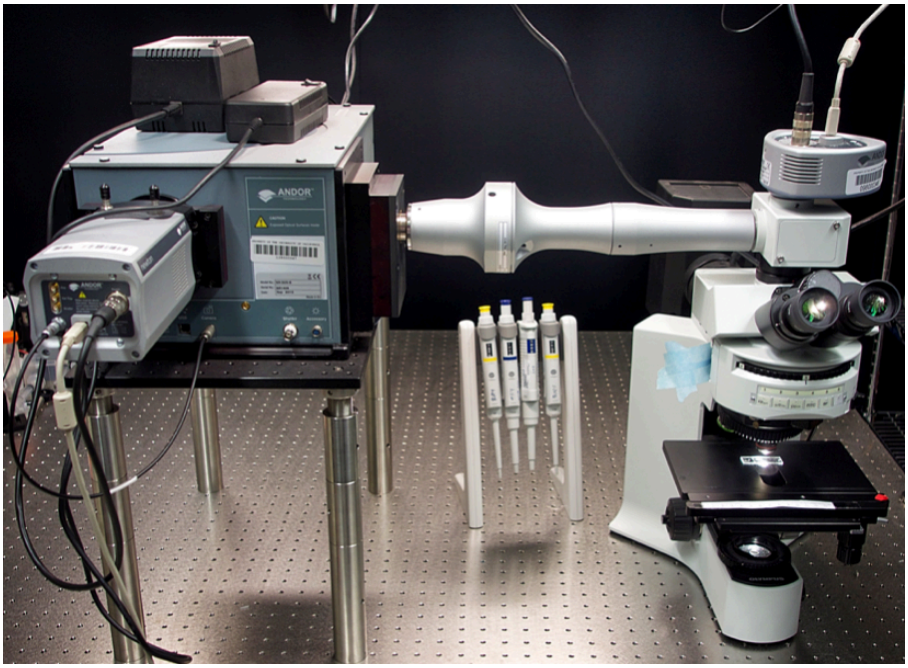


Figure 5.11: Experimental setup for microfluidic-based microspectrophotometry system. Using an Olympus BX-41 upright microscope as the imaging platform, a Andor Shamrock 303i spectrograph with a Newton camera is attached for spectral analysis. An Andor Luca camera is used to chip alignment verification.

A series of dilution tests were performed starting with the initial stock nanorod solution to characterize the sensitivity of the system. Figure 5.12 illustrates the sampling process whereby distinct nanoparticle samples are introduced to a single microfluidic channel via vacuum-driven flow separated from a water blank by air-bubble spacers. The use of water blanks ensured accurate baseline measurement before and after each nanoparticle sample.

Figure 5.13 shows the recorded signal for NR20(735) nanorod sample. The non-normalized intensity values (shown) are small as a result of the 20 $\mu$m measurement pathlength. The nanorod absorbance peak is clearly detected and measured using this technique. The noise in the signal is the result of variations in light intensity and increased stray scattering from the spectrograph diffraction grating when outside optimal range (for this grating, above 760 nm).

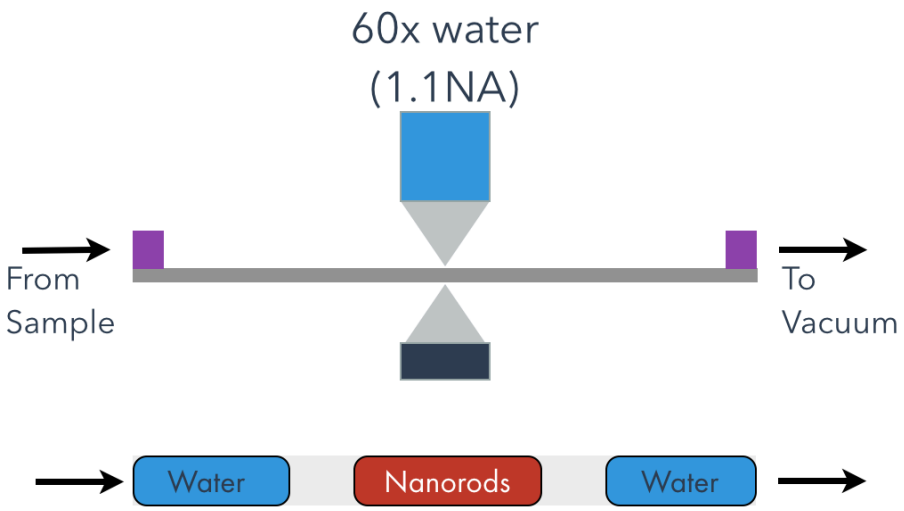


Figure 5.12: Illustration of the sampling process for the concentration validation measurements. Nanoparticle samples are introduced to a single microfluidic chip via vacuum-driven flow. Water is used as the spectral baseline and the two solutions are separated by air-bubble spacers.

The dilution series from stock NR20(735) nanorod concentration to a 1:32 dilution is shown as raw absorbance data in Figure 5.14. From the data only the stock, 1:2, and 1:4 solutions are resolved with clear peaks near 735 nm. As a result of intensity variations in the recorded absorbance spectra, the 1:8, 1:16, and 1:32 dilutions are not resolved. However, as shown in Figure 5.15, the high frequency noise in the signal from the intensity fluctuations can be removed using wavelet denoising analysis [119]. After denoising, the absorbance signals are significantly clearer enabling the resolution of the 1:8 dilution spectra, but the 1:16 and 1:32 spectra are still indistinguishable from the control signal.

As a detection platform, the microfluidic-microspectrophotometry system monitors the absorbance signal over time to capture the evolution of the characteristic LSPR peak as shown in Figure 5.16. Variations in sample concentration appear as gradients in peak intensity as expected from the serial dilution measurements. The platform can measure

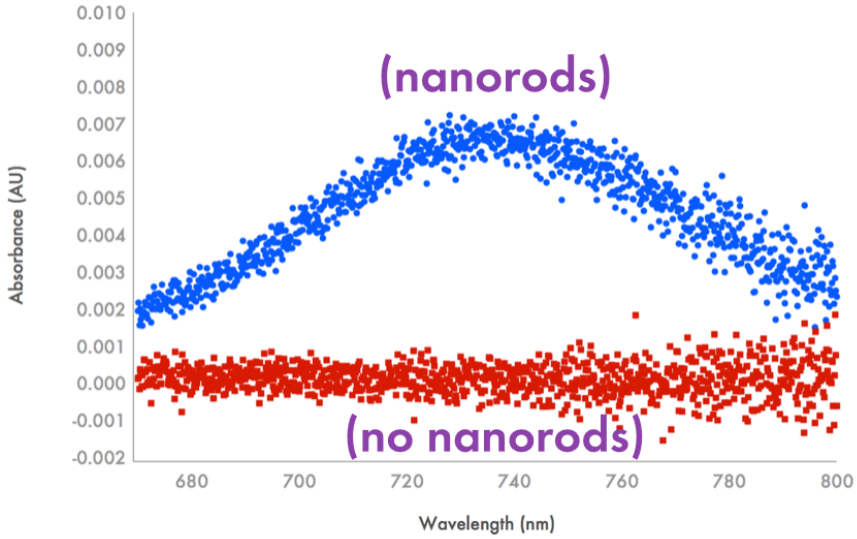


Figure 5.13: The recorded signal for NR20(735) nanorod sample. The non-normalized intensity values (shown) are small as a result of the 20 $\mu$m measurement pathlength.

stock nanorod concentrations, such as NR20(735) in Figure 5.16, but due to the noise from light intensity variations, concentrations relevant for capillary electrophoresis are undetectable.

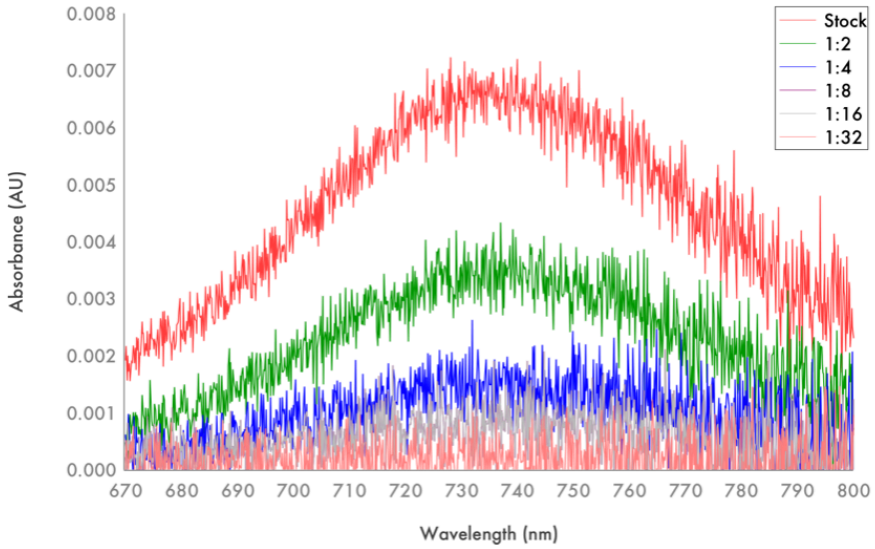


Figure 5.14: Dilution series of the NR20(735) nanorods from stock to 1:32. Raw absorbance spectra shows significant noise component due to fluctuations in the measured light intensity. The increase in noise with increasing wavelength is a function of instrument design and diffraction grating positioning. Stock, 1:2, and 1:4 measurements are resolved, but the remaining samples are not resolved above the baseline noise floor.

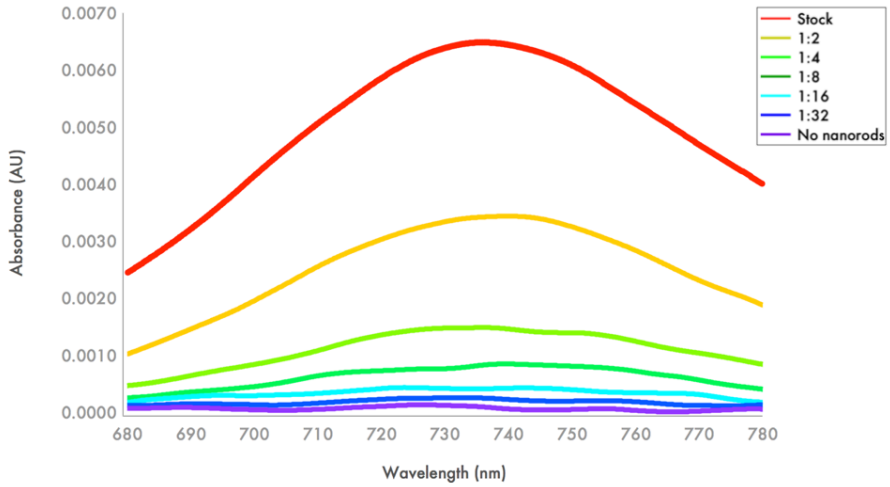


Figure 5.15: Dilution series of the NR20(735) nanorods from stock to 1:32. Denoised spectra from wavelet analysis shows significant noise reduction. Stock, 1:2, 1:4, 1:8 measurements are resolved, but the remaining samples are not resolved above the baseline noise floor.

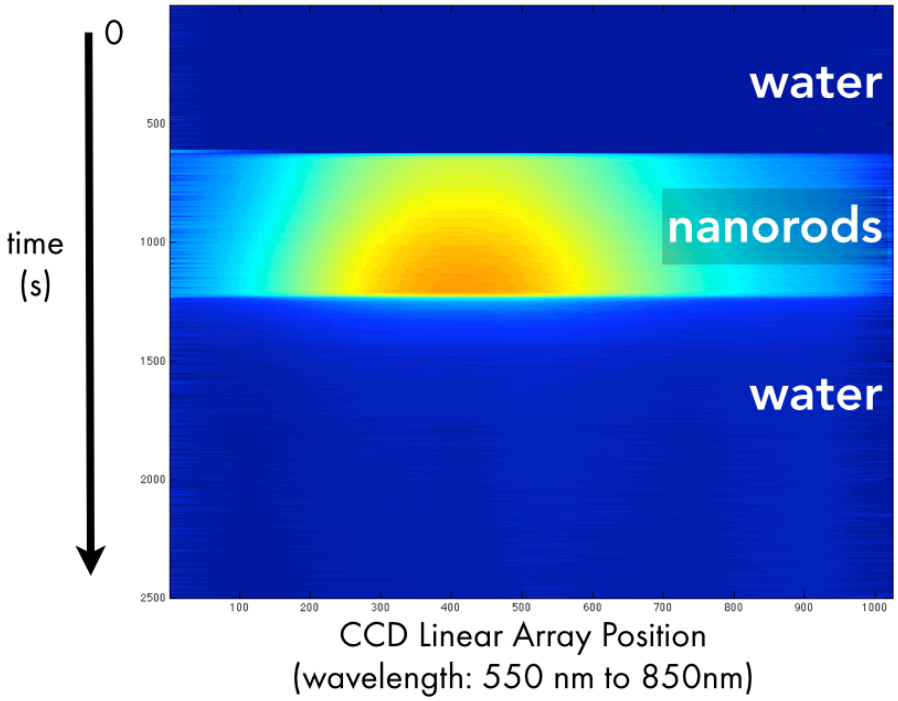


Figure 5.16: Evolution of absorbance spectra over time for the NR20(735) nanorod sample. As observed, the nanorod solution increases in concentration until a steady-state value is measured. Bubble spacers are used to separate the nanorods from the water samples.

## 5.5 Discussion

Accurate and rapid characterization of gold nanoparticles is critical for not only nanoparticle synthesis, but also for advancing gold nanoparticle application development. Limitations of current analytical techniques inhibits the full *in-situ* characterization of gold nanoparticles, such as the inability to distinguish the specific nature of the multiple peaks observed in the microchip capillary electrophoresis experiments discussed in Chapter 3. The benefits of doing on–chip absorbance measurements in conjunction with microchip CE separations are substantial as this would enable not only the ability to full characterize nanoparticles, but would also enable other spectroscopic technique such as localized surface plasmon resonance biosensing using the nanoparticles as the sensing medium.

The combination of microspectrophotometry and microfluidics has demonstrated the ability to characterize gold nanoparticle populations in real-time. However, noise from light intensity fluctuations inhibit the detection of nanoparticle populations at concentrations relevant for both biological sensing and nanoparticle characterization by microchip CE. The fluctuations in intensity are the result of instability in the illumination source rather than stray environmental light. A thorough investigation of different light sources yielded no improvements with the established system. Mercury lamps (Olympus), temperature stabilized fiber coupled mercury illuminators (Olympus), Halogen illuminators (Olympus, Prior Scientific), and a custom-built LED illuminator (Cree LED source) demonstrated significant time-resolved intensity instabilities. Without significant modifications to the experimental setup in the form of a custom-built microscope with temperature stabilized LED illumination, referenced mercury illumination, or integrated laser illumination, this technique will not achieve the necessary sensitivity required.

Integration of the absorbance spectrophotometry system with the nanoparticle de-

tection platform for blood sepsis does not require the same light stability with wide tunability as the nanoparticle characterization platform does. As the nanoparticle system is selected *a priori*, a laser source with a wavelength centered at the nanoparticle LSPR peak would be sufficient for detection measurements. By integrating the appropriate laser with the microfluidic chip, the next steps in platform development can proceed. Specifically, careful evaluation of the limits of detection, nanoparticle concentration, and resolution of the system is required. These steps must be conducted with active streptococcus pneumoniae from mouse blood cultures and simultaneously measured using culturing techniques as any variation in time between measurements will result in different bacteria concentrations.

The demonstration of both the microspectrophotometric microfluidic platform and the successful detection of streptococcus pneumoniae are significant steps towards a fully integrated blood sepsis analysis platform. By overcoming the noise limitation, this platform can also characterize nanoparticles using the increased specificity offered by microchip CE.

# Chapter 6

# Conclusions and Future Directions

Metallic nanoparticles are an exciting class of engineered materials that hold great promise for revolutionizing a wide array of fields and disciplines. Although utilized already in cosmetics, stain-resistant clothing, and diagnostics, significant challenges exist in adequately characterization nanoparticles. These challenges are both in the actual measurement of nanoparticle morphology, surface functionalization, polydispersity, and colloidal stability after synthesis, but also with understanding how the nanoparticles interact with the surrounding environment such nanoparticle toxicity to cells in bio-related applications or their presence in the environment as found in waste products. As a consequence, the ability to both engineer and safely use nanoparticles in a fully-realized manner depends solely upon our ability to characterize them.

This dissertation explores the fundamental difficulties in nanoparticle characterization in order to develop better methods than the traditionally used methods of TEM, DLS, and UV-Vis. This work shows that not only do these methods offer an incomplete picture of a nanoparticle population, but commercially available nanoparticles must be independently characterized before use in order to verify they are of the desired size, shape, and functionality.

Through this work, microfluidics is shown to be a powerful tool for accessing information about nanoparticle properties in a manner not traditionally available with standard analytical tools. However, much is required to fully develop the capabilities of both micro-CE and a fully-integrated microfluidic detection platform. Using this dissertation as a foundation, subsequent work would focus upon better understanding the separation mechanism of gold nanoparticle populations in micro-CE by evaluating the use of surfactants present in the running buffer and through integration of the micro-CE experiments with absorbance detection. This would enable the probing of the different sub-peak populations to ascertain the nanoparticle composition that forms each of the separated peaks. Fully integrating absorbance spectroscopy to on-chip microfluidic analysis would realize the potential of the light-scattering properties of the gold nanoparticles for biodetection / diagnostics. Shown to be a promising method for detecting the presence of pathogens in whole blood, further developing an understanding of the limits of detection, concentration dependence of the absorbance signal, and the time for full analysis would establish this method as a clinically relevant detection tool.

Both gold nanoparticles and microfluidics hold great promise as transformative technologies. It is the author's hope that with continued development by the scientific community as a whole, this promise can be realized in an meaningful, constructive, and broadly-applicable manner.

# Bibliography


[1] C. Toumey and NanoCenter, USC, *Reading Feynman into nanotechnology: a text for a new science*, *Techné* **12** (2008), no. 3 133.

[2] C. A. M. Roco, Mihail C. and M. C. Hersam, *Nanotechnology Research Directions for Societal Needs in 2020*, *Journal of nanoparticle research* **13** (2011), no. 3 1–607.

[3] J. F. Sargent, Jr, *The National Nanotechnology Initiative: Overview, Reauthorization, and Appropriations Issues*, *Congressional Research Service* **19** (2012) 2011.

[4] M. S. Olson and P. L. Gurian, *Risk assessment strategies as nanomaterials transition into commercial applications*, *Journal of Nanoparticle Research* **14** (Mar., 2012) 786.

[5] J. Liu, S. Legros, G. Ma, J. G. C. Veinot, F. von der Kammer, and T. Hofmann, *Influence of surface functionalization and particle size on the aggregation kinetics of engineered nanoparticles*, *Chemosphere* **87** (May, 2012) 918–924.

[6] C. J. Murphy and J. M. Buriak, *Best Practices for the Reporting of Colloidal Inorganic Nanomaterials*, *Chemistry of Materials* **27** (July, 2015) 4911–4913.

[7] T. R. Ray, B. Lettiere, J. de Rutte, and S. Pennathur, *Quantitative characterization of the colloidal stability of metallic nanoparticles using uv–vis absorbance spectroscopy*, *Langmuir* **31** (2015), no. 12 3577–3586. PMID: 25730093.

[8] M. Faraday, *The Bakerian lecture: experimental relations of gold (and other metals) to light*, *Philosophical Transactions of the Royal Society of London* **147** (1857) 145–181.

[9] P. P. Edwards and J. M. Thomas, *Gold in a Metallic Divided State—From Faraday to Present-Day Nanoscience*, *Angewandte Chemie International Edition* **46** (July, 2007) 5480–5486.

[10] C. M. Cobley, J. Chen, E. C. Cho, L. V. Wang, and Y. Xia, *Gold nanostructures: a class of multifunctional materials for biomedical applications*, *Chemical Society Reviews* **40** (2011), no. 1 44–56.

[11] E. C. Dreaden, A. M. Alkilany, X. Huang, C. J. Murphy, and M. A. El-Sayed, *The golden age: gold nanoparticles for biomedicine*, *Chemical Society Reviews* **41** (2012), no. 7 2740.

[12] S. Eustis and M. A. El-Sayed, *Why gold nanoparticles are more precious than pretty gold: Noble metal surface plasmon resonance and its enhancement of the radiative and nonradiative properties of nanocrystals of different shapes*, *Chemical Society Reviews* **35** (2006), no. 3 209.

[13] K. L. Kelly, E. Coronado, L. L. Zhao, and G. C. Schatz, *The optical properties of metal nanoparticles: the influence of size, shape, and dielectric environment*, *J. Phys. Chem. B* **107** (2003) 668–677.

[14] M. Pelton, J. Aizpurua, and G. Bryant, *Metal-nanoparticle plasmonics*, *Laser and Photon. Rev.* **2** (2008) 136–159.

[15] C. Sonnichsen, S. Geier, N. E. Hecker, G. von Plessen, J. Feldmann, H. Ditlbacher, B. Lamprecht, J. R. Krenn, F. R. Aussenegg, V. Z.-H. Chan, J. P. Spatz, and M. Moller, *Spectroscopy of single metallic nanoparticles using total internal reflection microscopy*, *Appl. Phys. Lett.* **77** (2000) 2949–2951.

[16] J. M. Brockman, B. P. Nelson, and R. M. Corn, *Surface plasmon resonance imaging measurements of ultrathin organic films*, *Annu. Rev. Phys. Chem.* **51** (2000) 41–63.

[17] C. J. Murphy, T. K. Sau, A. M. Gole, C. J. Orendorff, J. Gao, L. Gou, S. E. Hunyadi, and T. Li, *Anisotropic metal nanoparticles: Synthesis, assembly, and optical applications*, *J. Phys. Chem. B* **109** (2005) 13857–13870.

[18] M. B. Cortie, *The weird world of nanoscale gold*, *Gold Bulletin* **37** (2004) 12–19.

[19] C. J. Orendorff, T. Sau, and C. J. Murphy, *Shape-dependent plasmon-resonant gold nanoparticles*, *Small* **2** (2006) 636–639.

[20] C. J. Murphy, A. M. Gole, J. W. Stone, P. N. Sisco, A. M. Alkilany, E. C. Goldsmith, and S. C. Baxter, *Gold nanoparticles in biology: beyond toxicity to cellular imaging*, *Accounts Chem. Res.* **41** (2008) 1721–1730.

[21] C. Sonnichsen and A. P. Alivisatos, *Gold nanorods as novel nonbleaching plasmon-based orientation sensors for polarized single-particle microscopy*, *Nanoletters* **5** (2005) 301–304.

[22] C. J. Murphy and C. J. Orendorff, *Alignment of gold nanorods in polymer composites and on polymer surfaces*, *Adv. Mater.* **17** (2005) 2173–2177.

[23] P. K. Jain, X. Huang, I. H. El-Sayed, and M. A. El-Sayed, *Noble Metals on the Nanoscale: Optical and Photothermal Properties and Some Applications in Imaging, Sensing, Biology, and Medicine*, *Accounts of Chemical Research* **41** (Dec., 2008) 1578–1586.

[24] R. Sardar, A. M. Funston, P. Mulvaney, and R. W. Murray, *Gold Nanoparticles: Past, Present, and Future*, *Langmuir* **25** (Dec., 2009) 13840–13851.

[25] C. Gui and D. Cui, *Functionalized Gold Nanorods for Tumor Imaging and Targeted Therapy*, *Cancer Biology & Medicine* **9** (2012), no. 4 221–233.

[26] L. Dykman and N. Khlebtsov, *Gold nanoparticles in biomedical applications: recent advances and perspectives*, *Chemical Society Reviews* **41** (2012), no. 6 2256.

[27] S. E. Lohse and C. J. Murphy, *Applications of Colloidal Inorganic Nanoparticles: From Medicine to Energy*, *Journal of the American Chemical Society* **134** (Sept., 2012) 15607–15620.

[28] N. G. Khlebtsov, V. A. Bogatyrev, B. N. Khlebtsov, L. A. Dykman, and P. Englebienne, *A multilayer model for gold nanoparticle bioconjugates: application to study of gelatin and human IgG adsorption using extinction and light scattering spectra and the dynamic light scattering method*, *Colloid Journal* **65** (2003), no. 5 622–635.

[29] K.-S. Lee and M. A. El-Sayed, *Gold and Silver Nanoparticles in Sensing and Imaging: Sensitivity of Plasmon Response to Size, Shape, and Metal Composition*, *The Journal of Physical Chemistry B* **110** (Oct., 2006) 19220–19225.

[30] D. Gao, Z. Sheng, and H. Han, *An ultrasensitive method for the detection of gene fragment from transgenics using label-free gold nanoparticle probe and dynamic light scattering*, *Analytica Chimica Acta* **696** (June, 2011) 1–5.

[31] T. E. Pylaev, V. A. Khanadeev, B. N. Khlebtsov, L. A. Dykman, V. A. Bogatyrev, and N. G. Khlebtsov, *Colorimetric and dynamic light scattering detection of DNA sequences by using positively charged gold nanospheres: a comparative study with gold nanorods*, *Nanotechnology* **22** (May, 2011) 285501.

[32] J. D. Driskell, C. A. Jones, S. M. Tompkins, and R. A. Tripp, *One-step assay for detecting influenza virus using dynamic light scattering and gold nanoparticles*, *The Analyst* **136** (2011), no. 15 3083.

[33] X. Lu, X. Dong, K. Zhang, X. Han, X. Fang, and Y. Zhang, *A gold nanorods-based fluorescent biosensor for the detection of hepatitis B virus DNA based on fluorescence resonance energy transfer*, *The Analyst* **138** (2012), no. 2 642.

[34] H. Huang, F. Liu, S. Huang, S. Yuan, B. Liao, S. Yi, Y. Zeng, and P. K. Chu, *Sensitive and simultaneous detection of different disease markers using multiplexed gold nanorods*, *Analytica Chimica Acta* **755** (Nov., 2012) 108–114.

[35] G. K. Darbha, A. Ray, and P. C. Ray, *Gold Nanoparticle-Based Miniaturized Nanomaterial Surface Energy Transfer Probe for Rapid and Ultrasensitive Detection of Mercury in Soil, Water, and Fish*, *ACS Nano* **1** (Oct., 2007) 208–214.

[36] Y. Fan, Y. F. Long, and Y. F. Li, *A sensitive resonance light scattering spectrometry of trace Hg2+ with sulfur ion modified gold nanoparticles*, *Analytica Chimica Acta* **653** (Oct., 2009) 207–211.

[37] C. Xiong and L. Ling, *Label-free, sensitive detection of Hg(II) with gold nanoparticles by using dynamic light scattering technique*, *Talanta* **89** (Jan., 2012) 317–321.

[38] J. Z. James, D. Lucas, and C. P. Koshland, *Elemental mercury vapor interaction with individual gold nanorods*, *The Analyst* **138** (2013), no. 8 2323–2328.

[39] J. R. Kalluri, T. Arbneshi, S. Afrin Khan, A. Neely, P. Candice, B. Varisli, M. Washington, S. McAfee, B. Robinson, S. Banerjee, A. K. Singh, D. Senapati, and P. C. Ray, *Use of Gold Nanoparticles in a Simple Colorimetric and Ultrasensitive Dynamic Light Scattering Assay: Selective Detection of Arsenic in Groundwater*, *Angewandte Chemie International Edition* **48** (Nov., 2009) 9668–9671.

[40] D. Pissuwan, S. M. Valenzuela, and M. B. Cortie, *Therapeutic possibilities of plasmonically heated gold nanoparticles*, *Trends in Biotechnology* **24** (Feb., 2006) 62–67.

[41] D. K. Kirui, S. Krishnan, A. D. Strickland, and C. A. Batt, *PAA-Derived Gold Nanorods for Cellular Targeting and Photothermal Therapy*, *Macromolecular Bioscience* **11** (Mar., 2011) 779–788.

[42] J. W. Stone, P. N. Sisco, E. C. Goldsmith, S. C. Baxter, and C. J. Murphy, *Using gold nanorods to probe cell-induced collagen deformation*, *Nanoletters* **7** (2007) 116–119.

[43] V. M. Shalaev, W. Cai, U. K. Chettiar, H.-K. Yuan, A. K. Sarychev, V. P. Drachev, and A. V. Kildishev, *Negative index of refraction in optical metamaterials*, *Opt. Lett.* **30** (2005) 3356–3358.

[44] N. R. Jana, L. Gearheart, and C. J. Murphy, *Seed-mediated growth approach for shape-controlled synthesis of spheroidal and rod-like gold nanoparticles using a surfactant template*, *Adv. Mat.* **13** (2001) 1389–1393.

[45] N. R. Jana, L. Gearheart, and C. J. Murphy, *Wet chemical synthesis of high aspect ratio cylindrical gold nanorods*, *J. Phys. Chem. B* **105** (2001) 4065–4067.

[46] A. Wei, J. G. Mehtala, and A. K. Patri, *Challenges and opportunities in the advancement of nanomedicines*, *Journal of controlled release* **164** (Dec., 2012) 236–246.

[47] C. J. Murphy, T. K. Sau, A. M. Gole, C. J. Orendorff, J. Gao, L. Gou, S. E. Hunyadi, and T. Li, *Anisotropic Metal Nanoparticles: Synthesis, Assembly, and Optical Applications*, *The Journal of Physical Chemistry B* **109** (July, 2005) 13857–13870.

[48] U. Kätzel, R. Bedrich, M. Stintz, R. Ketzmerick, T. Gottschalk-Gaudig, and H. Barthel, *Dynamic Light Scattering for the Characterization of Polydisperse Fractal Systems: I. Simulation of the Diffusional Behavior*, *Particle & Particle Systems Characterization* **25** (Feb., 2008) 9–18.

[49] *NanoDLSay: a new platform technology for biomolecular detection and analysis using gold nanoparticle probes coupled with dynamic light scattering*, Proceedings of SPIE - the International Society for Optical Engineering, 2010.

[50] R. D. Boyd, S. K. Pichaimuthu, and A. Cuenat, *New approach to inter-technique comparisons for nanoparticle size measurements; using atomic force microscopy, nanoparticle tracking analysis and dynamic light scattering*, *Colloids and Surfaces A: Physicochemical and Engineering Aspects* **387** (Aug., 2011) 35–42.

[51] M. Hanauer, S. Pierrat, I. Zins, A. Lotz, and C. Sönnichsen, *Separation of Nanoparticles by Gel Electrophoresis According to Size and Shape*, *Nano Letters* **7** (Sept., 2007) 2881–2885.

[52] F.-K. Liu and G.-T. Wei, *Adding sodium dodecylsulfate to the running electrolyte enhances the separation of gold nanoparticles by capillary electrophoresis*, *Analytica Chimica Acta* **510** (May, 2004) 77–83.

[53] M. Napoli, P. Atzberger, and S. Pennathur, *Experimental study of the separation behavior of nanoparticles in micro- and nanochannels*, *Microfluidics and Nanofluidics* **10** (June, 2010) 69–80.

[54] S. Pennathur and D. Fygenson, *Improving fluorescence detection in lab on chip devices*, *Lab on a Chip* **8** (2008), no. 5 649–652.

[55] L. C. Jellema, T. Mey, S. Koster, and E. Verpoorte, *Charge-based particle separation in microfluidic devices using combined hydrodynamic and electrokinetic effects*, *Lab chip* **9** (2009), no. 13 1914–1925.

[56] K. E. Sapsford, K. M. Tyner, B. J. Dair, J. R. Deschamps, and I. L. Medintz, *Analyzing Nanomaterial Bioconjugates: A Review of Current and Emerging Purification and Characterization Techniques*, *Analytical Chemistry* **83** (June, 2011) 4453–4488.

[57] M. Zimbone, L. Calcagno, G. Messina, P. Baeri, and G. Compagnini, *Dynamic light scattering and UV–vis spectroscopy of gold nanoparticles solution*, *Materials Letters* **65** (Oct., 2011) 2906–2909.

[58] Y. Lu, L. Wang, D. Chen, and G. Wang, *Determination of the Concentration and the Average Number of Gold Atoms in a Gold Nanoparticle by Osmotic Pressure*, *Langmuir* **28** (June, 2012) 9282–9287.

[59] A. M. Alkilany, L. B. Thompson, S. P. Boulos, P. N. Sisco, and C. J. Murphy, *Gold nanorods: Their potential for photothermal therapeutics and drug delivery, tempered by the complexity of their biological interactions*, *Advanced Drug Delivery Reviews* **64** (Feb., 2012) 190–199.

[60] T. Ito, L. Sun, M. A. Bevan, and R. M. Crooks, *Comparison of Nanoparticle Size and Electrophoretic Mobility Measurements Using a Carbon-Nanotube-Based Coulter Counter, Dynamic Light Scattering, Transmission Electron Microscopy, and Phase Analysis Light Scattering*, *Langmuir* **20** (Aug., 2004) 6940–6945.

[61] D. Mahl, J. Diendorf, W. Meyer-Zaika, and M. Epple, *Possibilities and limitations of different analytical methods for the size determination of a bimodal dispersion of metallic nanoparticles*, *Colloids Surf., A* **377** (Mar., 2011) 386–392.

[62] M. Zimbone, L. Calcagno, P. Baeri, G. C. Messina, and G. Compagnini, *Dynamic light scattering in gold colloids prepared by laser ablation in water*, *Applied Surface Science* **258** (Sept., 2012) 9246–9249.

[63] A. Mishra, S. Ram, and G. Ghosh, *Dynamic Light Scattering and Optical Absorption in Biological Nanofluids of Gold Nanoparticles in Poly(vinyl pyrrolidone) Molecules*, *Journal of Physical Chemistry C* **113** (Apr., 2009) 6976–6982.

[64] H. Jans, X. Liu, L. Austin, G. Maes, and Q. Huo, *Dynamic Light Scattering as a Powerful Tool for Gold Nanoparticle Bioconjugation and Biomolecular Binding Studies*, *Analytical Chemistry* **81** (Nov., 2009) 9425–9432.

[65] H. Liu, N. Pierre-Pierre, and Q. Huo, *Dynamic light scattering for gold nanorod size characterization and study of nanorod–protein interactions*, *Gold Bulletin* **45** (Sept., 2012) 187–195.

[66] J. Rodriguez-Fernandez, J. Perez-Juste, L. M. Liz-Marzan, and P. R. Lang, *Dynamic light scattering of short au rods with low aspect ratios*, *J. Phys. Chem. C* **111** (Apr., 2007) 5020–5025.

[67] M. Glidden and M. Muschol, *Characterizing Gold Nanorods in Solution Using Depolarized Dynamic Light Scattering*, *Journal of Physical Chemistry C* **116** (Apr., 2012) 8128–8137.

[68] B. Khlebtsov and N. Khlebtsov, *On the measurement of gold nanoparticle sizes by the dynamic light scattering method*, *Colloid J.* **73** (2011), no. 1 118–127.

[69] H. Kato, M. Suzuki, K. Fujita, M. Horie, S. Endoh, Y. Yoshida, H. Iwahashi, K. Takahashi, A. Nakamura, and S. Kinugasa, *Reliable size determination of nanoparticles using dynamic light scattering method for in vitro toxicology assessment*, *Toxicology in Vitro* **23** (Aug., 2009) 927–934.

[70] P. Zijlstra, M. van Stee, N. Verhart, Z. Gu, and M. Orrit, *Rotational diffusion and alignment of short gold nanorods in an external electric field*, *Physical Chemistry Chemical Physics* **14** (2012), no. 13 4584.

[71] V. Myroshnychenko, J. Rodríguez-Fernández, I. Pastoriza-Santos, A. M. Funston, C. Novo, P. Mulvaney, L. M. Liz-Marzán, and F. J. García de Abajo, *Modelling the optical response of gold nanoparticles*, *Chemical Society Reviews* **37** (2008), no. 9 1792.

[72] K. K. Caswell, C. M. Bender, and C. J. Murphy, *Seedless, Surfactantless Wet Chemical Synthesis of Silver Nanowires*, *Nano Letters* **3** (May, 2003) 667–669.

[73] Ã. K. Jamting, J. Cullen, V. A. Coleman, M. Lawn, J. Herrmann, J. Miles, and M. J. Ford, *Systematic study of bimodal suspensions of latex nanoparticles using dynamic light scattering*, *Advanced Powder Technology* **22** (Mar., 2011) 290–293.

[74] T. L. Doane, C.-H. Chuang, R. J. Hill, and C. Burda, *Nanoparticle $\zeta$ -Potentials*, *Accounts of Chemical Research* **45** (Mar., 2012) 317–326.

[75] I. Medina-Ramirez, S. Bashir, Z. Luo, and J. L. Liu, *Green synthesis and characterization of polymer-stabilized silver nanoparticles*, *Colloids and Surfaces B: Biointerfaces* **73** (Oct., 2009) 185–191.

[76] V. Sharma, K. Park, and M. Srinivasarao, *Colloidal dispersion of gold nanorods: Historical background, optical properties, seed-mediated synthesis, shape separation and self-assembly*, *Materials Science and Engineering: R: Reports* **65** (May, 2009) 1–38.

[77] H. Nolte, C. Schilde, and A. Kwade, *Determination of particle size distributions and the degree of dispersion in nanocomposites*, *Composites Science and Technology* **72** (May, 2012) 948–958.

[78] B. R. Jennings and H. G. Jerrard, *Rayleigh-Gans-Debye and Mie theories in the determination of spherical particle sizes*, *Journal of colloid science* **20** (1965), no. 5 448–452.

[79] J.-f. Liu, S.-j. Yu, Y.-g. Yin, and J.-b. Chao, *Methods for separation, identification, characterization and quantification of silver nanoparticles*, *TrAC Trends in Analytical Chemistry* **33** (Mar., 2012) 95–106.

[80] R. Xu, *Progress in nanoparticles characterization: Sizing and zeta potential measurement*, *Particuology* **6** (Apr., 2008) 112–115.

[81] N. Surugau and P. L. Urban, *Electrophoretic methods for separation of nanoparticles*, *Journal of Separation Science* **32** (June, 2009) 1889–1906.

[82] X. Wang, Y. Li, H. Wang, Q. Fu, J. Peng, Y. Wang, J. Du, Y. Zhou, and L. Zhan, *Gold nanorod-based localized surface plasmon resonance biosensor for sensitive detection of hepatitis B virus in buffer, blood serum and plasma*, *Biosensors and Bioelectronics* **26** (Oct., 2010) 404–410.

[83] C. Kuemin, L. Nowack, L. Bozano, N. D. Spencer, and H. Wolf, *Oriented Assembly of Gold Nanorods on the Single-Particle Level*, *Advanced Functional Materials* **22** (Dec., 2011) 702–708.

[84] A. R. M. N. Afrooz, S. T. Sivalapalan, C. J. Murphy, S. M. Hussain, J. J. Schlager, and N. B. Saleh, *Spheres vs. rods: The shape of gold nanoparticles influences aggregation and deposition behavior*, *Chemosphere* **91** (Mar., 2013) 93–98.

[85] H. Su, Q. Ma, K. Shang, T. Liu, H. Yin, and S. Ai, *Gold nanoparticles as colorimetric sensor: A case study on E. coli O157:H7 as a model for Gram-negative bacteria*, *Sensors & Actuators: B. Chemical* **161** (Jan., 2012) 298–303.

[86] O. Lee, S. H. Jeong, W. U. Shin, G. Lee, C. Oh, and S. W. Son, *Influence of surface charge of gold nanorods on skin penetration*, *Skin Research and Technology* **19** (July, 2012) e390–e396.

[87] J. N. Anker, W. P. Hall, O. Lyandres, N. C. Shah, J. Zhao, and R. P. Van Duyne, *Biosensing with plasmonic nanosensors*, *Nat. Mater.* **7** (June, 2008) 442–453.

[88] A. Llevot and D. Astruc, *Applications of vectorized gold nanoparticles to the diagnosis and therapy of cancer*, *Chem. Soc. Rev.* **41** (2011), no. 1 242–257.

[89] A. K. Gupta and M. Gupta, *Synthesis and surface engineering of iron oxide nanoparticles for biomedical applications*, *Biomaterials* **26** (June, 2005) 3995–4021.

[90] J. Jain, S. Arora, J. M. Rajwade, P. Omray, S. Khandelwal, and K. M. Paknikar, *Silver nanoparticles in therapeutics: Development of an antimicrobial gel formulation for topical use*, *Mol. Pharm.* **6** (Oct., 2009) 1388–1401.

[91] H. A. Atwater and A. Polman, *Plasmonics for improved photovoltaic devices*, *Nature Publishing Group* **9** (Feb., 2010) 205–213.

[92] A. S. Aricò, P. Bruce, B. Scrosati, and J. M. Tarascon, *Nanostructured materials for advanced energy conversion and storage devices*, *Nature Materials* **4** (2005), no. 5 366–377.

[93] M. C. Daniel and D. Astruc, *Gold nanoparticles: Assembly, supramolecular chemistry, quantum size related properties, and applications toward biology, catalysis, and nanotechnology*, *Chemical Reviews* **104** (2004), no. 1 293–346.

[94] C. Andreou, M. R. Hoonejani, M. R. Barmi, M. Moskovits, and C. D. Meinhart, *Rapid detection of drugs of abuse in saliva using surface enhanced raman spectroscopy and microfluidics*, *ACS Nano* **7** (Aug., 2013) 7157–7164.

[95] X. Qu, P. J. J. Alvarez, and Q. Li, *Applications of nanotechnology in water and wastewater treatment*, *Water Res.* **47** (Aug., 2013) 3931–3946.

[96] S. Bandyopadhyay, J. R. Peralta-Videa, J. A. Hernandez-Viezcas, M. O. Montes, A. A. Keller, and J. L. Gardea-Torresdey, *Microscopic and spectroscopic methods applied to the measurements of nanoparticles in the environment*, *Appl. Spectrosc. Rev.* **47** (Apr., 2012) 180–206.

[97] B. M. S. Lopez-Lorente, A. I. and M. Valcarcel, *Electrophoretic methods for the analysis of nanoparticles*, *TrAC Trends in Analytical Chemistry* **30** (2011), no. 1 58–71.

[98] W. M. Hwang, C. Y. Lee, and D. W. Boo, *Separation of nanoparticles in different sizes and compositions by capillary electrophoresis*, *Bulletin–Korea Chemical Society* **24** (2003), no. 5 684–686.

[99] D. A. Hoagland, E. Arvanitidou, and C. Welch, *Capillary Electrophoresis Measurements of the Free Solution Mobility for Several Model Polyelectrolyte Systems*, *Macromolecules* **32** (Sept., 1999) 6180–6190.

[100] C. K. Lo, M. C. Paau, D. Xiao, and M. Choi, *Capillary Electrophoresis, Mass Spectrometry, and UV-Visible Absorption Studies on Electrolyte-Induced Fractionation of Gold Nanoclusters*, *Analytical Chemistry* **80** (2008), no. 7 2439–2446.

[101] J.-Y. Kim, H.-B. Kim, and D.-J. Jang, *Electrophoretic separation of gold nanoparticles according to bifunctional molecules-induced charge and size*, *Electrophoresis* **34** (2013), no. 5 911–916.

[102] *Gold nanoparticle sizing based on differential static light scattering spectroscopy, absorption spectroscopy, and dynamic light scattering*, Proceedings of SPIE - the International Society for Optical Engineering, 2004.

[103] L. Ossicini, *Electrophoretic methods: State of the art, trends and developments*, *Microchemical Journal* **46** (1992), no. 3 399–417.

[104] X. Xu, K. K. Caswell, E. Tucker, S. Kabisatpathy, K. L. Brodhacker, and W. A. Scrivens, *Size and shape separation of gold nanoparticles with preparative gel electrophoresis*, *Journal of Chromatography A* **1167** (Oct., 2007) 35–41.

[105] J. P. Landers, *Handbook of capillary and microchip electrophoresis and associated microtechniques*. CRC press, 2007.

[106] U. Pyell, *Characterization of nanoparticles by capillary electromigration separation techniques*, *Electrophoresis* **31** (2010), no. 5 814–831.

[107] U. Pyell, A. H. Jalil, C. Pfeiffer, B. Pelaz, and W. J. Parak, *Characterization of gold nanoparticles with different hydrophilic coatings via capillary electrophoresis and taylor dispersion analysis. part i: Determination of the zeta potential employing a modified analytic approximation*, *Journal of colloid and interface science* **450** (2015), no. C 288–300.

[108] M. Stanisavljevic, M. Vaculovicova, R. Kizek, and V. Adam, *Capillary electrophoresis of quantum dots: Minireview*, *Electrophoresis* **35** (May, 2014) 1929–1937.

[109] M. A. Rodriguez and D. W. Armstrong, *Separation and analysis of colloidal/nano-particles including microorganisms by capillary electrophoresis: a fundamental review*, *Journal of Chromatography B* **800** (Feb., 2004) 7–25.

[110] F.-K. Liu, F.-H. Ko, P.-W. Huang, C.-H. Wu, and T.-C. Chu, *Studying the size/shape separation and optical properties of silver nanoparticles by capillary electrophoresis*, *Journal of Chromatography A* **1062** (Jan., 2005) 139–145.

[111] K.-H. Lin, T.-C. Chu, and F.-K. Liu, *On-line enhancement and separation of nanoparticles using capillary electrophoresis*, *Journal of Chromatography A* **1161** (Aug., 2007) 314–321.

[112] F.-K. Liu, *A high-efficiency capillary electrophoresis-based method for characterizing the sizes of Au nanoparticles*, *Journal of Chromatography A* **1167** (Oct., 2007) 231–235.

[113] K. B. Mogensen, H. Klank, and J. r. P. Kutter, *Recent developments in detection for microfluidic systems*, *Electrophoresis* **25** (Nov., 2004) 3498–3512.

[114] M. H. Oddy, *Electrokinetic transport phenomena: Mobility measurement and electrokinetic instability.* PhD thesis, Stanford University, 2005.

[115] C. Nilsson, S. Birnbaum, and S. Nilsson, *Use of nanoparticles in capillary and microchip electrochromatography*, *Journal of Chromatography A* **1168** (Oct., 2007) 212–224.

[116] C. A. Schneider, W. S. Rasband, and K. W. Eliceiri, *Nih image to imagej: 25 years of image analysis*, *Nature methods* **9** (2012), no. 7 671–675.

[117] Z. J. Hu, S. Hou, Y. L. Ji, T. Wen, W. Q. Liu, H. Zhang, X. W. Shi, J. Yan, and X. C. Wu, *Fast characterization of gold nanorods ensemble by correlating its structure with optical extinction spectral features*, *AIP Advances* **4** (Nov., 2014) 117137–12.

[118] V. Amendola and M. Meneghetti, *Size Evaluation of Gold Nanoparticles by UV−vis Spectroscopy*, *Journal of Physical Chemistry C* **113** (Mar., 2009) 4277–4285.

[119] R. Baraniuk, H. Choi, R. Neelamani, V. Ribeiro, J. Romberg, H. Guo, F. Fernandes, B. Hendricks, R. Gopinath, M. Lang, *et. al.*, *Rice wavelet toolbox*, 1993.

[120] J. Shang and X. Gao, *Nanoparticle counting: Towards accurate determination of the molar concentration*, *Chemical Society Reviews* **43** (2014), no. 21 7267–7278.

[121] S. K. Brar and M. Verma, *Measurement of nanoparticles by light-scattering techniques*, *Trends in Analytical Chemistry* **30** (Jan., 2011) 4–17.

[122] S. K. Ghosh and T. Pal, *Interparticle coupling effect on the surface plasmon resonance of gold nanoparticles: From theory to applications*, *Chem. Rev.* **107** (Nov., 2007) 4797–4862.

[123] J. Cao, T. Sun, and K. T. V. Grattan, *Gold nanorod-based localized surface plasmon resonance biosensors: A review*, *Sensors & Actuators: B. Chemical* **195** (May, 2014) 332–351.

[124] W. Haiss, N. T. K. Thanh, J. Aveyard, and D. G. Fernig, *Determination of Size and Concentration of Gold Nanoparticles from UV−Vis Spectra*, *Analytical Chemistry* **79** (June, 2007) 4215–4221.

[125] P. B. Johnson and R.-W. Christy, *Optical constants of the noble metals*, *Physical Review B* **6** (1972), no. 12 4370.

[126] R. Gans, *Über die form ultramikroskopischer goldteilchen*, *Annalen der Physik* **342** (1912), no. 5 881–900.

[127] S. Link, M. B. Mohamed, and M. A. El-Sayed, *Simulation of the Optical Absorption Spectra of Gold Nanorods as a Function of Their Aspect Ratio and the Effect of the Medium Dielectric Constant*, *The Journal of Physical Chemistry B* **103** (Apr., 1999) 3073–3077.

[128] S. Eustis and M. A. El-Sayed, *Determination of the aspect ratio statistical distribution of gold nanorods in solution from a theoretical fit of the observed inhomogeneously broadened longitudinal plasmon resonance absorption spectrum*, *Journal of Applied Physics* **100** (2006), no. 4 044324–8.

[129] J. G. Mehtala and A. Wei, *Nanometric Resolution in the Hydrodynamic Size Analysis of Ligand-Stabilized Gold Nanorods*, *Langmuir* **30** (Nov., 2014) 13737–13743.

[130] W. Brown, *Dynamic light scattering: the method and some applications*, vol. 49. Oxford University Press, USA, 1993.

[131] N. C. Bell, C. Minelli, J. Tompkins, M. M. Stevens, and A. G. Shard, *Emerging Techniques for Submicrometer Particle Sizing Applied to Stöber Silica*, *Langmuir* **28** (July, 2012) 10860–10872.

[132] V. A. Bloomfield, *On-line biophysics textbook: Separations and hydrodynamics*, 2000.

[133] J. E. Sader, *Accurate analytic formulae for the far field effective potential and surface charge density of a uniformly charged sphere*, *Journal of colloid and interface science* **188** (1997), no. 2 508–510.

[134] A. Delgado, F. González-Caballero, and J. Salcedo, *On the zeta potential of spherical polystyrene particles from electrophoresis theories - Delgado - 2003 - Acta Polymerica - Wiley Online Library*, *Acta Polymerica* **37** (June, 1986) 361–364.

[135] H. Ohshima, *Approximate Analytic Expression for the Electrophoretic Mobility of a Spherical Colloidal Particle*, *Journal of colloid and interface science* **239** (July, 2001) 587–590.

[136] M. L. Jiménez, F. J. Arroyo, F. Carrique, and A. V. Delgado, *Surface conductivity of colloidal particles: Experimental assessment of its contributions*, *Journal of colloid and interface science* **316** (Dec., 2007) 836–843.

[137] J. W. Swan and E. M. Furst, *A simpler expression for Henry's function describing the electrophoretic mobility of spherical colloids*, *Journal of colloid and interface science* **388** (Dec., 2012) 92–94.

[138] R. Agra, E. Trizac, and L. Bocquet, *The interplay between screening properties and colloid anisotropy: Towards a reliable pair potential for disc-like charged particles*, *The European Physical Journal E* **15** (Nov., 2004) 345–357.

[139] D. Stigter, *Electrophoresis of highly charged colloidal cylinders in univalent salt solutions. 1. Mobility in transverse field*, *The Journal of Physical Chemistry* **82** (June, 1978) 1417–1423.

[140] H. Ohshima, *Henry's function for electrophoresis of a cylindrical colloidal particle*, *Journal of colloid and interface science* **180** (1996), no. 1 299–301.

[141] H. J. Keh and S. B. Chen, *Diffusiophoresis and electrophoresis of colloidal cylinders*, *Langmuir* **9** (Apr., 1993) 1142–1149.

[142] S. Allison, *Electrophoretic mobility and primary electroviscous effect of dilute "hard" prolate ellipsoids*, *Journal of colloid and interface science* **282** (Feb., 2005) 231–237.

[143] Y. Solomentsev and J. L. Anderson, *Electrophoresis of slender particles*, *Journal of Fluid Mechanics* **279** (1994) 197–215.

[144] L. B. Harris, *Simplified calculation of electrophoretic mobility of non-spherical particles when the electrical double layer is very extended*, *Journal of colloid and interface science* **34** (1970), no. 2 322–325.

[145] H. Ohshima, *Dynamic electrophoretic mobility of a cylindrical colloidal particle*, *Journal of colloid and interface science* **185** (1997), no. 1 131–139.

[146] H. Ohshima, *On the limiting electrophoretic mobility of a highly charged colloidal particle in an electrolyte solution*, *Journal of colloid and interface science* **263** (July, 2003) 337–340.

[147] K. Rose, B. Hoffman, D. Saintillan, E. Shaqfeh, and J. Santiago, *Hydrodynamic interactions in metal rodlike-particle suspensions due to induced charge electroosmosis*, *Physical Review E* **79** (Jan., 2009) 011402.

[148] S. Pedrosa, C. Grosse, and V. Shilov, *Numerical calculation of the electrophoretic mobility of colloidal particles in weak electrolyte solutions*, *Journal of colloid and interface science* **260** (Apr., 2003) 107–117.

[149] H. Ohshima, *Approximate expression for the electrophoretic mobility of a spherical colloidal particle in a solution of general electrolytes*, *Colloids and Surfaces A: Physicochemical and Engineering Aspects* **267** (Oct., 2005) 50–55.

[150] H. Ohshima, *Approximate expression for the electrophoretic mobility of a spherical colloidal particle covered with an ion-penetrable uncharged polymer Layer*, *Colloid and Polymer Science* **283** (Dec., 2004) 819–825.

[151] B. J. Yoon and S. Kim, *Electrophoresis of spheroidal particles*, *Journal of colloid and interface science* **128** (Mar., 1989) 275–288.

[152] H. Ohshima, *Electrophoretic mobility of a highly charged colloidal particle in a solution of general electrolytes*, *Journal of colloid and interface science* **275** (July, 2004) 665–669.

[153] E. K. Zholkovskij, J. H. Masliyah, and V. N. Shilov, *Electrokinetic Phenomena in concentrated disperse systems: general problem formulation and Spherical Cell Approach*, *Advances in colloid and interface science* **134** (2007) 279–321.

[154] H. M. Manzanilla-Granados, F. Jiménez-Ángeles, and M. Lozada-Cassou, *The Œ∂-potential for a concentrated colloidal dispersion: The colloidal primitive model vs. the cell model*, *Colloids and Surfaces A: Physicochemical and Engineering Aspects* **376** (Feb., 2011) 59–66.

[155] T. J. Johnson and E. J. Davis, *An analysis of electrophoresis of concentrated suspensions of colloidal particles*, *Journal of colloid and interface science* **215** (1999), no. 2 397–408.

[156] F. Carrique, F. J. Arroyo, and A. V. Delgado, *Electrokinetics of Concentrated Suspensions of Spherical Colloidal Particles with Surface Conductance, Arbitrary Zeta Potential, and Double-Layer Thickness in Static Electric Fields*, *Journal of colloid and interface science* **252** (Aug., 2002) 126–137.

[157] R. J. Hunter, *Measuring zeta potential in concentrated industrial slurries*, *Colloids and Surfaces A: Physicochemical and Engineering Aspects* **195** (2001), no. 1 205–214.

[158] M. Aubouy, E. Trizac, and L. r. Bocquet, *Effective charge versus bare charge: an analytical estimate for colloids in the infinite dilution limit*, *Journal of Physics A: Mathematical and General* **36** (May, 2003) 5835–5840.

[159] A. Martin-Molina, M. Quesada-Perez, F. Galisteo-Gonzalez, , and R. Hidalgo-Alvarez, *Electrophoretic Mobility and Primitive Models:Surface Charge Density Effect*, *The Journal of Physical Chemistry B* **106** (2002), no. 27 6881–6886.

[160] J. P. Camp and A. T. Capitano, *Size-dependent mobile surface charge model of cell electrophoresis*, *Biophysical Chemistry* **113** (Feb., 2005) 115–122.

[161] M.-S. Chun and I. Lee, *Rigorous estimation of effective protein charge from experimental electrophoretic mobilities for proteomics analysis using microchip electrophoresis*, *Colloids and Surfaces A: Physicochemical and Engineering Aspects* **318** (Apr., 2008) 191–198.

[162] R. W. O'Brien and L. R. White, *Electrophoretic mobility of a spherical colloidal particle*, *Journal of the Chemical Society, Faraday Transactions 2: Molecular and Chemical Physics* **74** (1978) 1607–1626.

[163] K. H. Jacobson, I. L. Gunsolus, T. R. Kuech, J. M. Troiano, E. S. Melby, S. E. Lohse, D. Hu, W. B. Chrisler, C. J. Murphy, G. Orr, F. M. Geiger, C. L. Haynes, and J. A. Pedersen, *Lipopolysaccharide Density and Structure Govern the Extent and Distance of Nanoparticle Interaction with Actual and Model Bacterial Outer Membranes*, *Environmental Science & Technology* **49** (Sept., 2015) 10642–10650.

[164] B. J. Kirby and E. F. Hasselbrink, *Zeta potential of microfluidic substrates: 1. Theory, experimental techniques, and effects on separations*, *Electrophoresis* **25** (Jan., 2004) 187–202.

[165] A. Sze, D. Erickson, L. Ren, and D. Li, *Zeta-potential measurement using the Smoluchowski equation and the slope of the current–time relationship in electroosmotic flow*, *Journal of colloid and interface science* **261** (May, 2003) 402–410.

[166] T. Driehorst, P. O'Neill, P. M. Goodwin, S. Pennathur, and D. K. Fygenson, *Distinct Conformations of DNA-Stabilized Fluorescent Silver Nanoclusters Revealed by Electrophoretic Mobility and Diffusivity Measurements*, *Langmuir* **27** (July, 2011) 8923–8933.

[167] G. J. M. Bruin, *Recent developments in electrokinetically driven analysis on microfabricated devices*, *Electrophoresis* **21** (Dec., 2000) 3931–3951.

[168] B. Franze and C. Engelhard, *Fast Separation, Characterization, and Speciation of Gold and Silver Nanoparticles and Their Ionic Counterparts with Micellar Electrokinetic Chromatography Coupled to ICP-MS*, *Analytical Chemistry* **86** (June, 2014) 5713–5720.

[169] H. Qu, T. K. Mudalige, and S. W. Linder, *Capillary electrophoresis/inductively-coupled plasma-mass spectrometry: Development and optimization of a high resolution analytical tool for the size-based characterization of nanomaterials in dietary supplements*, *Analytical Chemistry* **86** (2014), no. 23 11620–11627.

[170] A. Lapresta-Fernández and A. Salinas-Castillo, *A general perspective of the characterization and quantification of nanoparticles: imaging, spectroscopic, and separation techniques*, *Critical Reviews in ...* **39** (2014), no. 6 423–458.

[171] A. I. López-Lorente, B. M. Simonet, and M. Valcárcel, *Electrophoretic methods for the analysis of nanoparticles*, *TrAC Trends in Analytical Chemistry* **30** (2011), no. 1 58–71.

[172] U. Pyell, A. H. Jalil, D. A. Urban, C. Pfeiffer, and B. Pelaz, *Characterization of hydrophilic coated gold nanoparticles via capillary electrophoresis and Taylor dispersion analysis. Part II: Determination of the hydrodynamic . . .*, *Journal of colloid and interface science* **450** (2015), no. C 131–140.

[173] B. Gates, *Determining the Stability of Nanoparticles in Solution and Implications for Using these Materials*, 2012.

[174] L. Rodriguez-Lorenzo, B. Rothen-Rutishauser, A. Petri-Fink, and S. Balog, *Nanoparticle Polydispersity Can Strongly Affect In Vitro Dose*, *Particle & Particle Systems Characterization* **32** (2015), no. 3 321–333.

[175] J. C. Y. Kah, A. Zubieta, R. A. Saavedra, and K. Hamad-Schifferli, *Stability of gold nanorods passivated with amphiphilic ligands*, *Langmuir* **28** (June, 2012) 8834–8844.

[176] M. Sethi, G. Joung, and M. R. Knecht, *Stability and Electrostatic Assembly of Au Nanorods for Use in Biological Assays*, *Langmuir* **25** (Jan., 2009) 317–325.

[177] B. C. Rostro-Kohanloo, L. R. Bickford, C. M. Payne, E. S. Day, L. J. E. Anderson, M. Zhong, S. Lee, K. M. Mayer, T. Zal, L. Adam, C. P. N. Dinney, R. A. Drezek, J. L. West, and J. H. Hafner, *The stabilization and targeting of surfactant-synthesized gold nanorods*, *Nanotechnology* **20** (Oct., 2009) 434005.

[178] R. Becker, B. Liedberg, and P.-O. Käll, *Ctab promoted synthesis of au nanorods – temperature effects and stability considerations*, *J. Colloid Interface Sci.* **343** (Mar., 2010) 25–30.

[179] A. R. Ferhan, L. Guo, and D.-H. Kim, *Influence of Ionic Strength and Surfactant Concentration on Electrostatic Surfacial Assembly of Cetyltrimethylammonium Bromide-Capped Gold Nanorods on Fully Immersed Glass*, *Langmuir* **26** (July, 2010) 12433–12442.

[180] N. Bogliotti, B. Oberleitner, A. Di-Cicco, F. Schmidt, J.-C. Florent, and V. Semetey, *Optimizing the formation of biocompatible gold nanorods for cancer research: Functionalization, stabilization and purification*, *J. Colloid Interface Sci.* **357** (May, 2011) 75–81.

[181] J. C. Y. Kah, J. Chen, A. Zubieta, and K. Hamad-Schifferli, *Exploiting the Protein Corona around Gold Nanorods for Loading and Triggered Release*, *ACS Nano* **6** (Aug., 2012) 6730–6740.

[182] N. A. Merrill, M. Sethi, and M. R. Knecht, *Structural and equilibrium effects of the surface passivant on the stability of au nanorods*, *ACS Appl. Mater. Interfaces* **5** (Aug., 2013) 7906–7914.

[183] A. P. Leonov, J. Zheng, J. D. Clogston, S. T. Stern, A. K. Patri, and A. Wei, *Detoxification of Gold Nanorods by Treatment with Polystyrenesulfonate*, *ACS Nano* **2** (Dec., 2008) 2481–2488.

[184] A. M. Alkilany, L. B. Thompson, and C. J. Murphy, *Polyelectrolyte Coating Provides a Facile Route to Suspend Gold Nanorods in Polar Organic Solvents and Hydrophobic Polymers*, *ACS Applied Materials & Interfaces* **2** (Dec., 2010) 3417–3421.

[185] T. Wang, X. Zhang, Y. Pan, X. Miao, Z. Su, C. Wang, and X. Li, *Fabrication of doxorubicin functionalized gold nanorod probes for combined cancer imaging and drug delivery*, *Dalton Trans.* **40** (2011), no. 38 9789–9794.

[186] K. K. Comfort, J. W. Speltz, B. M. Stacy, L. R. Dosser, and S. M. Hussain, *Physiological fluid specific agglomeration patterns diminish gold nanorod photothermal characteristics*, *Adv. Nanopart.* **02** (2013), no. 04 336–343.

[187] C. J. Murphy, A. M. Gole, S. E. Hunyadi, J. W. Stone, P. N. Sisco, A. Alkilany, B. E. Kinard, and P. Hankins, *Chemical sensing and imaging with metallic nanorods*, *Chemical Communications* **5** (2008) 544–557.

[188] V. Berry, A. Gole, S. Kundu, C. J. Murphy, and R. F. Saraf, *Deposition of CTAB-Terminated Nanorods on Bacteria to Form Highly Conducting Hybrid Systems*, *Journal of the American Chemical Society* **127** (Dec., 2005) 17600–17601.

[189] A. Gole and C. J. Murphy, *Biotin streptavidin-induced aggregation of gold nanorods: Tuning rod-rod orientation*, *Langmuir* **21** (Nov., 2005) 10756–10762.

[190] C. J. Orendorff, P. L. Hankins, and C. J. Murphy, *pH-Triggered Assembly of Gold Nanorods*, *Langmuir* **21** (Mar., 2005) 2022–2026.

[191] N. Tiwari, S. Kalele, and S. K. Kulkarni, *Modulation of Optical Properties of Gold Nanorods on Addition of KOH*, *Plasmonics* **2** (Sept., 2007) 231–236.

[192] M. Das, L. Mordoukhovski, and E. Kumacheva, *Sequestering gold nanorods by polymer microgels*, *Adv. Mater.* **20** (June, 2008) 2371–2375.

[193] V. Kozlovskaya, E. Kharlampieva, B. P. Khanal, P. Manna, E. R. Zubarev, and V. V. Tsukruk, *Ultrathin layer-by-layer hydrogels with incorporated gold nanorods as ph-sensitive optical materials*, *Chem. Mater.* **20** (Dec., 2008) 7474–7485.

[194] M. Sethi, G. Joung, and M. R. Knecht, *Linear assembly of au nanorods using biomimetic ligands*, *Langmuir* **25** (Feb., 2009) 1572–1581.

[195] Q. Zhan, J. Qian, X. Li, and S. He, *A study of mesoporous silica-encapsulated gold nanorods as enhanced light scattering probes for cancer cell imaging*, *Nanotechnology* **21** (Dec., 2009) 055704.

[196] H. Ding, K. T. Yong, I. Roy, H. E. Pudavar, W. C. Law, E. J. Bergey, and P. N. Prasad, *Gold Nanorods Coated with Multilayer Polyelectrolyte as Contrast Agents for Multimodal Imaging*, *Journal of Physical Chemistry C* **111** (Aug., 2007) 12552–12557.

[197] B. Nikoobakht, Z. L. Wang, and M. A. El-Sayed, *Self-Assembly of Gold Nanorods*, *The Journal of Physical Chemistry B* **104** (Sept., 2000) 8635–8640.

[198] H.-C. Huang, S. Barua, D. B. Kay, and K. Rege, *Simultaneous Enhancement of Photothermal Stability and Gene Delivery Efficacy of Gold Nanorods Using Polyelectrolytes*, *ACS Nano* **3** (Oct., 2009) 2941–2952.

[199] Z. Guo, X. Fan, L. Xu, X. Lu, C. Gu, Z. Bian, N. Gu, J. Zhang, and D. Yang, *Shape separation of colloidal gold nanoparticles through salt-triggered selective precipitation*, *Chem. Commun.* **47** (2011), no. 14 4180–4182.

[200] L. Liu, Z. Guo, L. Xu, R. Xu, and X. Lu, *Facile purification of colloidal nir-responsive gold nanorods using ions assisted self-assembly*, *Nanoscale Res. Lett.* **6** (Feb., 2011) 143.

[201] H. Petrova, J. Perez Juste, I. Pastoriza-Santos, G. V. Hartland, L. M. Liz-Marzán, and P. Mulvaney, *On the temperature stability of gold nanorods: Comparison between thermal and ultrafast laser-induced heating*, *Phys. Chem. Chem. Phys.* **8** (2006), no. 7 814–821.

[202] J. C. Y. Kah, C. Grabinski, E. Untener, C. Garrett, J. Chen, D. Zhu, S. M. Hussain, and K. Hamad-Schifferli, *Protein coronas on gold nanorods passivated with amphiphilic ligands affect cytotoxicity and cellular response to penicillin/streptomycin*, *ACS Nano* **8** (May, 2014) 4608–4620.

[203] C. F. Bohren and D. R. Huffman, *Absorption and scattering of light by small particles*. John Wiley & Sons, 2008.

[204] J. Gregory, *Monitoring particle aggregation processes*, *Adv. Colloid Interface Sci.* **147-148** (Mar., 2009) 109–123.

[205] K. Rahn-Chique, A. M. Puertas, M. S. Romero-Cano, C. Rojas, and G. Urbina-Villalba, *Nanoemulsion stability: Experimental evaluation of the flocculation rate from turbidity measurements*, *Adv. Colloid Interface Sci.* **178** (Oct., 2012) 1–20.

[206] F. Gambinossi, S. E. Mylon, and J. K. Ferri, *Aggregation kinetics and colloidal stability of functionalized nanoparticles*, *Advances in Colloid and Interface Science* **222** (2014) 332–349.

[207] K. L. Kelly, E. Coronado, L. L. Zhao, and G. C. Schatz, *The optical properties of metal nanoparticles: The influence of size, shape, and dielectric environment*, *J. Phys. Chem. B* **107** (Jan., 2003) 668–677.

[208] S. E. Lohse and C. J. Murphy, *The quest for shape control: A history of gold nanorod synthesis*, *Chem. Mater.* **25** (Apr., 2013) 1250–1261.

[209] C. S. Weisbecker, M. V. Merritt, and G. M. Whitesides, *Molecular self-assembly of aliphatic thiols on gold colloids*, *Langmuir* **12** (1996) 3763–3772.

[210] K. S. Mayya, V. Patil, and M. Sastry, *On the stability of carboxylic acid derivatized gold colloidal particles: The role of colloidal solution ph studied by optical absorption spectroscopy*, *Langmuir* **13** (1997), no. 15 3944–3947.

[211] Y. Zhao, Z. Wang, W. Zhang, and X. Jiang, *Adsorbed tween 80 is unique in its ability to improve the stability of gold nanoparticles in solutions of biomolecules*, *Nanoscale* **2** (2010), no. 10 2114–2119.

[212] C. G. Blatchford, J. R. Campbell, and J. A. Creighton, *Plasma resonance—enhanced raman scattering by absorbates on gold colloids: the effects of aggregation*, *Surf. Sci.* **120** (1982), no. 2 435–455.

[213] Z. Wang, J. H. Lee, and Y. Lu, *Label-free colorimetric detection of lead ions with a nanomolar detection limit and tunable dynamic range by using gold nanoparticles and DNAzyme*, *Adv. Mater.* **20** (Sept., 2008) 3263–3267.

[214] N. R. Jana, L. Gearheart, and C. J. Murphy, *Seed-mediated growth approach for shape-controlled synthesis of spheroidal and rod-like gold nanoparticles using a surfactant template*, *Adv. Mater.* **13** (2001) 1389–1393.

[215] B. Nikoobakht and M. A. El-Sayed, *Preparation and growth mechanism of gold nanorods (nrs) using seed-mediated growth method*, *Chem. Mater.* **15** (May, 2003) 1957–1962.

[216] P. J. Wyatt, *Measurement of Special Nanoparticle Structures by Light Scattering*, *Analytical Chemistry* **86** (Aug., 2014) 7171–7183.

[217] S. Finfer, R. Bellomo, N. Boyce, J. French, J. Myburgh, R. Norton, R. Norton, M. Doig, M. Hayek, S. O'Donnell, A. Bell, D. Blythe, J. Cade, M. Chapman, L. Cole, J. Cooper, A. Davies, C. French, C. Joyce, C. McArthur, S. MacMahon, B. Neal, J. Presneill, P. Saul, I. Seppelt, D. Stephens, A. Turner, A. Williams, C. Woolfe, R. Peto, P. Sandercock, C. Sprung, D. Young, S. K. Lo,

S. Sivarajasingham, L. Francis, M. Woodward, J. Charlton, C. Harry, L. Higgins, K. Moulden, S. Vallance, J. Chadderton, L. Newby, S. Bates, D. Goldsmith, A. Voss, A. Palermo, K. Jayne, M. Merai, B. Norton, S. Pandey, M. Schmidt, R. Carroll, B. McFadyen, J. Clarke, J. Powell, J. Tai, I. Hynesova, L. Weisbrodt, L. Bradley, T. Kelly, A. Limpus, R. Moore, S. Creed, S. Kaplan, J. Rivett, J. Thomas, K. Marsden, C. Boyce, B. Howe, M. Robertson, G. Doig, A. O'Connor, J. Potter, N. Ramakrishnan, C. Powell, D. Rajbhandari, K. Girling, M. Hodgetts, A. Jovanovska, L. Little, and S. S. Investigators, *A comparison of albumin and saline for fluid resuscitation in the intensive care unit*, *New England Journal of Medicine* **350** (2004), no. 22 2247–2256.

[218] C. L. John, S. L. Strating, K. A. Shephard, and J. X. Zhao, *Reproducibly synthesize gold nanorods and maintain their stability*, *RSC Advances* **3** (2013), no. 27 10909–10918.

[219] Y. Wang and L. Tang, *Multiplexed gold nanorod array biochip for multi-sample analysis*, *Biosensors and Bioelectronic* **67** (Aug., 2014) 1–7.

[220] T. Kim, C.-H. Lee, S.-W. Joo, and K. Lee, *Kinetics of gold nanoparticle aggregation: Experiments and modeling*, *J. Colloid Interface Sci.* **318** (2008), no. 2 238–243.

[221] A. S. D. S. Indrasekara, R. C. Wadams, and L. Fabris, *Ligand exchange on gold nanorods: Going back to the future*, *Part. Part. Syst. Charact.* **31** (Aug., 2014) 819–838.

[222] M. I. Neuman and M. B. Harper, *Time to positivity of blood cultures for children with Streptococcus pneumoniae bacteremia*, *Clinical infectious diseases* **33** (2001), no. 8 1324–1328.

[223] N. Wellinghausen, A. J. Kochem, C. Disque, H. Muhl, S. Gebert, J. Winter, J. Matten, and S. G. Sakka, *Diagnosis of Bacteremia in Whole-Blood Samples by Use of a Commercial Universal 16S rRNA Gene-Based PCR and Sequence Analysis*, *Journal of Clinical Microbiology* **47** (Aug., 2009) 2759–2765.

[224] M. Hassan-King, I. Baldeh, O. Secka, A. Falade, and B. Greenwood, *Detection of Streptococcus pneumoniae DNA in blood cultures by PCR.*, *Journal of Clinical Microbiology* **32** (1994), no. 7 1721–1724.

[225] P. K. Grewal, P. V. Aziz, S. Uchiyama, G. R. Rubio, R. D. Lardone, D. Le, N. M. Varki, V. Nizet, and J. D. Marth, *Inducing host protection in pneumococcal sepsis by preactivation of the ashwell-morell receptor*, *Proceedings of the National Academy of Sciences* **110** (2013), no. 50 20218–20223.

[226] A. M. Alkilany, A. Shatanawi, T. Kurtz, R. B. Caldwell, and R. W. Caldwell, *Toxicity and Cellular Uptake of Gold Nanorods in Vascular Endothelium and Smooth Muscles of Isolated Rat Blood Vessel: Importance of Surface Modification*, *Small* **8** (Feb., 2012) 1270–1278.